RICE UNIVERSITY

Transport Properties of Topological Phases in Broken Gap InAs/GaSb Based Quantum Wells

by

Ivan Knez

A Thesis Submitted
in Partial Fulfillment of the
Requirements for the Degree

Doctor of Philosophy

Approved, Thesis Committee:

Rui-Rui Du, Chair
Professor of Physics and Astronomy

Adilet Imambekov
Assistant Professor of Physics and Astronomy

Junichiro Kono
Professor of Electrical and Computer Engineering

Houston, Texas

March, 2012

Abstract

Transport Properties of Topological Phases in Broken Gap InAs/GaSb Based Quantum Wells

by

Ivan Knez

The quantum Spin Hall Insulator (QSHI) is a two-dimensional variant of a novel class of materials characterized by topological order, whose unique properties have recently triggered much interest and excitement in the condensed matter community. Most notably, the topological properties of these systems hold great promise in mitigating the difficult problem of decoherence in implementations of quantum computers. Although QSHI has been theoretically predicted in a few different materials, prior to the work presented in this thesis, only the HgTe/CdTe semiconductor system has shown direct evidence for the existence of this phase. Ideally insulating in the bulk, QSHI is characterized by one-dimensional channels at the sample perimeter, which have a helical property, with carrier spin tied to the carrier direction of motion, and protected from elastic back-scattering by time-reversal symmetry. In this thesis we present low temperature transport measurements, showing strong evidence for the existence of proposed helical edge channels in InAs/GaSb quantum wells, which thus emerge as an important alternate to HgTe/CdTe quantum wells in stud-

ies of two-dimensional topological insulators and superconductors. Surprisingly, edge modes persist in spite of comparable bulk conduction of non-trivial origin and show only weak dependence on magnetic field in mesoscopic devices. We elucidate that the seeming independence of edge on bulk transport comes due to the disparity in Fermi wave-vectors between the bulk and the edge, leading to a total internal reflection of the edge modes. Furthermore, low Schottky barrier of this material system and good interface to superconductors allows us to probe topological properties of helical channels in Andreev reflection measurements, opening a promising route towards the realization of topologically superconducting phases hosting exotic Majorana modes.

Acknowledgments

I would like to thank my advisor Prof. Rui-Rui Du for giving me a great opportunity to work and grow in the rapidly developing field of topological phases. I am indebted to his genorosity, fantastic support and guidance during my graduate work. I am also very grateful to my committee members, Prof. Junichiro Kono and Prof. Adilet Imambekov, for taking the time out of their busy schedules to read this thesis and serve on the thesis committee. I also thank Prof. Huey W. Huang, Prof. Douglas Natelson, and Prof. Emilia Morosan for serving on my advisory and master thesis committees.

I am immensely indebted to many of my colleagues without whom this work would not be possible, especially to my former labmates Dr. Kristjan Stone, Dr. Zhouquan Yuan, Dr. Chi Zhang, and Dr. Yanhua Dai who welcomed me and my wife here in Houston, as well as our post-doc Dr. Guangtong Liu, who joined us shortly afterwards. Special thanks go to Patrick Johnson, Dr. Tim Gilheart and Dr. Kelley Bradley for doing such a great job with keeping the clean rooms running, both at Rice University and University of Houston, respectively. I am also indebted to Dr. Dan Ward and Dr. Gavin Scott from Prof. Natelson's group who got me started with e-beam lithography, as well as to Eric Frey, Dirk Lorenz, Emilian Nica and Dr. Jorge Zuloaga Franco for the careful proofreading of this thesis.

I gratefully acknowledge our collaborators at Teledyne Scientific and Imaging, Dr. Gerry Sullivan and Amal Ikhlassi for MBE growth of our wafers, and Dr. Josh

Bergman for processing suggestions. I would also like to thank Dr. Jun Li and Prof. Kai Chang from the Institute of Semiconductors, Chinese Academy of Sciences for their theoretical calculations. The work at Rice was supported by Rice Faculty Initiative Fund, Hackerman Advanced Research Program grant 003604-0062-2009, Welch Foundation grant C-1682, and NSF grant DMR-0706634. I acknowledge partial support from M. W. Keck Scholar. A portion of this work was performed at the National High Magnetic Field Laboratory (NHMFL), which is supported by NSF Cooperative Agreement No. DMR-0084173, by the State of Florida, and by the DOE. Travel to NHMFL was supported by NSF Grant No. DMR-0706634. We thank Dr. Tim Murphy and Dr. Ju-Hyun Park for expert technical assistance. We also thank Prof. Shoucheng Zhang for bringing our attention to InAs/GaSb system, as well as to Prof. Herbert Kroemer, Prof. Xiao-Liang Qi, Prof. Chao-Xing Liu, Dr. Joseph Maciejko, and Dr. Markus Konig for helpful discussions.

Finally, I thank and dedicate this thesis to my wife Liza who had much faith and trust in me over the last several years, following me across the world in my whimsical choice to pursue a career in science. It really takes a special woman to leave behind her job, and the comfort of dear friends and family only to embark upon a journey to the unknown, without clear direction or any promise of reward.

Contents

Illustrations

Chapter 1

Introduction

1.1 Topological Order

An overarching goal of condensed matter physics is the classification and understanding of various phases of matter and its phase transitions. A substantial proportion of all phase transitions can be understood in terms of the celebrated Landau-Ginzburg framework of spontaneous symmetry breaking and the notion of a local order parameter which describes the onset of the particular order in the system. For example, in ferromagnetic systems rotational symmetry is spontaneously broken at the Curie temperature, while the concurrent onset of magnetic order is characterized by the local order parameter of net magnetization. Nevertheless, the concept of symmetry breaking and local order parameter describing the phase transition, although a general concept, does not suffice to explain some intriguing phenomena such as the integer quantum Hall effect [1] and many body phases of the fractional quantum Hall effect [2]. In fact, it is the study of these effects which has led to a new paradigm in the classification of condensed matter systems, that is the notion of topological order [3], which lacks a local order parameter and is instead characterized by some non-local property. Specifically, in the integer quantum Hall effect (IQHE), Hall resistance plateaus have shown a baffling degree of precision in quantization, some one part

in billion, universally appearing across many different systems. Indeed, it has been shown theoretically [3], that the fundamental reason for such remarkable quantization is the existence of topological invariants, in this case Hall conductance, which do not change for smooth variations of material parameters and hence can be considered as non-local order parameters of the system.

More recently, a topologically distinct class of electronic insulators has been predicted to occur in some 2D and 3D systems [4, 5] which preserve time reversal symmetry and have strong spin orbit coupling. This novel type of materials is insulating in the bulk but posseses Dirac type surface (3D case) or edge states (2D case), which are guaranteed by the symmetry of the bulk bands alone and are independent of the microscopic details at the sample edge. Just like normal insulators (NI), topological insulators (TI) have an energy gap in the bulk between the lowest empty band, which we normally refer to as the conduction band, and the highest filled band, which we call the valence band. Because all of the bands are either empty or filled, the bulk conductance of both materials (NI and TI) vanishes in the zero-temperature limit. Nevertheless, it has been recognized in the early 1980s by Volkov and Pankratov [6, 7] that the opposing symmetry of the valence and conduction states at the interface between two distinct insulators necessitates the existence of linearly dispersing gapless interface states, leading to systems which are uniquely conductive along surfaces or edges but insulating elsewhere. These ideas have been independently rediscovered and further developed in the mid-2000s, leading to an emerging field of topological

phases [4, 5], whose experimental studies are the subject of this thesis. Here we focus primarily on the transport studies of the 2D TI phase, which is also known as the quantum spin Hall insulating (QSHI) phase, realized in the broken gap InAs/GaSb semiconducting material.

1.2 Motivation for InAs/GaSb Material System

In 2D TIs time reversal symmetry leads to the helical property of the linearly dispersing Dirac edge modes, where the electron momentum and spin degrees of freedom are locked-in, leading to the vanishing of the elastic backscattering probability of edge electrons. As a result, within certain limits, edge modes in 2D TI are by its nature dissipationless, making topological insulators not only fundamentally interesting but also practically relevant. In fact, the ability to tune from the NI to the TI phase in a single device would not only enable the first dissipationless transistor - a holy grail of the modern semiconductor industry - but also allow the study of topological quantum phase transitions [8]. Furthermore, in the latest theoretical developments, it has been predicted that the combination of the TI edge and an ordinary superconductor can lead to a superconducting topological phase and realizations of Majorana bound states [9, 10]. Majorana fermions (MFs) [11], which can be thought of as half-fermions, are their own anti-particles, and possess non-Abelian exchange properties [12, 13], i.e. exchange of two MFs does not modify the wave function by a simple phase factor but generates a completely different wave function. As a result, manipulation of MFs is

instrumental for the realization of braiding operations in topological quantum computers [14]. Both of the mentioned thrusts open exciting opportunities in the study of topological phases, and as we will discuss for the remainder of this thesis, they are uniquely suited for the InAs/GaSb material system, which shows evidence for the existence of the TI phase and also exhibits a strong superconducting proximity effect [15] - a necessary requirement for the realization of TI/superconductor hybrid structures.

Most of the progress in topological phases that has so far been achieved is mainly theoretical, and despite intense experimental efforts many of the interesting proposals are yet to come to fruition, such as axion dynamics and Majorana fermion bound states [4, 5]. In 2D, the TI phase has been first predicted to occur in graphene [16] and strained GaAs [17]; shortly thereafter in inverted HgTe QWs [18], and InAs/GaSb composite quantum wells (CQWs) [8], which proved to be much closer to the current experimental reach. The QSH phase has a natural extension in 3D topological insulators [19] where the surface exhibits a graphene-like electronic structure with a single Dirac cone that bridges the bulk gap. These unique states have been observed in angle resolved photoemission spectroscopy (ARPES) in $Bi_{1-x}Sb_x$ [20] and Bi_2Se_3 [21]; in addition, some evidence for the non-trivial surface states has been shown in scanning tunneling microscopy [22, 23, 24, 25, 26] and transport measurements [27, 28, 29, 30, 31].

Unfortunately, 3D topological insulators are notoriously conductive [4, 5] and

from the transport perspective prior to the work presented in this thesis, inverted HgTe/CdTe quantum wells were the only material showing truly insulating bulk and helical edge mode transport – a defining characteristic of 2D TIs [32, 33]. Nevertheless, the mercury content in HgTe QWs imposes some strict fabrication restrictions and in this material, the TI phase can be tuned only through the thickness of the well, which is a discrete parameter. On the other hand, InAs/GaSb is another mature material, commonly used in infrared detectors and in high electron mobility transistors (HEMTs) [34] with well developed molecular beam epitaxy (MBE) growth and device fabrication techniques. Compared to HgTe/CdTe, InAs/GaSb carries a series of advantages, including low Schottky barriers to most metals, with good interface to superconductors [15] and continuously tunable band structure via electrical fields [35], making this material uniquely suited for the study of the phase transition from TI to NI via a continuously varying parameter as well as for the realization of TI/superconductor hybrid structures [4, 5].

1.3 2D Topologically Insulating Phase in InAs/GaSb

InAs, GaSb, and AlSb belong to a class of lattice matched compounds, commonly referred to as the 6.1 Å family [34], which is the approximate lattice constant of all three materials. In this system, AlSb serves as a good quantum well barrier to narrow gap InAs with a very high band offset of 1.35 eV, enabling deep quantum wells. In addition, the small electron effective mass in InAs results in the second

highest room temperature mobility of all semiconductors (the first is InSb), making this material very interesting, especially from a device perspective. Nevertheless, the most attractive aspect of the 6.1 Å family is its unusual "broken gap" band alignment between InAs and GaSb, with the conduction band of InAs some 150 meV lower than the valence band of GaSb [34]. In wider quantum wells, this allows for the coexistence of closely separated electron (in InAs) and hole (in GaSb) two-dimensional gases, that are confined by neighboring AlSb barriers.

Furthermore, when the in-plane momentum and energy of electrons and holes are equal, carriers can tunnel between the wells and the system is strongly coupled. In this case, due to the hybridization of the bands, a mini-gap opens in the otherwise semimetallic band structure, resulting in a non-monotonic band dispersion. Note that in this case the progression of the states is inverted, with conduction states being lower in energy than the valence states. A smooth connection of bands inside and outside of the sample (vacuum or insulator) leads to gapless edge modes with a linear dispersion at the sample boundary. Time reversal symmetry considerations require these states to be helical, i.e. counterpropagating spin up and spin down states, which are protected from elastic backscattering by time reversal symmetry. Thus, in the context of TIs, the hybridization gap of inverted InAs/GaSb CQW is the bulk energy gap, while the edge states arise due to the broken gap band alignment and not from the spin-orbit coupling as in HgTe/CdTe, graphene and strained GaAs. Nevertheless, we note here that the spin-orbital coupling due to inversion asymmetry is still an

essential ingredient for the opening of the hybridization gap, as it mixes light and heavy hole bands and hence leads to non-vanishing matrix elements between electron and what is considered predominantly heavy hole states which otherwise would be zero based on the conservation of angular momentum. This is also a hint of how hybridization gap can be increased beyond current values of 30 K to 40 K in order to possibly support room temperature operation.

Existence of the hybridization gap has been confirmed experimentally in transport [36, 37] and far-infrared measurements [38, 39]; however, a true bulk insulator, which shows temperature activated conductivity has never been observed. In fact, theoretical studies have shown that finite, even in principle vanishing amount of disorder will lead to a residual conductivity in the mini-gap regime. Interestingly, this conductivity is independent of the amount of scattering and strongly dependent on the band parameters as suggested theoretically [40] and shown experimentally in this thesis [41]. The presence of residual bulk conductivity has important implications for the TI phase and stability of the proposed helical edge states. The existence of states inside the bulk gap would presumably allow for scattering of the edge states from the opposite side of the sample, thus destroying the helical edge modes [42, 43, 44]. However, at the moment of writing the thesis, this issue is not settled even theoretically. A counterargument is that, 3D systems which are also conductive in the bulk, still show surface states characteristic of TIs, such as in ARPES measurements. In fact, our work presented in this thesis shows remarkable resilience and decoupling of edge

states to bulk conduction, which is believed to be a result of large disparity in Fermi wave-vectors between the bulk and edge states, leading to a total internal reflection of the edge modes and consequent edge-bulk decoupling.

1.4 This Thesis

Work presented in this thesis [41, 45, 46, 47] is the first experimental study of the InAs/GaSb CQW hybridization gap in the light of the recent theoretical proposal [8, 9] for this system regarding topological phases. We present detailed low temperature transport measurements of inverted InAs/GaSb CQWs in the mini-gap regime, confirming the existence of the hybridization gap. The mini-gap shows substantial residual conductivity, which is consistent with the theoretical work of Naveh and Laikhtman [40] and in agreement with the previous experimental studies [36, 37], and masks a possible contribution from the edge. Nevertheless, we find that the residual conductivity decreases as the overlap between valence and conduction subbands is reduced and as the system approaches the critical point where the band structure changes from inverted to normal, thus promoting QSHE. Furthermore, the length and width dependence of conductance in such a regime of reduced band inversion shows strong evidence for the existence of helical edge modes proposed by Liu et al [8]. Surprisingly, edge modes persist in spite of comparable bulk conduction and show only weak dependence on magnetic field for mesoscopic structures. We elucidate that the seeming independence of edge to bulk transport comes due to the disparity in

Fermi wavevectors between the bulk and the edge, leading to a total internal reflection of the edge modes. Finally, the low Schottky barrier of this material system and good interface to superconductors allows us to probe topological properties of helical channels in Andreev reflection measurements, opening a promising route towards the realization of exotic Majorana modes.

Chapter 2

Background

2.1 Band Lineups and Band Structure of InAs/GaSb QWs

InAs, GaSb, and AlSb form a well lattice matched material system dubbed the 6.1Å family for the approximate value of their lattice constants [34]. Energy gaps in the 6.1 Å family vary from 0.36 eV in InAs and 0.78 eV in GaSb to 1.69 eV in AlSb, offering a wide range of available gaps and great electron confinement with well depths of up to 1.35 eV. This allows for electron densities in InAs quantum wells of up to $10^{13}\,\mathrm{cm}^{-2}$ achieved via modulation doping. Furthermore, the effective mass of InAs is around 0.03 in units of free electron mass and is the second smallest only to InSb, with Fermi velocities exceeding $10^{8}\,\mathrm{cm/s}$, thus exhibiting near-metal properties and providing an excellent interface to superconductors. As previously mentioned, this is of great importance for experimental realizations of topological superconducting phases, which might have profound technological impact leading to topological quantum computing.

The primary interest in the 6.1 Å family comes from the unusual band lineup shown in Fig. 2.1. It has been observed very early that InAs/GaSb heterostructures possess a broken gap band alignment [48] and this discovery propelled much of the research interest in antimonides in the 80's and early 90's. The bulk valence band top of GaSb is some 150 meV higher than the bottom of the conduction band in InAs

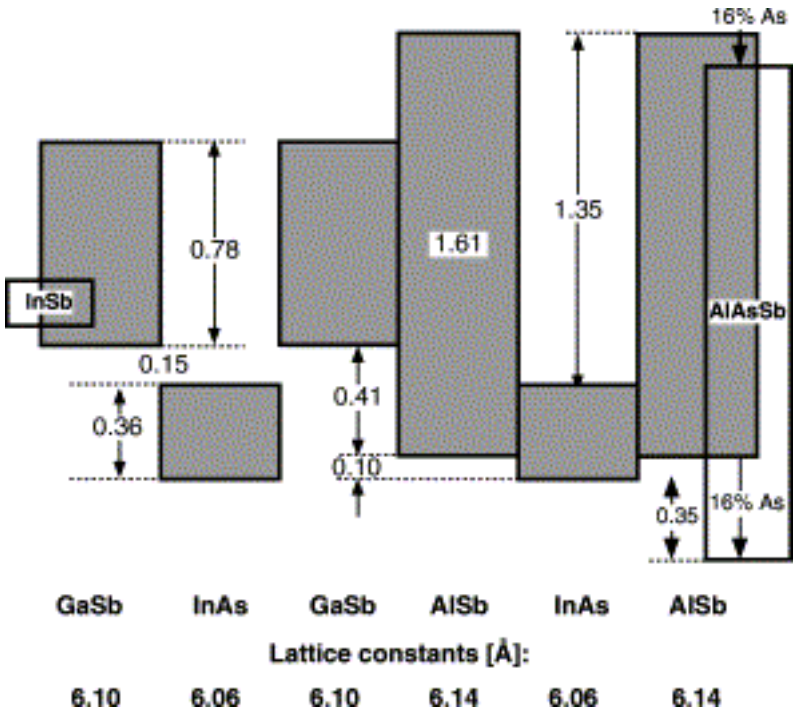

Figure 2.1 : Band lineup in the 6.1 Å family and lattice constants of each material. Shaded regions are the bandgaps and all energies are in eV [34].

[34], resulting in charge transfer between GaSb and InAs layers and a built-in electric field at the interface, which enables an excellent tunability of the band structure with external electric fields [35]. In AlSb, the valence band is some 0.4 eV lower than the valence band in GaSb, while the conduction band of AlSb is approximately 0.4 eV higher. Thus, AlSb can serve as a quantum well barrier, confining both electrons and holes in the InAs and GaSb layers, respectively.

This is utilized in composite quantum well structures (CQWs) shown in Fig. 2.2 a. Note that because holes have a negative effective mass, in band diagrams hole quantum wells are in the opposite direction to that of electrons, analogous to the electron and positron case in Dirac's relativistic quantum theory. Thus, CQWs are

effectively a composite of seperate electron (InAs) and hole (GaSb) wells, placed in immediate proximity. Furthermore, due to the broken gap band alignment, the inverted CQW structure should intrinsically have equal densities of both 2D electron and hole gases. However, the high density of surface states usually pins the Fermi level some 130 meV high above the bottom of the bulk conduction band in InAs [49], and depending on the CQW width parameters, gating is necessary to induce holes in the GaSb layer. We will discuss this issue seperately in the experimental section of this thesis.

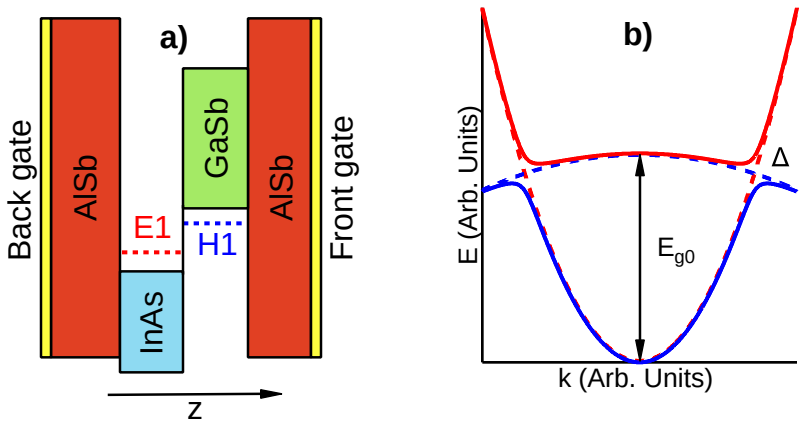

Figure 2.2 : Panel a) shows the structure and energy spectrum of inverted CQW with $E1 < H1$. Panel b) shows the energy dispersion of uncoupled $E1$ and $H1$ bands (dashed) and coupled (full line). At the anti-crossing point, where $n \sim p$, a hybridization gap Δ opens. Separation of the bands, E_{go}, as well as Fermi energy E_F can be tuned with front and back gates shown in a.

The width of the CQW well determines two fundamentally different regimes of this system: normal, with the usual progression of bands from valence to conduction for increasing energy; and an inverted regime, with the opposite arrangement. In quantum wells, energy levels are discrete and hence conduction and valence states

will form subbands. For the CQWs studied in this thesis only the first electron and heavy-hole subbands, $E1$ and $H1$, are experimentally relevant and hence we restrict our discussion only to those. In the infinite quantum well approximation, the position of the edges of these subbands in energy from the bottom of the electron and hole well goes as $\sim \frac{h^2}{8m_{e,h}a_{e,h}^2}$, where $a_{e,h}$ is the electron and hole quantum well width and m_e and m_h are electron and hole effective masses. Thus, for a narrow CQW, i.e. smaller $a_{e,h}$, $E1$ will be higher than $H1$, resulting in normal structure. On the other hand, for wider wells, $E1$ will be below $H1$, as shown in Fig. 2.2 a, and such structure is referred to as inverted.

The inverted regime is of particular interest because in this case electrons and holes coexist in their respective quantum wells. Due to their proximity, the electron wavefunction extends into the hole layer, inducing quantum mechanical coupling between 2D electron and hole systems. When the in-plane momentum and carrier energy in the two wells are nearly equal, the system will be strongly coupled, and electron and hole states will be mixed [50, 35]. In analogy to the familiar case of bonding and antibonding states, a small hybridization gap Δ on the order of $2-5\,\mathrm{meV}$ opens. Thus, the semimetallic band dispersion, shown in dashed in Fig. 2.2 b, becomes non-monotonic, shown with full line, with a distinct mini-gap [50, 35, 36, 37, 39]. In other words, $E1$ and $H1$ bands anticross at a finite momentum value, and with a suitable coupling potential between the bands, this degeneracy is lifted, opening a mini-gap in the spectrum. Because this hybridization gap is the essence of our study presented

in this thesis, we discuss its theoretical origin and experimental implications in detail in the following sections. Note that for the moment we ignore the phenomena which manifest at the sample edge, and focus exclusively on the bulk band structure. Based on symmery arguments, we will later argue for the existence of helical edge states in structures with a hybridized band spectrum.

2.2 Hybridization of Electron-Hole Subbands and Mini-gap Conductivity

Electron-hole hybridization is a textbook band anticrossing problem and in the simplest model it can be described within a two-band Hamiltonian using uncoupled electron, $|\psi_e\rangle$, and hole states, $|\psi_h\rangle$ as a basis:

$$H = \begin{bmatrix} E_e & V(k) \\ V(k)^\star & E_h \end{bmatrix}, \tag{2.1}$$

where $E_e = \frac{\hbar^2 k^2}{2m_e}$ and $E_h = E_{g0} - \frac{\hbar^2 k^2}{2m_h}$ are uncoupled electron and hole energies and E_{g0} is the overlap between the $H1$ and $E1$ subbands. Notice that for the inverted regime $E_{g0} > 0$, and the two bands will anticross when $E_e = E_h$, so that the anticrossing point in in-plane momentum is $k_{cross} = \sqrt{E_{g0}\frac{m^*}{2\hbar^2}}$, where $m^* = \frac{m_e m_h}{m_e + m_h}$ is the reduced mass. In this simple model we neglect effects of the self-consistent potential, which will only shift band edges of the quantum well, and thus to lowest order affects only the value of E_{g0} [51]. Coupling between the wells is described with the off-diagonal

element $V(k)$ which generally depends on the wavevector k. Tunneling is allowed only for the states of the same symmetry, i.e. same angular momentum, and thus electron states ($J = 1/2$, $m_J = \pm 1/2$) can couple to heavy-hole states ($J = 3/2$, $m_J = \pm 3/2$) only through the mixed-in light-hole component ($J = 3/2$, $m_J = \pm 1/2$), which goes to zero as k goes to zero [52, 53]. In addition, electron states are derived from s-orbitals, while the hole states come from spin-orbit coupled p-orbitals with $p_x + ip_y$ rotational symmetry around the growth axis of the wells. Because these states have opposite parity, parity selection rules require that these states be coupled through an operator which is odd under space inversion. Hence, to the second order, the off-diagonal coupling element will be linear in k. Furthermore, to preserve symmetry, within this $k \cdot p$ approach, the coupling element will go as $V(k) = w(k_x + ik_y)$ [50, 52] where w is a constant. In other words, due to the conservation of angular momentum, coupling between electron and hole states happens only due to the light-hole component of the heavy-hole band, which is mixed-in due to an inversion asymmetry type term in the Hamiltonian that is linear in momentum. Finally, following the approach of Quinn [51] we can further simplify this model by setting $V(k) = \Delta/2$ to give a constant splitting Δ. Thus, the two-band Hamiltonian describing the system is:

$$H = \begin{bmatrix} \frac{\hbar^2 k^2}{2m_e} & \Delta/2 \\ \Delta/2 & E_{g0} - \frac{\hbar^2 k^2}{2m_h} \end{bmatrix}, \tag{2.2}$$

Diagonalizing this Hamiltonian, we obtain eigenenergies as [54]:

$$E_{1,2} = \frac{E_e + E_h}{2} \pm \sqrt{\left(\frac{E_e - E_h}{2}\right)^2 + \left(\frac{\Delta}{2}\right)^2}, \tag{2.3}$$

and eigenstates as:

$$|\psi_{1,2}\rangle = cos\theta\,|\psi_{e,h}\rangle + i \cdot sin\theta\,|\psi_{h,e}\rangle\,, \tag{2.4}$$

where $sin2\theta = \frac{\Delta}{\sqrt{(E_e - E_h)^2 + \Delta^2}}$.

When the difference in particle energies is much larger than the size of the particle coupling, then the eigenstates of the system correspond to the eigenstates of two uncoupled quantum wells. The conductivity of such an uncoupled system can be described with the Drude formula: $\sigma_{xx} = ne\mu_e + pe\mu_h$. On the other hand, when the carriers in the two wells are isoenergetic, and ignoring the presence of disorder for a moment, then the band structure will be gapped due to hybridization, and in this case, expected bulk mini-gap conductivity will vanish in the low temperature limit. This comes solely due to the nonlocal nature of electrons in the growth direction of quantum wells and is not a manifestation of simple charge transfer but of real quantum mechanical coupling.

According to Einstein's relation, conductivity varies proportionally to the density of states of the system, DOS, which can be obtained from the energy dispersion given in Eq. (2.3) as $DOS = \frac{k}{\pi} \cdot \left(\frac{\partial E}{\partial k}\right)^{-1}$ and is shown in Fig. 2.3. Clearly, within the hybridization gap DOS vanishes, and thus, the expected conductivity of the system in the low-temperature limit would be identically zero. Furthermore, due to the

non-monotonic dispersion of the system, shown in Fig. 2.2, hybridized energy bands have local extrema at nonzero wavevector values, which according to the expression for DOS leads to van Hove singularities at mini-gap edges. We note here in passing, that such a large DOS may be conducive to the emergence of many-body phenomena, which have been theoretically considered for this system but to date have remained experimentally unexplored [55]. Also, we caution the reader here that in Fig. 2.3 the DOS is based on a simple two-band calculation and does not include the effect of disorder, which even in the vanishing limit has a profound effect on mini-gap conductivity as will be argued in the subsequent parts of the thesis. In fact, it is evident from our experiments that disorder leads to reconstruction of DOS singularities, putting a finite number of states inside the hybridization gap; however, at the moment, realistic density of states calculations, which include effect of disorder, are absent in the literature.

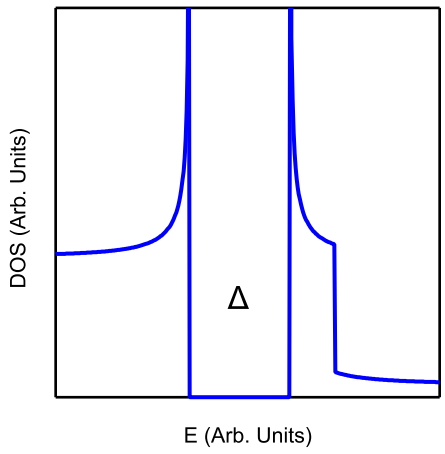

Figure 2.3 : Density of states in strongly coupled electron-hole system versus energy. Within the hybridization gap Δ density of states is zero for an ideal case of no disorder, while the mini-gap edges are marked by sharp van Hove singularities.

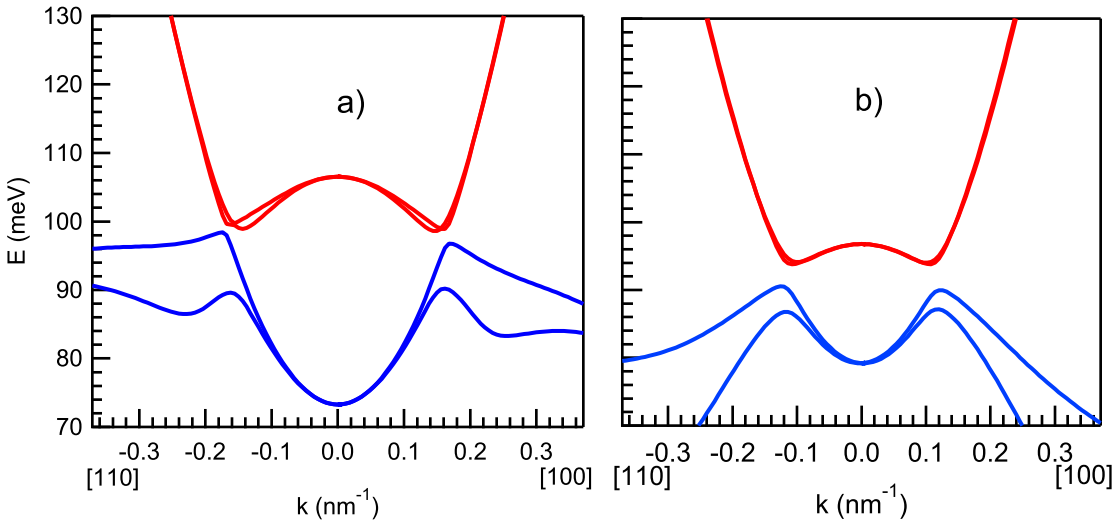

Figure 2.4 : Dispersion of $E1$ and $H1$ bands, for spin up and down projections, calculated self-consistently in 8-band $k \cdot p$ model shown for [110] and [100] crystal directions for 150 Å InAs/80 Å GaSb CQW in a), and 125 Å InAs/50 Å GaSb CQW in b). Only experimentally relevant bands are presented and energy is with respect to the conduction band of bulk InAs, i.e. bottom of InAs well [56].

The actual band structure of CQWs is slightly more complicated than the two band model might suggest. More advanced calculations, such as an 8-band $k \cdot p$ model, whose detail is beyond the scope of this thesis, elucidate some of the deficiencies of the two-band model, such as the non-parabolicity and anisotropy of bands at higher k values as well as the importance of spin degrees of freedom. Fig. 2.4 shows band structure calculated [56] using an 8-band $k \cdot p$ model for 150 Å InAs/80 Å GaSb CQW in a) and 125 Å InAs/50 Å GaSb CQW in b) - structures that were experimentally studied in this thesis. Note that these structures are inverted, and as previously claimed, only the first subbands are important; however, the gap opens at different momentum values for different crystal directions, which is a consequence of band

anisotropy, resulting in a smaller hybridization gap. Also, the mini-gap is different for the spin-up and spin-down projections; however, the qualitative physical picture discussed above is unchanged. We also note that the overlap between the electron and hole subbands E_{g0} is signficantly reduced in the narrower structures as earlier discussed, and as we will see in the latter parts of the thesis, this can have significant impact on the transport properties of the hybridization gap in realistic samples.

2.3 Double-gated CQWs

Besides the broken gap band alignment, another interesting aspect of InAs/GaSb CQWs is the tunability of the band structure via electric fields applied perpendicular to the wells [35, 57], as in the double gated structures shown in Fig. 2.2 a. Applying an electric field $\overrightarrow{F}$ across the CQW will lead to band bending such that $\overrightarrow{F} = \frac{1}{e}\nabla E$, where E is the band energy. This changes the energy profile of the wells and results in a shift of the electron and hole subband energy levels in the quantum well in the opposite direction. For example, if we apply an electric field F in the $+z$ direction, shown in Fig. 2.2a, then the $E1$ band will shift downwards, while $H1$ will move upwards and the overlap between the subbands E_{g0} will increase, and anticrossing will occur at higher k values. Similarly, applying F in the $-z$ direction will move the subbands in the opposite direction, decreasing the overlap between the subbands.

A more quantitative description can be obtained via a simple perturbative treatment. For smaller electric fields, we can treat the electric field as a perturbation,

and to first order, the energy correction will be $\langle\psi|\, V(z)\, |\psi\rangle$, where $V(z) = eFz$ for electrons and $V(z) = -eFz$ for holes, indicating that the electron and hole subbands will shift in opposite directions by $\Delta E = \pm eF\,\langle z_{e,h}\rangle$, respectively. Hence, in principle, the $E1$ and $H1$ bands can be tuned to an arbitrary position with an appropriate perpendicular electric field, which allows switching between the normal and inverted regimes via a pair of gates, as shown in Fig. 2.2.

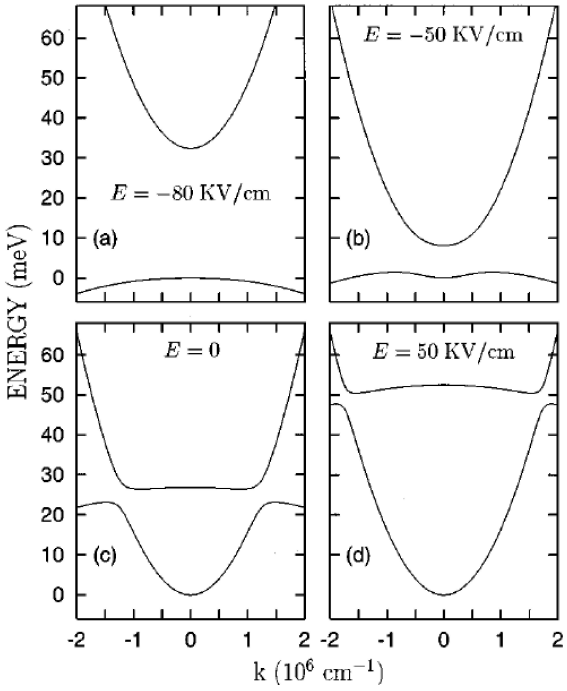

Figure 2.5 : Dispersion of $E1$ and $H1$ bands, for different perpendicular electric fields, in 170 Å InAs/50 Å GaSb CQW. Switching from normal to inverted regime can be in principle achieved via experimentally accessible electric fields [35].

Furthermore, numerical solutions of Poisson and Schrödinger equations in a self-consistent manner with realistic band parameters [35] show that biases to achieve such switching are experimentally accessible for suitable parameters of the CQW.

Fig. 2.5 shows the results of such calculations for 170 Å InAs/50 Å GaSb CQW. Note that switching can be achieved with modest electric fields of $\sim 100\,\mathrm{kV/cm}$, or in more useful units, $\sim 1V/k\text{Å}$. Typical dielectric thicknesses in our samples are on the order of kÅ and thus the required biases to achieve the switching are theoretically expected to be on the order of one Volt. Small biases are especially important because higher operating biases necessarily lead to charge trapping at the interface between the semiconductor and the dielectric and hence unavoidable hysterisis. In addition, such surface charging effects limit the absolute value of biases which can be applied. We will discuss this issue in more detail in the experimental section of the thesis.

Besides changing the band structure, gates allow us to tune the Fermi level, i.e. change the carrier density in the wells. This can be understood as a simple capacitor charging effect, that is, the carrier density will change as $\Delta n = \frac{\varepsilon}{ed}\Delta V$, where ε is the dielectric constant and d is the thickness of the dielectric layer, while ΔV is the applied bias. As previously mentioned, because the Fermi level is usually pinned high above the $H1$ band, gating allows us to push the Fermi level in between the $H1$ and $E1$ bands and explore the interesting regime of strongly coupled electron-hole systems. It should be noted that only in a double-gate geometry one can change both, the overlap between the subbands, and hence the position of the hybridization gap in k-space, as well as the position of the Fermi level, to an arbitrary value. In other words, in order to control these two degrees of freedom in the energy spectrum, one needs to have access to two different experimental knobs, in this case front and

back gates. Note that the absolute value of the gate biases determines the position of the Fermi level, while the relative difference between the biases determines the overlap of the $H1$ and $E1$ bands.

Finally, double-gated CQWs, originally proposed by Naveh and Laikhtman [35] and experimentally demonstrated by Cooper et al [37] offer unprecedented control of the CQWs' band structure and allow us to place the Fermi level into the hybridization gap. In this regime, as previously discussed, due to the strong electron-hole coupling and resultant carrier hybridization, the longitudinal resistance exhibits strong resistance peaks, which have been previously observed by Cooper et al [37]. More importantly, the mini-gap is the regime where some fascinating and novel phases of matter are predicted to occur.

2.4 QSHE in InAs/GaSb CQWs

2.4.1 Theory

Recent theoretical calculations [8] suggest that InAs/GaSb CQWs in the inverted regime should exhibit the QSH phase, which is characterized by an energy gap in the bulk and protected gapless edge modes. The edge modes in InAs/GaSb arise due to the inverted structure, i.e. the energy gap between the conduction and valence states is "negative" in the bulk of the sample. However, outside of the sample in vacuum or insulator, the energy difference between the conduction and valence states is always positive. In other words, the confinement potential for electrons is always pointed

upwards in energy, while for the holes the confinement potential of the sample is pointed downwards in energy. For the inverted structure, a smooth connection of energy states outside and inside of the sample necessarily leads to gap closing at the boundary and thus guarantees the existence of gapless edge modes. This is demonstrated in Fig. 2.6, which schematically shows the energy spectrum of the normal and inverted band structure in real space. If we place the Fermi energy into the gap, then in the case of the normal structure, the Fermi energy stays in the gap for the entire sample, while for the case of the inverted structure, the Fermi energy will necessarily cross the energy states at the sample edges [58].

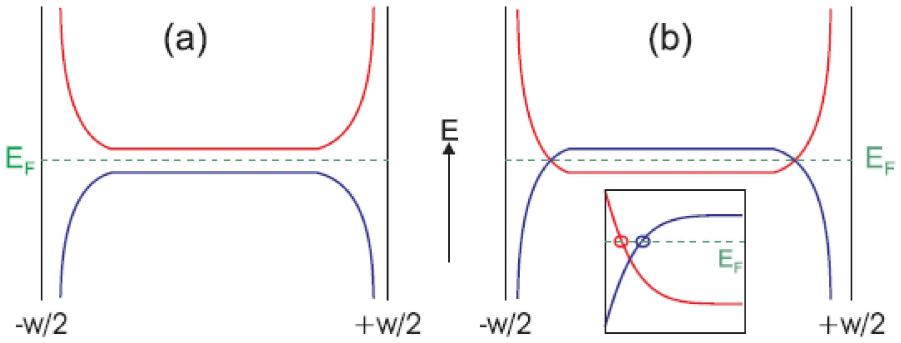

Figure 2.6 : Energy spectrum in real space for normal regime in a) and inverted regime in b). The confinement potential for electrons and holes has opposite direction. For the inverted structure and Fermi level E_F in the gap, E_F crosses energy states at edges, while for the normal regime E_F stays in the gap for the entire width of the sample [58].

In addition, in a slightly different picture, the energy of lifting up one electron from the valence band and placing it into the conduction band, i.e. the gap energy, can be related to the mass by Einstein's equivalence principle. This Einsteinian mass will be negative inside the sample due to the band inversion, while outside of the sample

this mass is naturally positive. As a result, the smooth connection of this mass inside and outside of the sample indicates that at the edges the mass will be zero. As a consequence, similarly to photons, which also have zero Einsteinian or rest mass, edge modes must have linear dispersions, i.e. $E \sim k$. As a consequence, inverted structure necessarily invokes edge modes with linear dispersion; however, inverted structure alone does not necessarily guarantee the protection of such linerarly dispersed edge states, which is a signature mark of the QSH phase.

This protection comes from the time-reversal symmetry of the system. The Hamiltonian of the system is a general function of momenta, spin and position operators, such that $H = H(p^2,\ \overrightarrow{s} \cdot \overrightarrow{p},\ \overrightarrow{r})$, where $\overrightarrow{p}$ is the momentum, $\overrightarrow{s}$ is the spin, and $\overrightarrow{r}$ is the position operator. The first term is related to the kinetic energy, the second describes spin-orbit coupling, while the last term describes the role of different potentials which generally only depend on $\overrightarrow{r}$. Under time reversal, $\overrightarrow{p}$ and $\overrightarrow{s}$ change sign while $\overrightarrow{r}$ stays the same. As a result, a Hamiltonian of this form will be invariant under time-reversal, unless we apply a magnetic field, which breaks this symmetry because $\overrightarrow{p} \rightarrow \overrightarrow{p} + e\overrightarrow{A}$ where $\overrightarrow{A}$ is the vector potential and does not change sign under time reversal. Furthermore, Kramers' theorem requires double degeneracy at the time reversal invariant points, which is in this case the middle of the Brillouin zone also known as the Γ point ($k = 0$), and thus, we must have a Kramers pair of edge modes at this point. Furthermore, in order to preserve time reversal, for $k \rightarrow -k$ we must have $s \rightarrow -s$, and hence edge states will be helical, with counter-propagating

spin up and spin down states.

A natural question to ask is whether helical edge states are stable against elastic backscattering. Very simple symmetry considerations indicate that the QSH phase has built-in protection against elastic backscattering. Consider, for example, scattering of the QSH state by a nonmagnetic impurity shown in Fig. 2.7. The reflected electron must rotate its spin by π in order to satisfy the time-reversal symmetry, as it goes around the impurity. However, there are two distinct paths, clockwise and counter-clockwise, and thus, the total phase difference between these two rotations will be 2π. However, upon a full 2π rotation, the wavefunction of a spin 1/2 particle changes sign, and thus, clockwise and counter-clockwise paths will interfere destructively [5]. This simple argument illustrates topological protection of the helical edge states and robustness of the edge modes against disorder. Nevertheless, this protection does not extend to higher-order processes, such as two simultaneous spin flips, as well as inelastic processes [16, 59, 60, 19, 61]. In addition, the role of time reversal symmetry in edge backscattering protection is not clear, with some authors suggesting that such protection may be independent of the symmetry if the confinement potential of the wells is sufficiently smooth [62]. This is of particular importance for the magnetic field dependence of the mini-gap resistance, which we discuss in Chapter 4.

So far the discusssion of the QSH effect and its proposal in InAs/GaSb has been mainly qualitative. However, real systems always exhibit additional complexities that

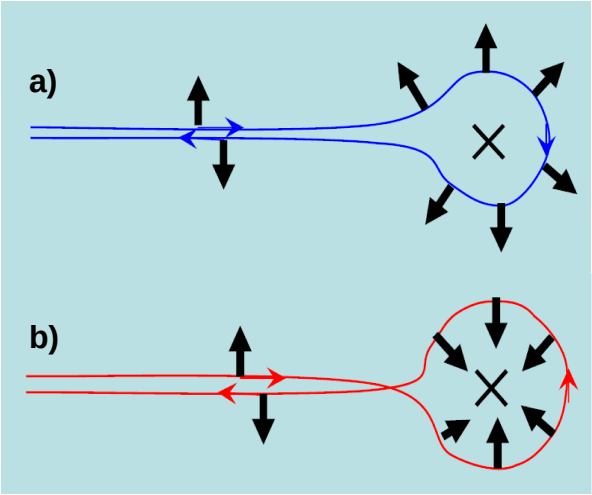

Figure 2.7 : Scattering of a quantum spin Hall edge state around a non-magnetic impurity. Due to time reversal symmetry the spin rotates by π in the clockwise direction and $-\pi$ in the counterclockwise direction, with a total change in phase of 2π. Upon 2π spin rotation the wavefunction changes sign and the two paths interfere destructively [5].

simple arguments cannot adequatly address. As a result, we present the model of the QSH effect in InAs/GaSb as proposed by Liu et al [8]. A starting point for such a model is the 8-band $k \cdot p$ model, which is a standard model describing semiconductors with outer s-like and p-like bands around the Γ point. The eight-band model is comprised of two $s-$bands, $|\Gamma_6,\ m_J = \pm 1/2\rangle$, which form conduction states, and six $p-$bands which form valence states: heavy hole $|\Gamma_8,\ J = 3/2,\ m_J = \pm 3/2\rangle$, light hole $|\Gamma_8,\ J = 3/2,\ m_J = \pm 1/2\rangle$, and split-off band $|\Gamma_7,\ J = 1/2,\ m_J = \pm 1/2\rangle$ [63]. Without spin-orbit coupling, the Γ_8 and Γ_7 bands would be degenerate; however, due to $L \cdot S$ coupling, Γ_8 is lifted high above the Γ_7 band. Furthermore, due to quantization effects in quantum wells and spin-orbital interaction the band edge of Γ_8 band is further separated into light and heavy hole components because of different effective

masses. Fig. 2.4 shows that the experimentally relevant bands are only Γ_6, previously labeled as $E1$, and heavy hole Γ_8, which we labeled as $H1$, and hence we can describe the system in terms of a four-component spinor: $|E1,\ m_J = 1/2\rangle$, $|H1,\ m_J = 3/2\rangle$, $|E1,\ m_J = -1/2\rangle$, and $|H1,\ m_J = -3/2\rangle$.

If inversion symmetry and axial symmetry around the growth axis are conserved, then spin-up and spin-down components will be decoupled, and the effective Hamiltonian will be block diagonal and thus can be described in terms of two diagonal 2×2 blocks. The off diagonal blocks are zero as assumed. Due to the time reversal symmetry, the upper and lower diagonal blocks are time reversed to each other and hence we have:

$$H_{eff}(k_x,\ k_y) = \begin{pmatrix} H(k) & 0 \\ 0 & H^*(-k) \end{pmatrix}. \tag{2.5}$$

$H(k)$ is a 2×2 matrix of the form $H(k) = E(k)+d_i(k)\sigma_i$, $E(k)$ is a diagonal matrix, representing the uncoupled energy of the bands and is of the form $E(k) = C_0 + M_2k^2$, where C_0 takes into consideration the quantization energy, while M_2 is related to the inverse of the effective mass. Furthermore, σ_i are Pauli matrices, and the $d(k)\sigma_i$ term describes spin-orbit coupling of the bands, where $d(k)$ is a scalar function of k. The first two Pauli matrices have only off-diagonal elements and hence $d_{1,2}(k)$ connect states of different parity and hence must be odd under two-dimensional spatial inversion. As a result, to lowest order $d_{1,2}(k) = A{\cdot}k$. On the other hand, σ_3 is diagonal

and thus $d_3(k)$ connect states of the same parity, and consequently, must be an even function in k. With convenient rearranging and re-labeling of some of the coefficients, the Hamiltonian $H_{eff}(k)$ becomes [8]:

$$\varepsilon(k) + \begin{pmatrix} M_0 + M_2k^2 & A(k_x + ik_y) & 0 & 0 \\ A(k_x - ik_y) & -(M_0 + M_2k^2) & 0 & 0 \\ 0 & 0 & M_0 + M_2k^2 & A(-k_x + ik_y) \\ 0 & 0 & A(-k_x - ik_y) & -(M_0 + M_2k^2) \end{pmatrix}, \quad (2.6)$$

where $\varepsilon(k) = (C_0 + C_2k^2)\, I_{4\times4}$ matrix describes unimportant band bending, $2M_0 = -E_{g0}$ corresponds to the energy gap between bands and is negative in the inverted regime; M_2 describes the curvature of the bands and corresponds to the inverse of the effective mass, while A includes interband coupling to lowest order. Note that this model Hamiltonian is an extension of the two-band model given in Eq. (2.2) to include spin, with an important bonus. The Hamiltonian has the form of the Dirac relativistic equation in 2+1 dimensions, i.e. with the rest mass on the diagonal, with opposite mass for the electron (particle) and hole (antiparticle), and off-diagonal elements linear in momentum which couple electron (particle) and hole (antiparticle) of the same spin. As such, the InAs/GaSb CQW is a voltage-tunable graphene like system, in which the Einsteinian rest mass can be tuned from positive values (normal regime) to negative values (inverted regime). Of special interest is the critical point

where the band structure changes from normal to inverted and in this case the rest mass M_0 will be near zero for small k, and the bulk dispersion will be graphene-like with a single Dirac cone. In the inverted regime, this mass will be negative, and as previously discussed the smooth connection of this mass inside and outside of the sample leads to gapless edge states with a linear dispersion, protected by time reversal symmetry.

The underlying assumption of the model presented in Eq. (2.6) is that the system preserves bulk and structural inversion symmetry, which is generally not true in InAs/GaSb with its zinc-blende crystal structure and strong Rashba coupling [8]. In consequence, the different spin components in Eq. (2.6) will be coupled. Nevertheless, numerical calculations that include these effects indicate that such contributions cannot destroy the QSH phase, although they can certainly modify the quantum phase transition [8]. The outcome of such calculations is given in Fig. 2.8 for 81 Å InAs/100 Å GaSb CQW (normal regime), and 100 Å InAs/100 Å GaSb CQW (inverted regime), showing gapless edge states for the latter case.

Furthermore, because in a double-gated geometry the band structure of CQWs can be tuned from the normal to the inverted regime as discussed earlier, one can describe the relevant state of the system based on the front and back gate bias values, in the phase diagram shown in Fig. 2.9. The phase diagram is clearly separated into normal (in blue) and inverted regimes (in red). In the case when the system is in the normal regime and the Fermi level is in the gap, the system will be a normal insulator,

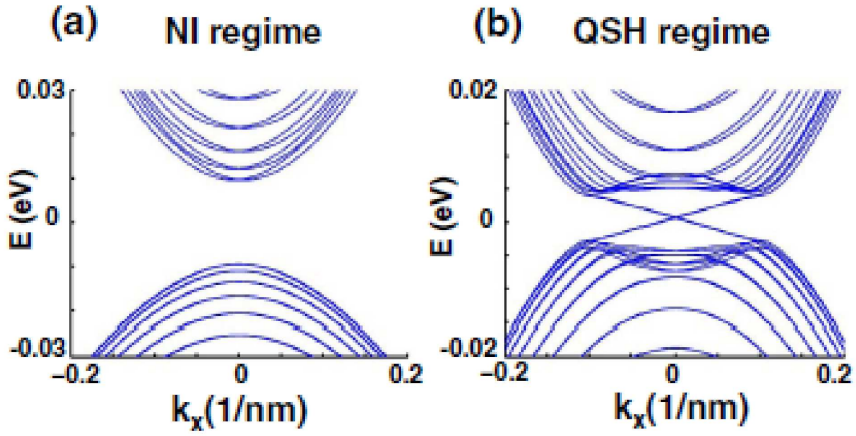

Figure 2.8 : Band dispersion obtained through tight binding calculations for 81 Å InAs/100 Å GaSb CQW (normal regime) in a), and 100 Å InAs/100 Å GaSb CQW (inverted regime) in b). Inverted structure shows gaples edge states with linear dispersion [8].

while when the Fermi level is in the gap of the inverted regime, then the system will exhibit a topologically insulating phase, with time-reversal protected edge states.

The primary goal of our experiments is to explore the phase diagram shown in Fig. 2.9, primarily in the inverted regime and towards the critical point, where the band structure changes from normal to inverted, fixing the Fermi level into the gap and looking for the QSH phase in transport measurements. However, before moving to the experimental section, it is necessary to discuss the transport signatures of the QSH phase.

2.4.2 Landauer-Büttiker Formula and Helical Edge States

As mentioned in the previous section, as long as time reversal symmetry is preserved, helical edge modes are protected from elastic backscattering due to destructive inter-

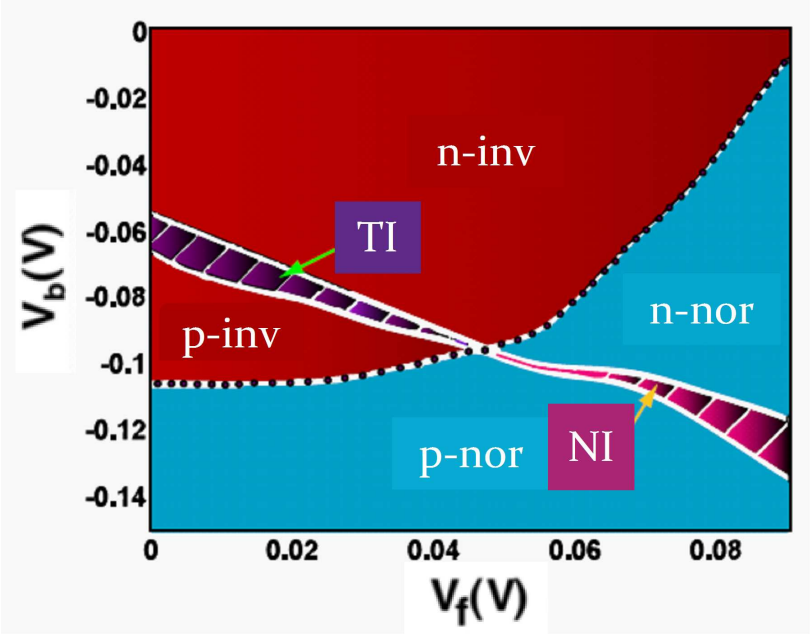

Figure 2.9 : Phase diagram of 100 Å InAs/100 Å GaSb CQW showing the TI phase in inverted regime (red) and the NI phase in normal regime (blue). For Fermi levels outside the gap, the system can be either n or p type [8].

ference of clockwise and counterclockwise spin rotation paths; however, an important caveat is that such wavefunction cancelation requires phase coherence. In any case, in the zero temperature limit, edge channels are perfectly ballistic and quantum transport in this regime can be described by the Landauer-Büttiker formula [64, 65, 66].

The Landauer-Büttiker formalism describes electrical transport in multiterminal devices in terms of transmission functions and is generally valid under two important constraints. The first constraint is that transport must be coherent across the device, i.e. a single wavefunction can be defined from one contact to another, and the second is that there should be no vertical flow of electrons from one energy to another [67]. In this case, the relationship between terminal current and voltage is:

$$I_p = \sum_q [G_{qp}V_p - G_{pq}V_q], \tag{2.7}$$

where q and p are contact labels, $G_{pq} \equiv \frac{2e^2}{h}\overline{T}_{p\leftarrow q}$ is conductance and $\overline{T}_{p\leftarrow q}$ is the transmission from contact q to contact p. In the case of QSH helical edge states this transmission probability is 1 for neighboring contacts, i.e. $\overline{T}_{p\leftarrow q}$=1 if q and p are neighbors, and edge states are not spin degenerate so $G_{pq} \equiv \frac{e^2}{h}\overline{T}_{p\leftarrow q}$ [58].

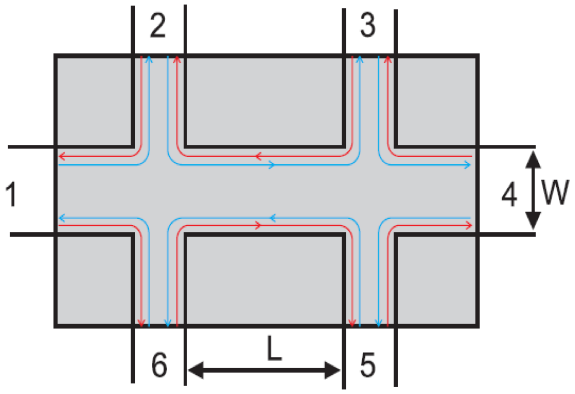

Figure 2.10 : Six-probe Hall bar device with depicted QSH edge states [58].

Thus, in the case of a six-probe device, also known as a Hall bar, shown in Fig. 2.10, the matrix G_{pq} will be:

$$G_{pq} = \frac{e^2}{h} \begin{pmatrix} 0 & 1 & 0 & 0 & 0 & 1 \\ 1 & 0 & 1 & 0 & 0 & 0 \\ 0 & 1 & 0 & 1 & 0 & 0 \\ 0 & 0 & 1 & 0 & 1 & 0 \\ 0 & 0 & 0 & 1 & 0 & 1 \\ 1 & 0 & 0 & 0 & 1 & 0 \end{pmatrix}, \tag{2.8}$$

giving the following system of linear equations:

$$\begin{pmatrix} I_1 \\ I_2 \\ I_3 \\ I_4 \\ I_5 \\ I_6 \end{pmatrix} = \frac{e^2}{h} \begin{pmatrix} 2 & -1 & 0 & 0 & 0 & -1 \\ -1 & 2 & -1 & 0 & 0 & 0 \\ 0 & -1 & 2 & -1 & 0 & 0 \\ 0 & 0 & -1 & 2 & -1 & 0 \\ 0 & 0 & 0 & -1 & 2 & -1 \\ -1 & 0 & 0 & 0 & -1 & 2 \end{pmatrix} \begin{pmatrix} V_1 \\ V_2 \\ V_3 \\ V_4 \\ V_5 \\ V_6 \end{pmatrix}. \tag{2.9}$$

By setting one of the voltages to zero and using the conservation of current, one row and one column can be eliminated. In this case, we choose to ground $V_4 = 0$ and we pass the current from 1 to 4. Contacts 2, 3, 6, and 5 are voltage measurement contacts and we have: $I_2 = I_3 = I_5 = I_6 = 0$. Solving for the remaining variables, we have:

$$I_1 = \frac{2e^2}{h}(V_2 - V_3) \qquad \text{and} \qquad \mathrm{G}_{14,23} = \frac{2e^2}{h}. \tag{2.10}$$

Thus, measuring the four probe conductance in the six-terminal device, we would expect to observe conductance quantized to a value of $\frac{2e^2}{h}$. However, Eq. (2.10) is valid only when the conductor is phase coherent. For samples whose size is larger than the phase coherence length, $L \gg L_\phi$, we can estimate the conductance by dividing the conductor into phase coherent sections. This approach is due to Büttiker, who was the first to note that voltage probes can serve as phase-breaking scatterers [66]. Thus, for longer devices, we can still use the Landauer-Büttiker formula if we account for the lack of phase coherence by inserting phase-breaking probes between our measurement probes. As a result, for a sample of length L we place $N = \frac{L}{L_\phi} - 1$ phase-breaking probes between contacts 2 and 3 and similarly between contacts 6 and 5. Applying the Landauer-Büttiker formula from Eq. (2.7) to such a system of $2N + 6$ contacts in a similar fashion as demonstrated for six contacts, we obtain:

$$\mathrm{G}_{14,23} = \frac{2e^2}{h}\frac{1}{N+1} \qquad \text{or} \qquad \mathrm{G}_{14,23} = \frac{L_\phi}{L}\frac{2e^2}{h}. \tag{2.11}$$

In consequence, in order to observe conductance quantization, which is a signature of the QSH effect in transport measurements, one needs to make devices which are smaller than the phase coherence length, as illustrated by Eq. (2.11). In addition, for larger devices this relationship can also help us determine the phase coherence length of the edge states, which does not necessarily have to be the same as in the bulk. At any rate, we emphasize here that for macroscopic devices where $L \gg L_\phi$ edge conductance vanishes acording to Eq. (2.11), and hence there is no apparent differ-

ence in transport between macroscopic normal insulating and topologically insulating structures.

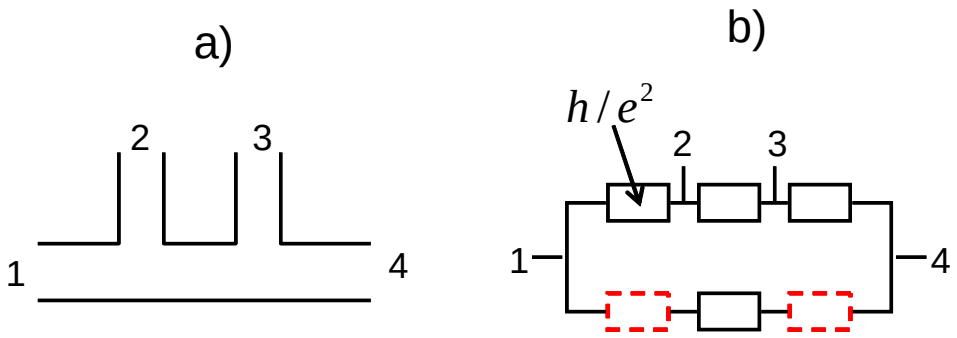

Figure 2.11 : Panel a) shows four-probe device in which edge conductance doubles to $G_{14,23} = \frac{4e^2}{h}$ as compared to six-terminal case. Panel b) shows equivalent resistance circuit. When the bottom two electrodes are removed from six-terminal configuration, current in the upper branch is reduced by a factor of two, resulting in doubling of edge conductance.

Besides six-terminal Hall bar structures, experiments presented in this thesis are also performed on four-terminal structures because in such structures edge conductance doubles to $G_{14,23} = \frac{4e^2}{h}$ for mesoscopic devices. This comes directly from the Landauer-Büttiker formula given in Eq. (2.7) but can be understood quite simply based on the equivalent circuit structure given in Fig. (2.11). In this circuit, neighboring terminals are connected by a quantum of resistance h/e^2 and removing lower two voltage probes reduces the current through the upper branch by a factor of two, which reduces the voltage drop between the upper two leads and results in doubling of conductance as compared to the six-terminal case. Note that the above picture can be extended to devices where $L \gg L_\phi$ by placing $N = \frac{L}{L_\phi} - 1$ resistors of value h/e^2 in each current branch, giving four terminal edge conductance:

$$G = \frac{2e^2}{h}\left[\frac{L_\phi}{L} + \left(\frac{L_\phi}{L}\right)^2\right]. \tag{2.12}$$

Similar to the six-terminal case, here edge conductance also vanishes in the macroscopic limit, reiterating the earlier point that there is no apparent difference in transport measurements between normal and topological insulators in macroscopic devices, i.e. in both cases conductance is vanishingly small, and that the number of contacts in this limit is irrelevant, although two cases certainly exhibit different functional dependence on the device length.

Nevertheless, at least in the mesoscopic limit the transport in QSH devices is nonlocal and this has some profound consequences on transport behavior of the system. One rather apparent corollary is that even the probes, which are outside the voltage measurement contacts, i.e., outside of contacts 2-3 and 5-6 in Fig. 2.10, can affect the voltage measurement between leads 2-3 and 5-6. For example, if we put an additional contact (see Fig. 2.10) between probes 5 and 4, and again pass the current from 1 to 4 and measure the voltage drop in between probes 2 -3, and 5-6, we obtain:

$$\mathrm{G}_{14,23} = \frac{7}{4}\frac{e^2}{h} \qquad \text{or} \qquad \mathrm{G}_{14,65} = \frac{7}{3}\frac{e^2}{h}. \tag{2.13}$$

Hence, the simple Landauer-Büttiker formula suggests that the presence of even one phase breaking center, and even outside measuring contacts, can introduce a

variation from the expected quantized value of $\frac{2e^2}{h}$. This may explain some of the fluctuations in six-probe measurements in HgTe/CdTe [32] and indicates that due to the potential fluctuations in gating and other imperfections of real samples, for example variation of the QW thickness across the wafer, perfect quantization cannot be expected for helical edge modes. In addition, we note here an important comparison to the chiral edge transport in QHE, which is also non-local, but does not show such sensitivity to phase breaking centers. In chiral edge modes the value of the transverse and longitudinal conductance is independent of the number of voltage probes or phase-scattering centers between the measuring probes. Hence, quantization will be perfect, regardless of the presence and distribution of local phase-scatterers. This comes directly from applying the Landauer-Büttiker formula to chiral edge states in a similar way as presented in this section for the helical modes, except that $G_{pq} \equiv \frac{2e^2}{h}\overline{T}_{p\leftarrow q}$, where in this case $\overline{T}_{p\leftarrow q} = 1$ only for neighboring contacts in one direction. In conclusion, helical edge states, although having a non-local property, are not as robust as chiral edge states, and as revealed by the Landauer-Büttiker formalism, this illustrates a simple, yet fundamental difference between a two-way and one-way traffic.

2.5 Previous Experimental Work

Before we delve into our experimental findings it is useful to quickly review previous experimental work in light of the theoretical proposal by Liu et al [8]. Mini-gap opening due to electron-hole hybridization has been first experimentally established

in capacitance and transport measurements by Yang et al [36], who have studied front-gated InAs/GaSb composite QWs in both inverted and normal regimes. Furthermore, evidence for the hybridization gap has been presented in far-infrared measurements of Kono et al [38] and later Yang et al [39]. Similarly, transport experiments by Cooper et al [37] on double-gated structures have shown strong resistance peaks, corresponding to the hybridization gap; however, Cooper et al have found that the resistance of the mini-gap does not diverge and does not show thermal activation, as may be expected for a purely insulating system, and have ascribed this oddity to possible band anisotropy and impurity states within the mini-gap. In fact, in the earliest study, it has been found by Yang et al [36] that capacitance signal, which corresponds directly to the density of the states, exhibits only a slight dip in the hybridization gap, compared to large reduction of density of states in the normal gap, presumably due to localized states present in the hybridization gap but curiously absent in the normal gap of similar size.

These early studies have all been performed on macroscopic samples, and based on the analysis given in the previous section, possible edge contributions to the observed finite gap conductivity in these studies can be safely excluded. As a result, finite mini-gap conductivity in these experiments must be understood as a predominantly bulk effect, and as such has been theoretically studied by Naveh and Laikhtman [40], who considered tunneling between the wells to be dissipative, albeit slightly. In early theoretical studies, Caldeira and Legett [68] have found that dissipation,

i.e. coupling of the quantum mechanical particle to external degrees of freedom, will lead to a reduced quantum mechanical capacity of the particle for tunneling. Thus, dissipative tunneling will leave some proportion of electronic states non-hybridized, giving nonzero density of states in the gap and finite gap conductivity. Suprisingly, only a slight amount of electron and hole level broadening leads to drastic changes in transport behavior, giving finite bulk conductivity even at zero temperature and even in the limit when level broadening is much smaller then the size of the mini-gap [40]. Nevertheless, for negligible level broadening, mini-gap bulk conductivity depends exclusively on band parameters. We further explore this subtle issue of bulk mini-gap conduction in the following chapter.

Chapter 3

Bulk Transport in Hybridized InAs/GaSb QWs

3.1 Sample Fabrication and Experimental Setup

The InAs/GaSb CQW sample was grown by molecular beam epitaxy on a silicon-doped $N^+(100)$ GaAs substrate. The structure, which is shown in Fig. 3.1, consists of a standard buffer with AlSb and $Al_{0.8}Ga_{0.2}Sb$ layers which compensates for about seven percent lattice mismatch between GaAs and AlSb [69]. On top of this, a 500 Å AlSb lower barrier layer was grown, followed by 150 Å InAs and 80 Å GaSb quantum wells with a 500 Å AlSb top barrier layer and a 30 Å GaSb cap layer.

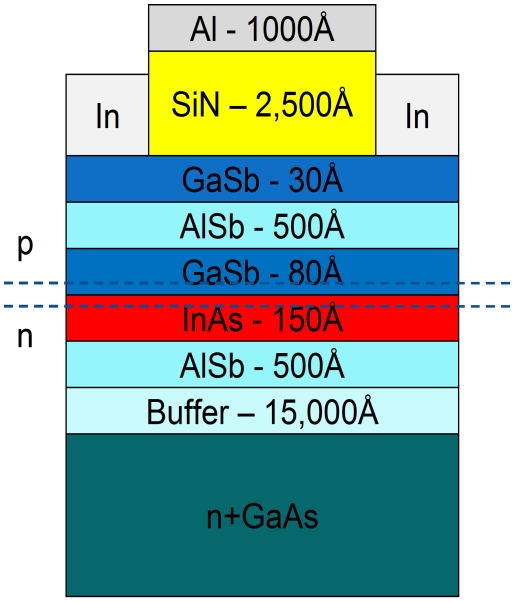

Figure 3.1 : Sample structure. 2D electron and hole gases are marked by dash lines and labeled as n and p, respectively.

Our experiments were performed on Hall bar samples from the same wafer, and were processed using standard photo- and e-beam lithography with wet etching. Fig. 3.2 sketches the fabrication steps. A lithographically defined mesa was etched with a phosphoric based etchant, and subsequently, a 2500 Å Si_3N_4 layer was deposited using plasma enhanced chemical vapor deposition. This layer serves as both a protection layer, as well as the dielectric for the front gate. Contact windows were etched through the Si_3N_4 layer and ohmic contacts to the electron-hole layers were made with indium and without annealing. A 1000 Å Al or Ti/Au front metal gate was evaporated on top of the dielectric, while the N^+GaAs substrate serves as a back gate for our devices and was contacted using silver resin.

Here we present data on Hall bar samples of two different lengths with two distinct transport regimes. Sample A is a Hall bar with a width and length of $10\,\mu m \times 20\,\mu m$ and is in the diffusive regime, while sample B has a width and length of $0.7\,\mu m \times 1.5\,\mu m$, and as our data suggests, is in the mesoscopic regime. An optical image of sample A and an SEM image of the sample B are shown in Fig. 3.3, panel a) and b), respectively. Low temperature magnetotransport measurements were carried out in a ^{3}He refrigerator (300 mK) combined with a 12 T superconducting magnet, or in a ^{3}He/^{4}He dilution refrigerator (20 mK) with a 18 T magnet at the National High Magnetic Field Laboratory. A standard lock-in technique with an excitation current of 100 nA at 23 Hz was employed.

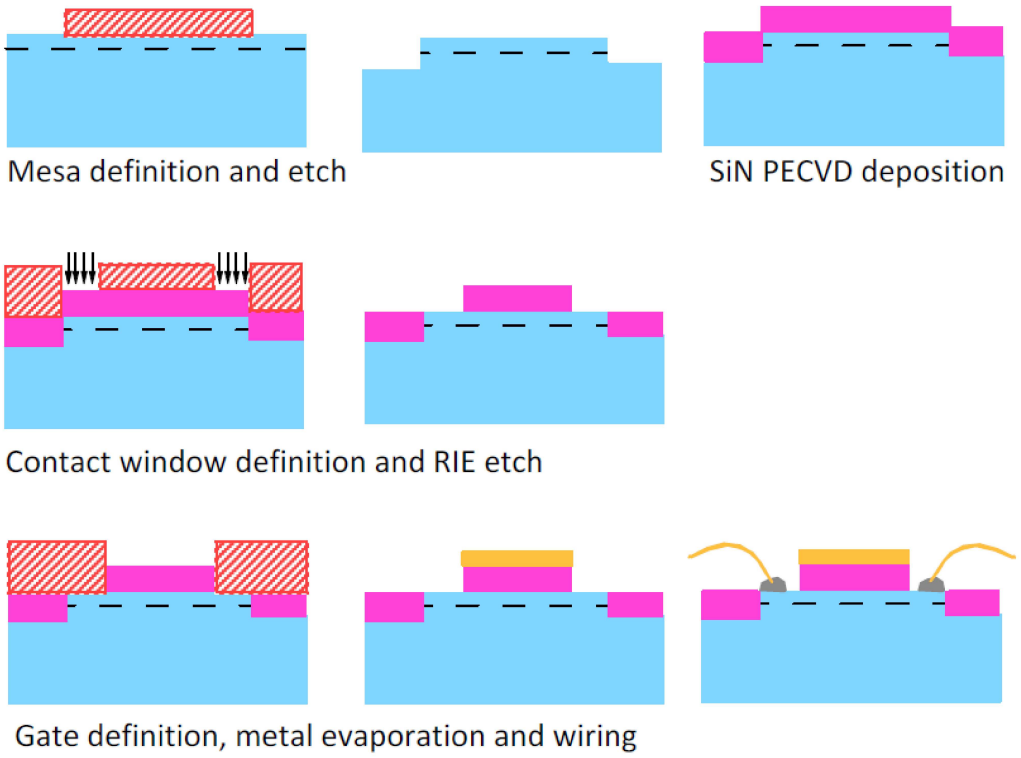

Figure 3.2 : Device fabrication steps.

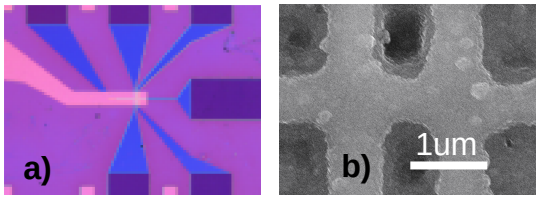

Figure 3.3 : Panel a) shows an optical image of a $10\,\mu m \times 20\,\mu m$ Hall bar, while panel b) shows an SEM image of a $0.7\,\mu m \times 1.5\,\mu m$ Hall bar (mesoscopic regime).

3.2 Sample Characterization

3.2.1 Single vs. Two-Carrier Transport

In the double-gate geometry, both the overlap between the subbands, E_{g0}, and the Fermi energy E_F can be tuned. Hence, not only the carrier density, but also the carrier character, i.e. electron or hole, can be changed. In fact, depending on the position of the Fermi level, the carriers can be electrons-only, holes-only, and both electrons and holes. Single and two-carrier regimes have distinct magnetoransport behavior, which becomes very important in sample characterization. In the single carrier regime, which occurs for either E_F above $H1$ (electrons) or below $E1$ (holes), the Hall or transverse resistance R_{xy} in the classical regime depends linearly on the magnetic field B according to:

$$R_{xy} = -\frac{B}{ne} \qquad \text{and} \qquad R_{xy} = \frac{B}{pe}, \tag{3.1}$$

for electrons and holes respectively, where n and p are electron and hole densities. The longitudinal resistance at $B = 0\,\mathrm{T}$ is:

$$R_{xx} = \frac{1}{ne\mu_e}\frac{L}{W} \qquad \text{and} \qquad R_{xx} = \frac{1}{pe\mu_h}\frac{L}{W}, \tag{3.2}$$

where $\frac{L}{W}$ is the ratio of Hall bar section length to the section width and $\mu_{e,h}$ are electron and hole mobilities. Thus, in the single carrier regime, electron or hole densities can be determined from the slope of the Hall resistance, while the carrier

mobility is extracted from the zero-field longitudinal resistance, as described by Eqs. (3.1) and (3.2).

Furthermore, for single carrier transport, the carrier density can be obtained from Shubnikov-de Haas oscillations (SdH) of R_{xx} in a magnetic field. The constant density of states of a two-dimensional electron gas (2DEG) or a hole gas (2DHG), separates into Landau levels, each with density per unit area equal to eB/h. Because the carrier density is fixed, the number of filled Landau levels, also known as filling factor will be: $\nu = \frac{nh}{Be}$. When the Fermi level lies in a Landau level, the density of states will be high, and the conductivity, which in a magnetic field is proportional to the resistivity, will be high as well. Thus, peaks in SdH oscillations correspond to Landau level filling and from the relative separation of the R_{xx} peaks in $1/B$ single carrier density can be determined as [70]:

$$n = \frac{\Delta\nu}{\Delta\left(\frac{1}{B}\right)\frac{h}{e}}, \tag{3.3}$$

where $\Delta\nu = 2$ if the spin degeneracy is not lifted, which is generally true in moderate magnetic fields.

On the other hand, two-carrier transport occurs for E_F between $H1$ and $E1$, and hence, electrons and holes coexist in their respective layers. This regime is marked by a non-linear dependence of the Hall resistance, R_{xy}, on the magnetic field, B and

in independent electron-hole classical model R_{xy} is given as [71]:

$$R_{xy} = \frac{B\left[(p - nb^2) + \mu_e^2 B^2 (p - n)\right]}{e\left[(bn + p)^2 + \mu_e^2 B^2 (p - n)^2\right]}, \tag{3.4}$$

where $b = \frac{\mu_e}{\mu_h}$. Note that in the limit of high magnetic fields, i.e. $B \gg \frac{1}{\mu_e}$, $R_{xy} \approx \frac{B}{(p-n)e}$ and the net carrier density can be determined from the slope of the Hall resistance in a magnetic field. The longitudinal resistance at $B = 0\,\mathrm{T}$ is given by:

$$R_{xx} = \frac{1}{e\left(n\mu_e + p\mu_h\right)} \frac{L}{W}. \tag{3.5}$$

In the two-carrier regime, carrier densities and mobilities are extracted by fitting Eq. (3.4) and using Eq. (3.5) as a fit constraint. In conclusion, even in the classical regime and assuming that electrons and holes are independent, single and two-carrier regimes show a different dependence of transport coefficients in magnetotransport, which is important from a transport characterization perspective. We note here that Eqs. (3.4) and (3.5) are not valid when electrons and holes are coupled [40], which is the case in our samples for Fermi energies near the hybridization gap.

3.2.2 Sample Characterization at Zero Gate Bias

In our CQW, the Fermi level is pinned by the surface states in the GaSb cap layer some 130 meV above the bottom of the InAs bulk conduction band [49]. In consequence, under zero applied bias or in ungated samples, only electrons are present in the well.

In this case, using the expressions from the previous section, the low temperature electron density is determined to be approximately $7 \cdot 10^{11}\mathrm{cm}^{-2}$, while the electron mobility is $9 \cdot 10^4\,\mathrm{cm}^2/\mathrm{Vs}$. Fig. 3.4 shows representative magnetotransport data in the electron transport regime for a larger Hall bar sample (sample A) and a smaller Hall bar sample (sample B) at $T = 0.3\,\mathrm{K}$. In the larger sample SdH oscillations can be observed in R_{xx} starting at 1.8 T with no evidence of parallel conduction, while the Hall resistance varies linearly with magnetic field until the appearance of quantum Hall plateaus. As described earlier, this is indicative of the single carrier regime.

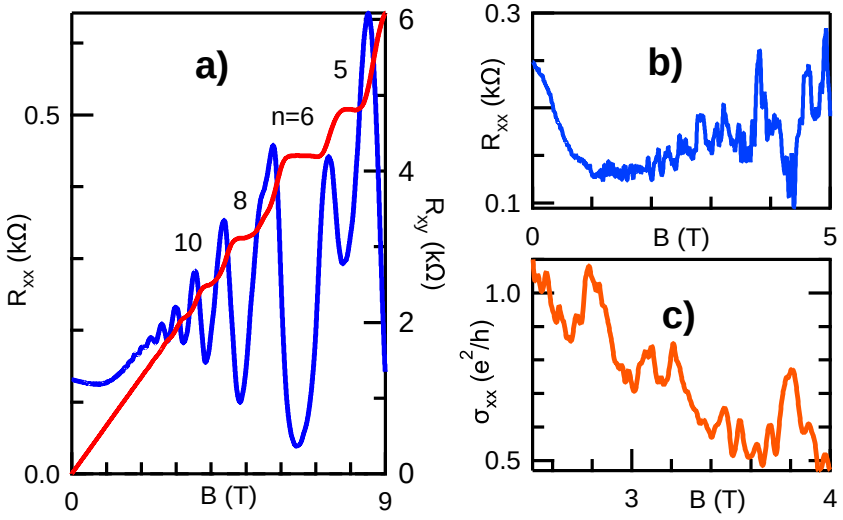

Figure 3.4 : Magnetotransport data at $T = 0.3\,\mathrm{K}$ is shown in a) for a $10\,\mu\mathrm{m} \times 20\,\mu\mathrm{m}$ (sample A), and in b) for a $0.7\,\mu\mathrm{m} \times 1.5\,\mu\mathrm{m}$ (Sample B) Hall bar where R_{xx} exhibits strong fluctuations. c) The fluctuations in conductivity (sample B) are on the order of e^2/h, indicating mesoscopic regime [41].

In contrast to larger samples which show clear SdH, micron-size devices show strong fluctuations in R_{xx} at low temperatures. Fluctuations are reproducible in magnetic field, and decrease in magnitude for higher temperatures, disappearing at

around 10 K. As shown in Fig. 3.4 c), the conductivity varies on the order of e^2/h, indicating a mesoscopic regime. This is more evident by estimating the coherence length from the size of the conductance fluctuations. A very rough estimate of the size of conductance fluctuations is given as [67]: $\delta g \sim \left(\frac{L_\phi}{L}\right)^{\frac{3}{2}} \frac{e^2}{h}$, where L_ϕ is the coherence length and L is the length of the sample. Using the latter expression, $L_\phi \sim 1\,\mu$m, and is on the same order as the sample B length, which is a necessary requirement for observing transport signatures of QSH edge modes.

3.2.3 Gate Characterization

When applying a voltage bias on the front and back gates, the carrier density will change as described in Chapter 2. When only electrons are present in the well, the electron density changes linearly with the front bias as approximately $1.5{\cdot}10^{11}\text{cm}^{-2}/\text{V}$ and with the back gate bias as $0.4 \cdot 10^{11}\text{cm}^{-2}/\text{V}$. Electron densities are extracted by sweeping gate biases at a fixed magnetic field or through analysis of SdH oscillations. The values are consistent and agree well with the parallel plate capacitor model described in Chapter 2.

Extracting the densities and mobilities of the holes is not as straightforward as those of electrons, because in this particular structure, when induced, holes always coexist with electrons in the device bias range. Thus, the analysis of carrier densities and mobilities is complicated by the non-linear form of the two carrier transport Eq. (3.4). In principle, four parameters describing electron/hole densities and mobilities

can be extracted from fits to the Hall resistance with Eq. (3.4), assuming non-interacting electrons and holes [71]. In practice, such fits are rather sensitive to the fitting parameters and data range, and inherently flawed due to the electron-hole coupling [40]; nevertheless, far from resonance, coupling effects are weak, and the change of the hole density with the front gate bias is consistent with the value for unscreened electrons and in agreement with the parallel plate capacitor model.

Fig. 3.5 shows Hall resistance R_{xy} versus the perpendicular magnetic field B, with the front gate bias V_{front} varied from 0 V to -10 V in 1 V steps. At $V_{front} = 0$ V, R_{xy} varies linearly with B for small fields, while at higher fields quantum Hall plateaus develop, indicating exclusively electron type transport. At $V_{front} = -1$ V, R_{xy} still varies linearly with B, but with a larger slope, indicating electronic transport with a smaller carrier density, in agreement with Eq. (3.1). On the other hand, at $V_{front} = -2$ V Hall resistance starts to bend downwards at higher fields, suggesting two-carrier transport described by the Eq. (3.4). This trend continues as V_{front} is made more negative, and at very negative biases and large magnetic fields, R_{xy} changes its sign, indicating a two carrier-hole dominated regime. In consequence, carrier character in our system can be changed via V_{front} from electron-only to hole-dominated, thus allowing us to tune the Fermi energy through the hybridization gap as advertised earlier.

This is further illustrated in Fig. 3.6, where we conveniently plot B/eR_{xy} vs. V_{front}, for various back gate biases V_{back} and for a fixed magnetic field of $B = 1$ T. In the

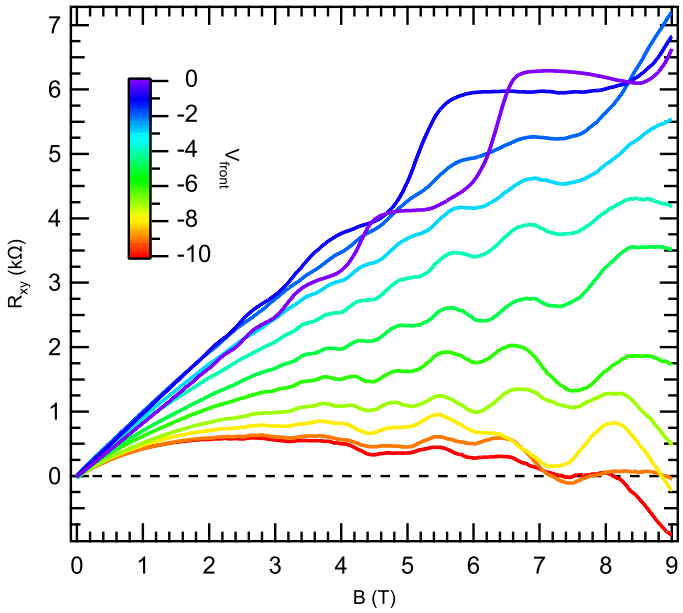

Figure 3.5 : Shows Hall resistance R_{xy} versus the perpendicular magnetic field B in sample A, while the front gate bias V_{front} is varied from 0 V to −10 V in 1 V steps. Bending of the Hall trace at more negative biases indicates coexistence of electrons and holes in transport. Carrier character in our system can be changed from electron-only to two-carrier hole-dominated.

single-carrier regime, B/eR_{xy} corresponds to the electron density and changes linearly with the applied bias. For a more negative front gate bias, B/eR_{xy} curve is non-linear indicating two-carrier transport, and in this regime B/eR_{xy} does not correspond directly to the carrier density. However, we can further simplify Eq. (3.4) by noting that the B^2 terms are comparably small, and when $p \ll nb^2$, we have that $B/eR_{xy} \approx n + \frac{2p}{b}$, where b can be fitted to $b \approx 6$. Once we start inducing holes in the GaSb well, the electron density stays approximately constant due to the screening from the top hole layer, while the hole density increases linearly [72]. As a result, the minimum in the B/eR_{xy} curve approximately corresponds to the minimum carrier density of the system, and hence resonant carrier density, i.e. $n \sim p$. In summary, in our devices the carrier character can be changed from electrons-only to predominantly holes, indicating that the Fermi level can be tuned from the conduction band to the valence band, and hence through the hybridization gap whose transport properties we aim to study. Before we proceed to this goal, a note regarding unavoidable hysterisis in our gated devices is in order.

As previously mentioned, our gates exhibit some hysterisis in up and down gate bias sweeps, especially if large biases are applied. This is due to the charge trapping sites at the interface of the semiconductor and the dielectric for the front gate, or at the interface between different semiconductors in the case of the back gate. At the interface, surface states exist, usually somewhere in the bulk energy gap. As a positive gate bias is applied, the Fermi level is lifted above the surface states due to

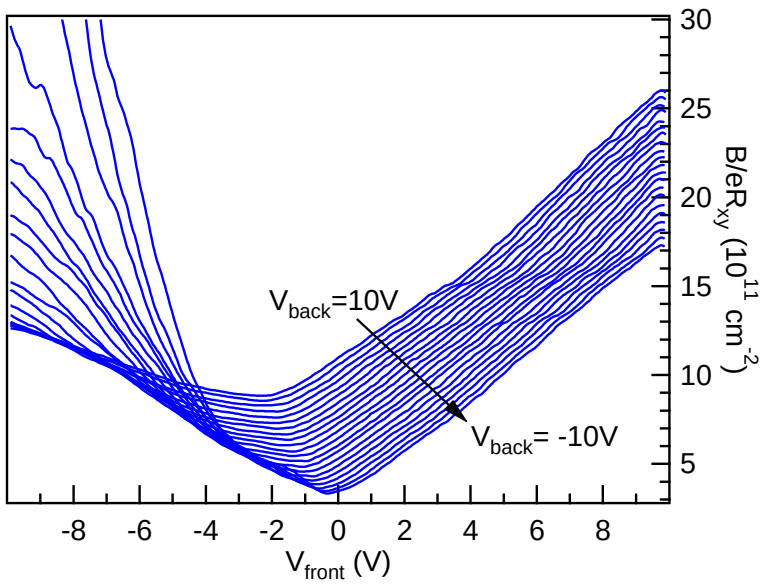

Figure 3.6 : Shows $^{B}/_{eR_{xy}}$ vs. front gate bias at $T = 0.3\,\mathrm{K}$, $B = 1\,\mathrm{T}$, Sample B. Back gate bias is changed from 10V to -10V in 1V steps. In linear regime, $^{B}/_{eR_{xy}}$ corresponds directly to electron density, while non-linear regime indicates two-carrier transport.

band bending, which results in their filling, and in this case, the effect of the gate on the 2DEG/2DHG is screened. On the other hand, when the Fermi energy is lowered below the surface states, these states become empty and the density of the modulated 2DEG/2DHG changes immediately with the gate bias. However, for more negative biases, electrons will tunnel from the surface to the 2DEG, providing a lower limit on the carrier density in the quantum well.

Hence, the variation of the carrier density with the gate bias will inherently possess memory, and the degree of such hysterisis depends on the density of surface states, which in antimonides is unfortunately rather high, some $10^{12}\mathrm{cm}^{-2}$ [73]. This might be unacceptable from a device point of view, and potential applications necessitate

the resolution of this important issue; however, from our perspective of fundamental physics, where a conceptual framework is studied and basic premises are tested, hysterisis is merely an experimental nuisance which must be carefully taken into account. In our case, and as evident from the above discussion, hysterisis is reproducible in full cycles of gate bias as long as the range of gate bias is unchanged, and this property is utilized to preserve the consistency of our measurements.

3.3 Resistance Peaks and Existence of Hybridization Gap

As demonstrated in the previous section, in our devices the Fermi level can be swept through the hybridization gap, and in this case, due to the strong electron-hole coupling, we observe strong resistance peaks in R_{xx}, shown in Fig. 3.7 as solid lines for mesoscopic device (sample B). Similarly to Fig. 3.5, in this figure, we sweep the front gate bias from $-10\,\mathrm{V}$ to $10\,\mathrm{V}$, and change the back gate bias from $-10\,\mathrm{V}$ to $10\,\mathrm{V}$ in $1\,\mathrm{V}$ steps at $T = 0.3\,\mathrm{K}$, $B = 0\,\mathrm{T}$.

Peaks correspond to near equal electron-hole density in our system, i.e. $n \sim p$, although as discussed in Chapter 2, strictly speaking, the traditional paradigm of electrons and holes breaks down near resonance and one can question whether electron and hole density is a meaningful concept [40]. However, for the lack of better way, we will continue using electron and hole densities as the relevant parameters.

Clear peaks in R_{xx} indicate the existence of the hybridization gap; however, the size of the resonance peaks $R_{xx}(max) \lesssim 4.5\,\mathrm{k}\Omega$ is a few times smaller than the expected

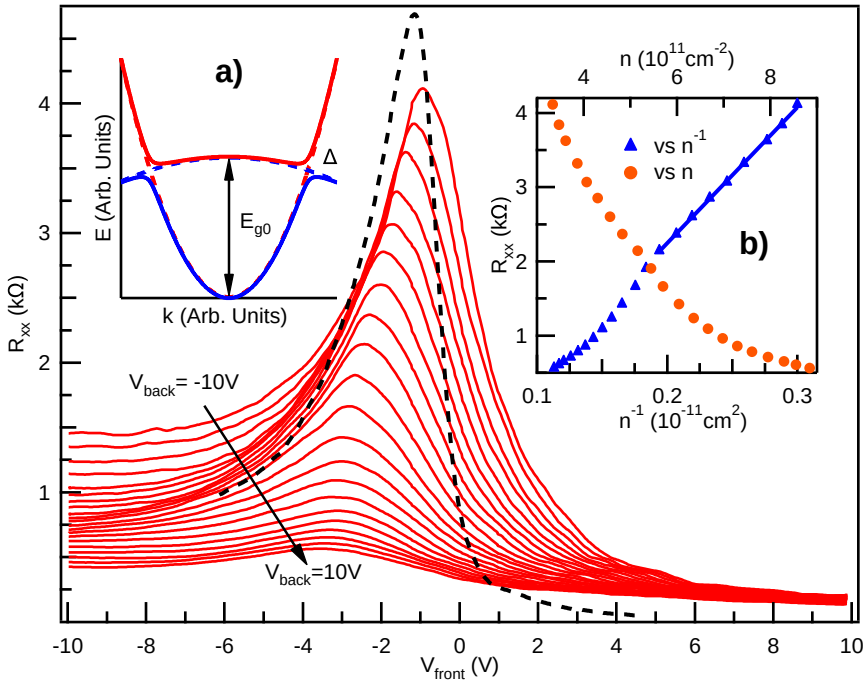

Figure 3.7 : Shows R_{xx} vs. V_{front} in sample B for V_{back} from 10 to -10 V, in 1V steps, $B = 0\,\mathrm{T}$, $T = 0.3\,\mathrm{K}$; and in sample A (dashed) for $V_{back} = -10\,\mathrm{V}$. Inset a) At the anti-crossing point, where $n \sim p$, a hybridization gap Δ opens. For E_F in the gap, R_{xx} exhibits resonance peaks, which decrease for increasing V_{back}. b) Resonance peaks vary lineary with n^{-1} for $n \lesssim 5 \cdot 10^{11}\mathrm{cm}^{-2}$ [41].

contribution from the edge of $\sim \frac{h}{2e^2} = 12.9\,\mathrm{k}\Omega$, and peak values strongly depend on the resonance carrier density. In fact, the resonance peaks, $R_{xx}(max)$, increase with decreasing back-gate bias, and hence, vary inversely with the resonance electron-hole density, $n_{cross} = n \sim p$ and corresponding k_{cross}(Fig. 3.7 a). In particular, for $n_{cross} \lesssim 5 \cdot 10^{11}\,\mathrm{cm}^{-2}$, the resonance peaks vary inverse proportionally with n_{cross} as shown in the inset of Figure 3.7 b). This inverse relationship, which we subsequently discuss, cannot be explained with an increasing mini-gap, for coupling between wells varies proportionally with k [53] as discussed in Chapter 2. Furthermore, the resonance carrier density n_{cross} can be related to the overlap between the electron and hole subbands E_{g0}, which is a more meaningful parameter in this case, as $E_{g0} = n_{cross}\frac{\pi\hbar^2}{m^*}$, where $m* = \frac{m_e m_h}{m_e + m_h}$ is the reduced mass, with carrier masses $m_e = 0.03$ and $m_h = 0.37$ (in units of free electron mass) [36]. As a result, the mini-gap resistance scales inversely with E_{g0}, which is in agreement with the bulk conductivity description given by Naveh and Laikhtman [40], upon which we elaborate in the later parts of the thesis.

Furthermore, larger Hall bars ($10\,\mu\mathrm{m} \times 20\,\mu\mathrm{m}$) also show a resistance peak of similar size, i.e.$\sim 4.5\,\mathrm{k}\Omega$, (shown in Fig. 3.7, dashed line). This behavior is in contrast to the case of HgTe/CdTe QWs where the quantized value is approached from larger resistances as the device length is reduced [32]. A lack of size dependence and inverse scaling of mini-gap resistance with E_{g0}, suggests that observed resonance peaks are predominantly a bulk effect, with a residual conductivity on the order of $10e^2/h$. This residual conductivity is a few times larger than the predicted contribution from the

edge and precludes the investigation of proposed edge modes in the current setup.

We note that Cooper et al [37] have reported a peak resistance value of $\sim 15\,\mathrm{k}\Omega$, which is close to $h/2e^2$. However, this value reflects only the bulk transport in the macroscopic samples used in their measurements, where $L \gg L_\phi$, and is consistent with our measurements if the geometric factor is taken into account. In conclusion, the strong resistance peaks are clear evidence for the existence of the hybridization gap; however, rather large conductivity indicates that the hybridization gap is not fully insulating in the bulk as a simple two-band model may indicate. In the next sections, we estimate the size of the mini-gap and investigate possible origins of residual bulk conductivity.

3.4 Resistance Dips and Size of the Hybridization Gap

Even in measurements at the lowest temperature, $T = 20\,\mathrm{mK}$ (Fig. 3.8 a), the resistance peak values do not change significantly and are approximately $\lesssim 5\,\mathrm{k}\Omega$ for mesoscopic samples, which is again at least 2-3 times smaller than $h/2e^2$. Thus, the residual bulk conductivity does not vanish even in the low temperature limit. However, measurements at very low temperature reveal another feature, which are dips in R_{xx} in the vicinity of resonance peaks, for $V_{back} < -9\,\mathrm{V}$, as shown in Fig. 3.8 a). This regime corresponds to small on-resonance carrier densities, and the observed dips can be explained by van Hove singularities in the DOS (Fig. 3.8 b) at gap edges [53]. In fact, this is the first time that such singularities have been observed in

transport, attesting to the high quality of our samples. Resistance dips occur only for smaller k due to the otherwise increasing anisotropy of the valence band, smearing out DOS singularities. When applying an in-plane magnetic field, as shown in Fig. 3.8 d), bands move in the k direction with respect to each other as: $\Delta k_{||} \approx \frac{eB_{||}\triangle z}{\hbar}$, where $\triangle z$ is the relative separation between 2DEG and 2DHG. In this case, the mini-gap opens at different $k-$values as shown in Fig. 3.8 d), and due to the induced gap anisotropy [36], DOS singularities are expected to be smeared out and resistance dips should weaken, as observed in Fig. 3.8 c).

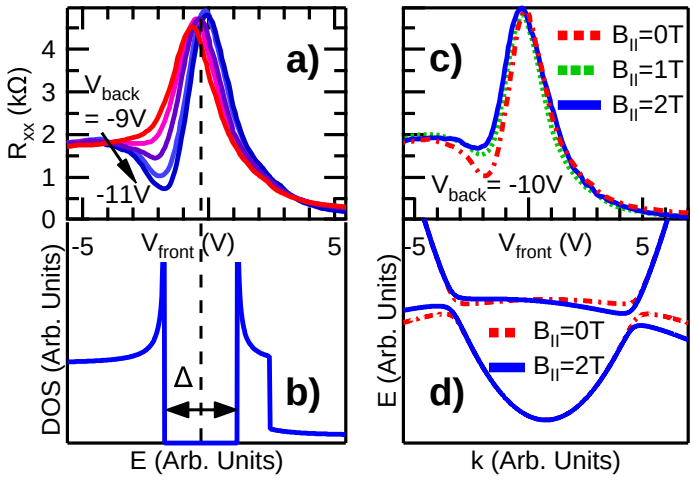

Figure 3.8 : a) Shows R_{xx} vs. V_{front} in sample A for V_{back} from -9 to -11V, in 0.5 V steps, $B = 0$ T, $T = 20$ mK. Resistance dips occur at singularities in DOS near gap edges shown in b). From relative position of dips and peaks in V_{front} we determine $\Delta \approx 3.6$ meV. Dips weaken with in-plane magnetic field in c), due to induced anisotropy in the dispersion in d) [41].

It is worth mentioning that resistance dips have not been observed at $T = 0.3$ K in these structures, which is presumably due to the higher carrier density. At $T = 20$ mK density of carriers is on average ten to fifteen percent less than at $T = 0.3$ K due to

the carrier freeze out. Nevertheless, resistance dips can be used to estimate the size of the mini-gap from the relative position of resistance dips and peaks (Fig. 3.8) in the front gate bias as: $\triangle = 2\,(V_{peak} - V_{dip})\,\frac{\Delta n}{\Delta V}\,\frac{1}{DOS}$, where $\frac{\Delta n}{\Delta V}$ is the rate of carrier density change with the front bias, and $DOS = (m_e + m_h)/\pi\hbar^2$. We obtain $\triangle = 3.6\,\mathrm{meV}$, in agreement with previous studies [36, 37, 39].

3.5 Temperature Dependence of Resistance Peaks

A similar value of the hybridization gap can be deduced from the temperature dependence of the resonance peaks shown in Fig. 3.9. For temperatures varied from $T = 0.3\,\mathrm{K}$ to $T = 40\,\mathrm{K}$ the size of the resistance peaks decreases, indicating the insulating character of the hybridization gap. On the other hand, we do not observe temperature-activated resistance, as one would expect for a true insulator. Resonance peaks increase only by a factor of 2-3 over a three orders of magnitude change in temperature, for six anti-crossing points measured, and saturate for $T < 2\,\mathrm{K}$ as suggested by a $1/T$ plot of the resistance peaks. Nevertheless, peaks persist up to $40\,\mathrm{K}$ for all six cases, which is consistent with a gap value of $3 - 4\,\mathrm{meV}$. In conclusion, the temperature dependence of the resistance peaks confirms gap existence, albeit with non-vanishing residual bulk conductivity.

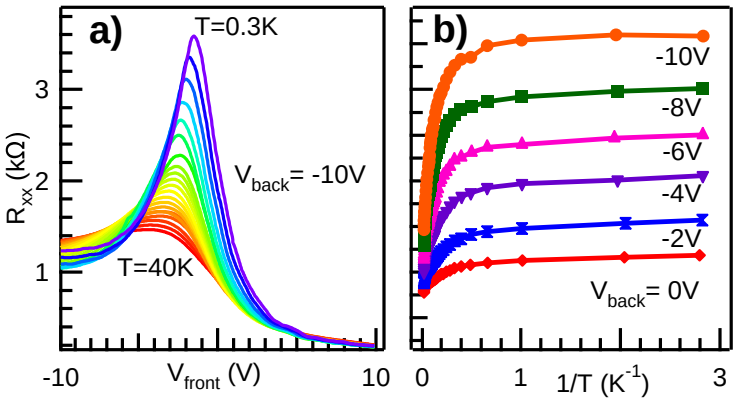

Figure 3.9 : a) Shows the temperature dependence of resonance peaks in sample A for V_{back}=−10 V for T from 0.3 K to 40 K consecutively in roughly 2 K steps. b) Resonance peaks shown vs T^{-1} saturate for $T < 2$ K, for six different k_{cross} [41].

3.6 Analysis of Scattering and Potential Fluctuations

So far we have established the existence of the mini-gap and estimated its size, noting that the mini-gap is not trully insulating as expected and as desired for observing the TI phase in this material system. Scattering and potential fluctuations in our samples induced by gating could be a likely culprit for the residual conductivity in a very trivial way, i.e. if the broadening of electron and hole energy levels due to the material imperfections is larger or comparable to the size of the hybridization gap. Thus, analysis of scattering and potential fluctuations is required in order to understand the nature of the observed resistance peaks.

Hence, we determine the carrier scattering times characterizing the transport in a zero magnetic field. At zero gate bias, the electron scattering time is $\tau_r = \frac{\mu_e m_e}{e} =$ 1.5 ps and the associated level broadening is $\Gamma_e = \hbar/2\tau_r = 0.2$ meV. The electron mobility shows a linear dependence on electron density and drops to approximately

$4{\cdot}10^4\,\mathrm{cm}^2/\mathrm{Vs}$ for the case of the smallest electron density of $3.3{\cdot}10^{11}\mathrm{cm}^{-2}$, giving $\Gamma_e = 0.5\,\mathrm{meV}$. The linear dependence of mobility on the electron density is indicative of short range scattering, presumably from dislocations at interfaces, which is confirmed by extracting the quantum time τ_q from the SdH oscillations [74, 75], giving $\tau_r/\tau_q{\approx}7$ at zero bias and validating the predominance of large angle scattering. The estimated τ_q has been corrected for density inhomogeneity [76] with a Gaussian width of $\delta n \approx 0.35 \cdot 10^{11}\,\mathrm{cm}^{-2}$. This suggests that the random potential fluctuations are on the order of $\delta E = \delta n/DOS \sim 0.25\,\mathrm{meV}$, and thus $\delta E \ll \Delta$. Here we briefly mention the procedure which is used to deduce the density inhomogeneity. We start from the semi-classical expression for Shubnikov-de Haas (SdH) oscillations given as:

$$\triangle R_{xx}(n) = R_0(n) \cdot e^{-\pi m_e/eB\tau_q} cos\left(\frac{\pi h}{eB} n - \pi\right), \tag{3.6}$$

which is further convoluted with a Gaussian distribution of carrier density and fitted to our data according to the following expression:

$$\triangle R'_{xx}(n_0) = \int dn \cdot \triangle R_{xx}(n) \cdot \frac{1}{\sqrt{2\pi}\delta n} e^{-\frac{(n-n_0)^2}{2\delta n^2}}. \tag{3.7}$$

For holes, $\Gamma_h = b\frac{m_e}{m_h}\Gamma_e$, where b is the ratio of electron to hole mobilities. From a fit to R_{xy} in the two-carrier transport regime, $b \approx 6$, giving $\Gamma_h = 0.3\,\mathrm{meV}$. Thus, the total level broadening is less than $\Gamma \leq \Gamma_e + \Gamma_h \approx 0.8\,\mathrm{meV}$, which is a few times smaller than the size of the gap. As a result, because the level broadening due to

scattering and potential fluctuations is smaller than the size of the hybridization gap, we conclude that disorder may play only a non-trivial role in the origin of residual conductivity. We clarify how this non-trivial role comes about in the following section.

3.7 Origin of Residual Conductivity - Discussion and Implications

In this section we primarily focus on the origin of residual gap conductivity and discuss its implications for the stability of the proposed edge modes. We consider band anisotropy, and level broadening due to scattering and potential fluctuations as possible sources of bulk mini-gap conductivity. We first note that the anisotropy of the heavy hole band may play a role in the gap anisotropy at the Fermi energy, which could lead to a residual conductivity. Anisotropy is more apparent for larger k_{cross} [53] and may explain the decrease of $R_{xx}(max)$ with larger n_{cross} (Fig. 3.7 b). To what extent such anisotropy would affect the gap value is a subject for numerical calculations with realistic materials parameters [77]. However, evidence for resistance dips indicate that at least in the small carrier density regime, anisotropy cannot be responsible for the observed residual conductivity. In fact, because dips disappear for a in-plane magnetic field of approximately 2 T, the size of the gap anisotropy for the observed case is < 1 meV. Thus, although anisotropy certainly plays an important effect for higher k_{cross}, for smaller wavevectors and hence lower densities, evidence for van Hove singularities suggests that the band anisotropy is weak and thus cannot

account for the rather large mini-gap conductivity.

On exactly the same grounds, because potential fluctuations induced by gating and associated density inhomogeneity would also destroy the resistance dips associated with DOS singularities, we argue that this contribution cannot explain large gap conductivity. In fact, estimates of potential fluctuations from the analysis of the SdH indicate that this contribution is more than an order of magnitude smaller than the size of the gap as well. Furthermore, analysis of the scattering parameters indicates that the level broadening due to disorder is smaller than the size of the gap as well. Finally, one can argue that the observation of resistance dips due to the DOS singularities indicates that level broadening in general cannot explain the residual conductivity in a trivial way, i.e. simply by smearing out the mini-gap.

This issue has been resolved theoretically by Laikhthman and Naveh [40] who studied the transport in the inverted regime of the InAs/GaSb system, concluding that even negligible but finite level broadening due to the carrier scattering will result in finite on-resonance conductivity at $T = 0\,\mathrm{K}$. Specifically, the residual conductivity will go as $g \sim \frac{e^2}{h}\frac{E_{g0}}{\Delta}$, when $\Gamma \ll \Delta \ll E_{g0}$, and is independent of scattering parameters. Since $E_{g0} = n_{cross}\frac{\pi\hbar^2}{m^*}$, where $m* = \frac{m_e m_h}{m_e+m_h}$, it follows that $R_{xx}(max) \sim n_{cross}^{-1}$ as observed in Fig. 3.7 b) for $n_{cross} \lesssim 5 \cdot 10^{11}\mathrm{cm}^{-2}$. In addition, in Fig. 3.10 we show bulk conductivity versus on-resonance carrier density showing both experimental values and theoretical estimates, giving good agreement at lower densities where the band anisotropy can be ignored. A discrepancy at larger densities is presumably due

to the band anisotropy, which for simplicity has been ignored in the Naveh-Laikhtman theory.

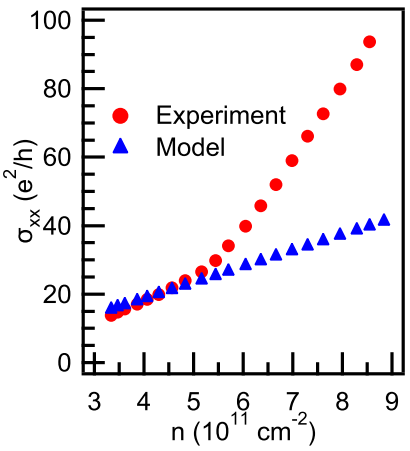

Figure 3.10 : Figure shows bulk conductivity versus anti-crossing density for both experiment and theory [40], giving a good agreement at lower densities where band anisotropy can be ignored.

The latter result can be understood by re-examining the original premise for carrier hybridization, which is the non-locality of electron states in the growth direction of the wells [78]. This non-locality can be suppressed through carrier scattering, i.e. coupling to external degrees of freedom, destroying carrier hybridization [68]. The relevant time-scale is the carrier tunneling time, $\tau_t = \hbar/2\Delta$, and in the relaxation time model, the total number of scattered carriers within τ_t will go as $n \cdot (1 - e^{-\frac{\tau_t}{\tau_r}})$, or equivalently as $n \cdot (1 - e^{-\frac{\Gamma}{\Delta}})$. Ignoring smaller contribution from scattered holes and using $\mu_e = \frac{e}{m}\frac{\hbar}{2\Gamma}$, we obtain $g \sim \frac{e^2}{h}\frac{E_{g0}}{\Gamma}\left(1 - e^{-\frac{\Gamma}{\Delta}}\right)$, recovering $g \sim \frac{e^2}{h}\frac{E_{g0}}{\Delta}$ for $\Gamma \ll \Delta$. As a result, because the number of non-hybridized carriers goes as Γ and their mobility goes as $1/\Gamma$, then it follows that the bulk conductivity, which is their product, will

have a constant value independent of level broadening.

In conclusion, in inverted InAs/GaSb quantum wells disorder has a singular effect, resulting in finite bulk conductivity even in the limit of relatively small level broadening of electron and hole levels, as revealed by theoretical work of Naveh and Laikhtman [40], and confirmed by our experiments. We emphasize here that the residual bulk conductivity is not a simple dirt effect, which can be removed by improving the cleanliness of the system, but a subtle yet profound consequence of dissipative quantum tunneling in realistic electron-hole systems. Nevertheless, this result suggests that bulk conductivity can be substantially reduced as the band structure is tuned towards the critical point, by decreasing the overlap between the bands E_{g0}, thus potentially opening a viable regime for observing a quantum spin Hall insulating phase. Experimentally, this can be readily achieved using narrower QWs. In the next section, we look in exactly such a parameter regime, where bulk conductivity is reduced, and by studying the length and width dependence of mini-gap conductance we find evidence in support of helical edge modes.

Chapter 4

Evidence for Helical Edge Channels and Topological Band Structure

4.1 Transport in narrower quantum wells - motivation and experimental preview

Motivated by the previous results, we have reduced the size of the quantum wells to 125 Å InAs/50 Å GaSb, resulting in a reduced bulk conductivity by a factor of 2-3, but with similar quantum well quality, i.e. comparable zero gate bias mobility. Furthermore, in order to increase the relative edge contribution to transport we study four-terminal structures, where edge conductance is doubled to $4e^2/h$ compared to six-terminal mesoscopic structures, as described in Chapter 2. With these modifications, the expected bulk contribution to electronic transport will be comparable to or smaller than the edge conductance, allowing us to investigate topological properties of the predicted helical edge channels. Note that unlike in mesoscopic structures where both edge and bulk conductance contributions are expected, in macroscopic samples only bulk conduction is measurable, because for macroscopic QSH samples, where $L \gg L_\phi$, the edge contribution vanishes (see Chapter 2). In this regard, macroscopic samples can be used as an important diagnostic of bulk mini-gap conduction, allowing us to separate the edge from the bulk contributions which coexist in mesoscopic

samples. This simple yet powerful idea has guided experiments presented in this chapter [45, 46].

4.2 Transport in narrower quantum wells - trade-offs and sample characterization

We first note that the reduced quantum well width has two competing effects on bulk conductivity in our structures. While the reduction of the quantum well width is necessary in order to decrease the value of E_{g0} and hence the bulk conduction in our samples, such an approach necessarily leads to lower sample moblities due to the increased interface scattering, with consequent larger level broadening, which generally increases bulk conductivity. However, in the case of InAs, this effect is significant only when the well widths are $\lesssim 100\,\text{Å}$, in which case the sample mobility drops off with power law dependence on the QW width [69]. In structures studied here, the electron mobility is still in the $10^4 - 10^5\,\text{cm}^2/\text{Vs}$ range, as can be seen in Fig. 4.1, and hence the bulk conductivity will decrease compared to the case of wider wells. Nevertheless, even in these structures, which are wider than $100\,\text{Å}$, interface scattering is the limiting factor in sample mobility, as can be concluded from the near linear dependence of mobility on the carrier density, and hence predominant short-range scattering. In any case, our narrower structures are still of very high quality, evidenced by the maximum mobility in excess of $2 \cdot 10^5\,\text{cm}^2/\text{Vs}$ at a carrier density of approximately $2.5{\cdot}10^{12}\text{cm}^{-2}$. The reduction in mobility at higher densities is due to the

populating of the second electron subband and consequent inter-subband scattering [79]. Two-subband electron occupation is clearly visible in SdH data shown in Fig. 4.2 b for the high density case. In this case, SdH can be described as a product of two cosine functions, each oscilatting with different frequency according to Eq. (3.6) and producing a signature beating pattern.

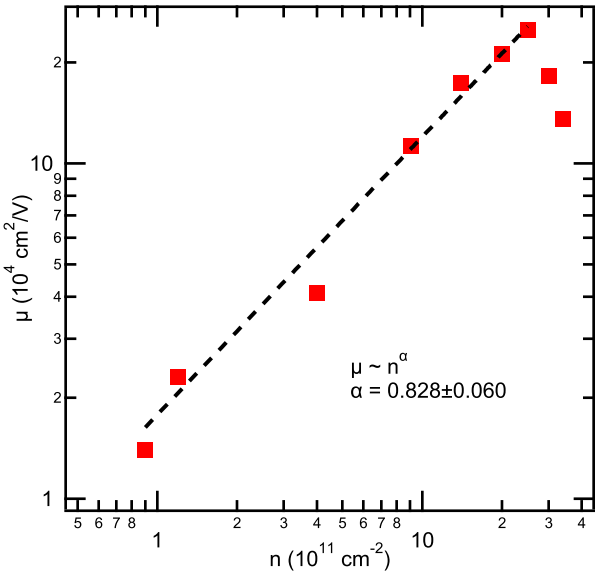

Figure 4.1 : Mobility versus density in 125 Å InAs/50 Å GaSb QW at $T = 300\,\mathrm{mK}$.

Furthermore, similar to the case of wider wells, in the narrower structures we can also tune the Fermi level through the hybridization gap, as demonstrated in Fig. 4.2 by plotting R_{xy} and R_{xx} versus B for front gate biases from $V_{front} = 6\,\mathrm{V}$ down to $-6\,\mathrm{V}$. At $V_{front} = 6\,\mathrm{V}$ (in red), R_{xy} varies linearly with B for small fields, while at higher fields quantum Hall plateaus develop, indicating single carrier electron type transport. As V_{front} is reduced to lower voltages, electron density is reduced and the slope of the R_{xy} trace increases, in agreement with Eq. (3.1) describing single car-

rier transport. However at $V_{front} = -4\,\mathrm{V}$(dark-blue), Hall resistance sharply bends downwards, suggesting two-carrier transport according to Eq. (3.4), and becomes negative at larger magnetic fields, indicating hole-dominated conduction. Furthermore, as V_{front} is further reduced to $-6\,\mathrm{V}$(violet), the slope of R_{xy} decreases, indicating a higher hole density. Fig. 4.2 is comparable to Fig. 3.6 presented in Chapter 3 for the case of wider wells; however in this case the bending of the Hall trace is much steeper and more abrupt, which is indicative of a lower electron density in the two-carrier regime, and hence lower on-resonance $n_{cross} = n \sim p$ density and reduced E_{g0}, as we expect for narrower wells. From the fits to the Hall trace in Fig. 4.2 with Eq. (3.4), for the case when $V_{front} = -4\,\mathrm{V}$(dark-blue) and the Fermi level is slightly below the hybridization gap, we obtain carrier densities as $n \sim 1.5{\cdot}10^{11}\mathrm{cm}^{-2}$ and $p \sim 3.6{\cdot}10^{11}\mathrm{cm}^{-2}$ indicating that on-resonance carrier density is roughly $n_{cross} \sim 2 \cdot 10^{11}\mathrm{cm}^{-2}$ and thus $E_{g0} = n_{cross}\frac{\pi\hbar^2}{m^*} \simeq 16\,\mathrm{meV}$, where m^* is the reduced mass. The latter number is also confirmed by data presented in Fig. 4.3 and theoretical calculations presented in Fig. 2.4. In comparison, this E_{g0} value is roughly two times smaller than in the case of wider wells discussed in Chapter 3. Having established that the overlap between the electron and hole bands is reduced in these narrower wells, we next look at the effect of the reduced E_{g0} on the bulk conduction in the hybridization gap. Here we analyze macroscopic samples, which, as argued earlier, exhibit only bulk transport and are thus good diagnostic of bulk conduction in our structures.

Fig. 4.3 shows longitudinal resistance R_{xx} (in red) vs. front gate bias V_{front} for a

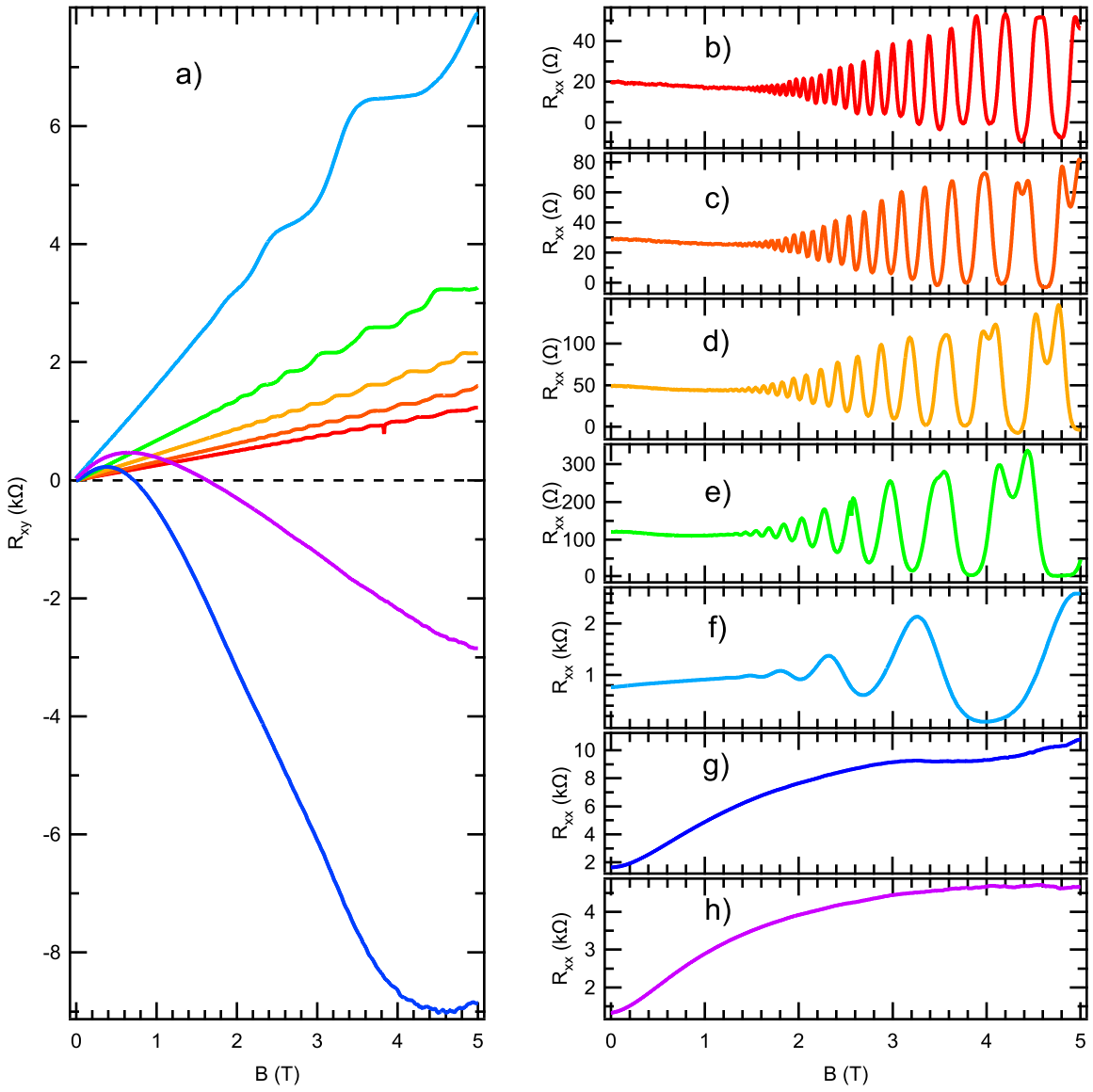

Figure 4.2 : Panel a) shows R_{xy} versus B for $V_{front} = 6\,\mathrm{V}$(red), $4\,\mathrm{V}$(orange), $2\,\mathrm{V}$(ocher), $0\,\mathrm{V}$(green), $-2\,\mathrm{V}$(light-blue), $-4\,\mathrm{V}$(dark blue), and $-6\,\mathrm{V}$(violet), while panels b-h show respective R_{xx} versus B traces for a $50\,\mu\mathrm{m} \times 100\,\mu\mathrm{m}$ device; $T = 300\,\mathrm{mK}$.

macroscopic Hall bar, with length $L = 100\,\mu\text{m}$ and geometric factor $\square = L/W = 2$, at $B = 0\,\text{T}$, $T = 300\,\text{mK}$. As V_{front} is swept from $0\,\text{V}$ to $-4\,\text{V}$, the Fermi energy E_F is pushed from the purely electron to the two-carrier hole-dominated regime. When $n \sim p$, a strong resistance peak of $R_{max} \sim 10.2\,\text{k}\Omega$ is observed, which for this macroscopic sample reflects only the bulk transport, with bulk gap conductivity of $g_{bulk} = \frac{\square}{Rmax} = 5.05e^2/h$.

The entry of the Fermi energy into the hybridization gap is also signaled by non-linearity in B/eR_{xy} (taken at $B = 1\,\text{T}$) shown in Fig. 4.3 in blue. The negative values of B/eR_{xy} indicate a hole-dominated regime although in a two-carrier regime direct correspondence to carrier density no longer exists as discussed in earlier chapters. Similarly, the size of the mini-gap can be determined from the relative position in V_{front} of the resistance dip, which corresponds to the van Hove singularity at the gap edge, and the resistance peak which corresponds to the middle of the gap $\triangle = 2\,(V_{peak} - V_{dip})\,\frac{\Delta n}{\Delta V}\frac{1}{DOS}$, where $\frac{\Delta n}{\Delta V} = 4.2 \cdot 10^{11}\text{cm}^{-2}/\text{V}$ is the rate of carrier density change with V_{front}, giving $\triangle \sim 4\,\text{meV}$. We note here in passing that this mini-gap value is slightly larger than the one reported for wider wells, presumably due to the "squeezing" of the electron-hole wavefunctions in narrower wells and larger overlap of the tails. Furthermore, from the minimum in B/eR_{xy} which corresponds to an anti-crossing density of $n_{cross} \sim 2 \cdot 10^{11}\,\text{cm}^{-2}$, we can estimate $E_{g0} = n_{cross}\frac{\pi\hbar^2}{m^*} \sim 16\,\text{meV}$, which is similar to the value obtained earlier. The expected bulk conductivity is then $g_{bulk} \sim \frac{e^2}{h}\frac{E_{g0}}{\Delta} \sim \frac{4e^2}{h}$, consistent with the observed value of $5.05e^2/h$ in Fig.

4.3. Besides validating the Naveh-Laikhtman theory of bulk conduction, these results clearly show that bulk conduction in our samples can be controlled and reduced so that edge conduction may become apparent, as we show in the next few sections [45, 46].

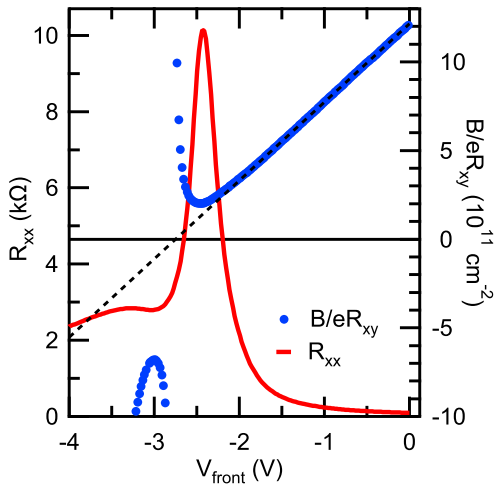

Figure 4.3 : Shows longitudinal resistance R_{xx} (in red) at $B = 0\,\mathrm{T}$ and B/eR_{xy} (in blue), taken at $B = 1\,\mathrm{T}$, vs. front gate bias V_{front} for $50\,\mu\mathrm{m} \times 100\,\mu\mathrm{m}$ device. As E_F is pushed into the hybridization gap R_{xx} exhibits a strong peak, concomitantly B/eR_{xy} becomes non-linear, signaling two-carrier transport and mini-gap entry [45].

4.3 Scaling evidence for the helical edge channels

In order to investigate possible edge transport in our samples, we compare the conduction in devices of various lengths, ranging from macroscopic down to mesocopic. As a result we reduce the length of devices from $L = 100\,\mu\mathrm{m}$, down to $10\,\mu\mathrm{m}$, $4\,\mu\mathrm{m}$, and $2\,\mu\mathrm{m}$, while adjusting the width to keep the constant geometric factor $\square = 2$, thus keeping the bulk contribution approximately the same in all devices. As the length

of the device is reduced form macroscopic to mesoscopic dimensions, the value of the resistance peaks decreases sharply as shown in Fig. 4.4, indicating the "activation" of edge transport at shorter length scales, in agreement with Eq. (2.12). Furthermore, noting that the edge contribution in the macroscopic $L = 100\,\mu\text{m}$ sample is negligible, the resistance peak of this device can be used to estimate the gap resistance of the bulk $R_{bulk} \sim 10.2\,\text{k}\Omega$. A parallel combination of R_{bulk} and the expected helical edge resistance of $h/4e^2$ gives a resistance value of $R_{bulk}||h/4e^2 \sim 3.95\,\text{k}\Omega$ (dashed black line in Fig. 4.4 a, which is just slightly above the measured valued of $R_{max} \sim 3.75\,\text{k}\Omega$ for the $L = 2\,\mu\text{m}$ device, in clear support of theoretically proposed helical edge channels.

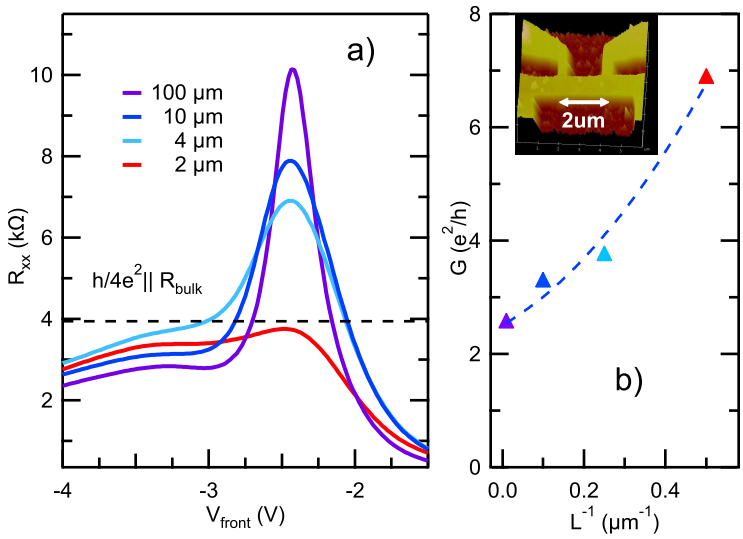

Figure 4.4 : Panel a) shows R_{xx} vs. V_{front} for devices with $L = 100\,\mu$m, $10\,\mu$m, $4\,\mu$m, and $2\,\mu$m (AFM image in inset) while W is varied to give a constant geometric factor $\square = L/W = 2$; $B = 0\,\text{T}$, $T = 300\,\text{mK}$. Resistance peaks decrease for shorter devices and approach the limit $R_{bulk}||h/4e^2$ (dashed line) for $2\,\mu$m device. Panel b) shows gap conductance G vs. L^{-1} and is fitted with Eq. (2.12) (dashed) giving coherence length $L_\phi = 2.07 \pm 0.25\,\mu$m. Conductance difference between mesoscopic and macroscopic device is $\sim 4e^2/h$ suggestive of helical edge transport [45].

Similarly, the gap conductance G plotted versus inverse device length $1/L$ in Fig. 4.4b, can be fitted reasonably well with Eq. (2.12), obtaining a phase coherence length of $L_\phi = (2.07 \pm 0.25)\ \mu$m. This is in agreement with the rough estimates of phase coherence length from universal conductance fluctuations in the previous chapter, as well as with values inferred from measurements on superconducting junctions [80]. We emphasize here that the difference in conductance between mesoscopic structures, which show both bulk and edge contributions, and macroscopic structures with bulk transport only, is just slightly above $4e^2/h$ - exactly the value which we expect for helical edge channels. Note that the bulk conductivity also scales with the length, however this logarithmic correction [81] to bulk conductance can be estimated as $\Delta G = \frac{e^2}{\square \pi h} \cdot Ln(\frac{100\,\mu\text{m}}{2\,\mu\text{m}}) \sim 0.6\frac{e^2}{h}$ and thus accounts for only a fraction of the total observed difference in conductance between the mesoscopic and macroscopic samples.

Additional evidence for edge modes is found in the width dependence of the gap resistance in mesoscopic samples. Fig. 4.5 shows the resistance peaks of four devices of equal length $L = 2\,\mu$m, but with different widths, $W = 0.5\,\mu$m, $1\,\mu$m, $1.5\,\mu$m, and $2\,\mu$m. In this case, the resistance peak decreases as the device width is increased, as expected for bulk transport; however, gap conductance, which shows linear dependence on W, has a nonzero intercept from the linear fit, which is in sharp contrast to exclusive bulk conduction. In fact, the intercept value of $G_{edge} = (4.08 \pm 0.69)\,\frac{e^2}{h}$, strongly suggests the existence of helical edge conduction channels. As an important check, the slope of the same fit gives a bulk conductivity of $g_{bulk} = (5.46 \pm 1.01)\,\frac{e^2}{h}$

which is consistent with previously determined values. In conclusion, both the length and width dependence of the gap conductance consistently confirm the existence of helical edge channels in inverted InAs/GaSb quantum wells.

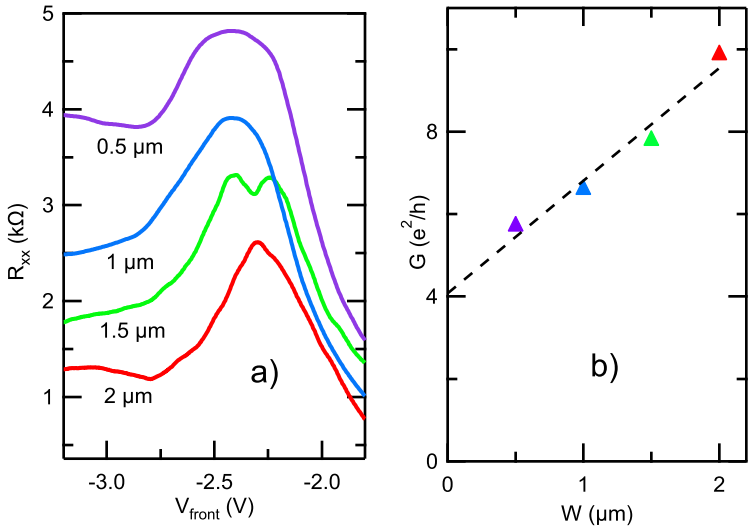

Figure 4.5 : Panel a) shows R_{xx} vs. V_{front} for devices with $W = 0.5\,\mu$m, $1\,\mu$m, $1.5\,\mu$m, and $2\,\mu$m; $L = 2\,\mu$m. Resistance peaks decrease with increasing W. Gap conductance G vs. W in panel b) shows a linear relationship. The intercept of the linear fit is $G_{edge} = (4.08 \pm 0.69)\,\frac{e^2}{h}$, as expected for helical edge transport, while slope of the fit gives bulk conductivity $g_{bulk} = (5.46 \pm 1.01)\,\frac{e^2}{h}$, consistent with data in Fig. 4.4 [45].

4.4 Resilience of edge transport to the presence of bulk states and edge-bulk decoupling

Data presented in the previous section suggests that edge transport shows a remarkable degree of resilience to the presence of bulk states. This issue is further investigated in experiments where the anticrossing point in the band structure and therefore the bulk conductivity is further tuned via back gate bias. In the first experiment we

tune the anticrossing point k_{cross} to lower values by applying more negative V_{back}, thereby suppressing g_{bulk}.

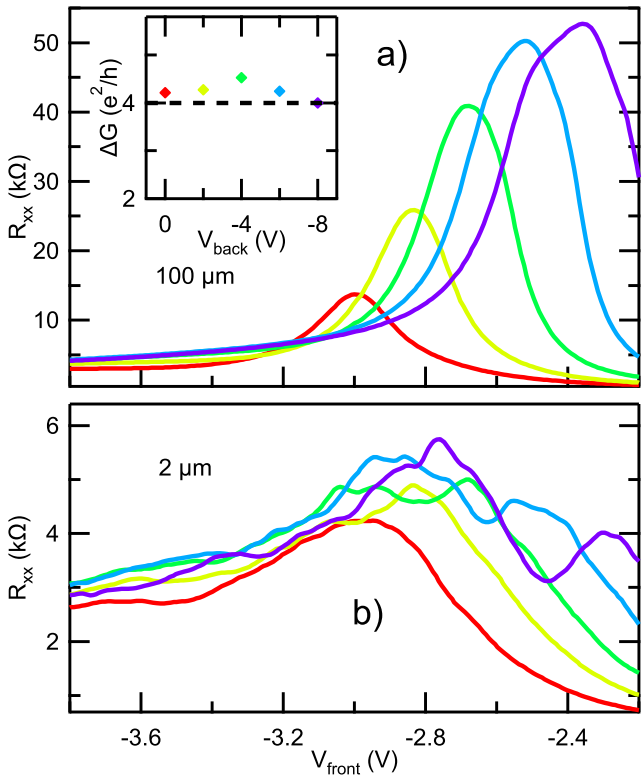

Figure 4.6 : Shows R_{xx} vs V_{front} for devices with $L = 100\,\mu$m in a) and $L = 2\,\mu$m in b), with $\square = 2$ in both cases, with V_{back} varied in 2 V steps from 0 V to -8 V; $B = 0$ T, $T = 20$ mK. As V_{back} is tuned to more negative values, the mini-gap moves to smaller wavevectors and the resistance peaks increase. Inset shows difference in conductance between mesoscopic and macroscopic sample, i.e. between $2\,\mu$m and $100\,\mu$m sample, $\Delta G = G_{2\,\mu\mathrm{m}} - G_{100\,\mu\mathrm{m}}$ versus vs V_{back}, which stays around $\Delta G \sim 4e^2/h$ for all values of V_{back}. These suggests that edge and bulk transport are seemingly decoupled. Note that in these structures $g_{bulk} \lesssim 5e^2/h$ [45].

Fig. 4.6 shows R_{xx} vs V_{front} with V_{back} varied in 2 V steps from 0 V to -8 V for devices of $L = 100\,\mu$m in a) and $L = 2\,\mu$m in b), with $\square = 2$ in both cases. As V_{back} is tuned to more negative values, the overlap between the bands E_{g0} is reduced,

and the resistance peak of the $L = 100\,\mu\text{m}$ sample increases from $R_{max} \sim 10\,\text{k}\Omega$ at $V_{back} = 0\,\text{V}$, to $R_{max} \sim 50\,\text{k}\Omega$ at $V_{back} = -8\,\text{V}$. On the other hand, the resistance peak of the mesoscopic sample increases only slightly, from $R_{max} \sim 4\,\text{k}\Omega$ at $V_{back} = 0\,\text{V}$, to $R_{max} \sim 6\,\text{k}\Omega$ at $V_{back} = -8\,\text{V}$. In fact, the conductance difference between mesoscopic and macroscopic samples, $\Delta G = G_{2\,\mu\text{m}} - G_{100\,\mu\text{m}}$ stays around $\sim 4e^2/h$ for all values of V_{back}, as shown in the inset of Fig. 4.6, giving further evidence in support of helical edge channels. We mention here in passing that the resistance peak shifts towards more positive V_{front} as V_{back} is made more negative, which is due to the fact that the resistance peak occurs at the charge neutral point, and hence $\Delta Q = 0$. As a result, from simple capacitance considerations we have $\Delta V_{back} \cdot C_{back} + \Delta V_{front} \cdot C_{front} = 0$, where C_{back} and C_{front} are capacitances of front and back gates. In fact, the ratio of shifts in gate biases corresponds directly to the ratio of respective capacitances.

Furthermore, note that for the case of $V_{back} = -8\,\text{V}$, the bulk resistance value is an order of magnitude larger than the corresponding edge resistance, as is the case in another model QSH system of HgTe/CdTe quantum wells [32, 58]. Of course, this comes with the added benefits of band structure tunability, selective etchability, and low Schottky barrier for a great number of metals and superconductors. This proves the presumption that bulk conductivity in our samples can be significantly suppressed, making InAs/GaSb a preferred system for studying many of the interesting QSH phenomena, such as proposed Majorana bound states and topological phase transitions within a variety of experimental techniques, ranging from transport to

scanning probe measurements.

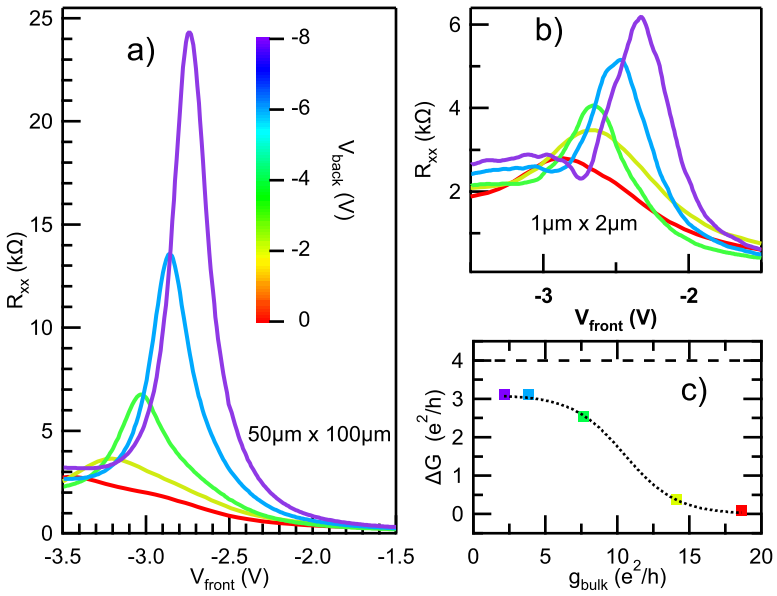

Figure 4.7 : Shows R_{xx} vs V_{front} for bias cooled devices with $L = 100\,\mu$m in a) and $L = 2\,\mu$m in b), with $\square = 2$ in both cases, with V_{back} varied in 2 V steps from 0 V to -8 V. Panel c) shows ΔG versus bulk conductivity g_{bulk}. Edge conduction is apparent for $g_{bulk} \lesssim 10e^2/h$ [45].

Before we proceed, a word of caution is here in order, for the data presented in Fig. 4.6 may suggest that edge conduction is completely independent of the gap bulk conductivity, g_{bulk}. However, this is valid only in the regime of low g_{bulk}. Note that in Fig. 4.6 the gap bulk conductivity is varied from about $g_{bulk} \sim 5e^2/h$ at $V_{back} = 0$ V, to $g_{bulk} \sim 0.5e^2/h$ at $V_{back} = -8$ V. Using the bias cooling technique, it is possible to shift the starting point deeper into the inverted regime, i.e. a larger E_{g0} can be obtained, so that at $V_{back} = 0$ V, $g_{bulk} \sim 19e^2/h$, while at $V_{back} = -8$ V, $g_{bulk} \sim e^2/h$, as shown in Fig. 4.7. In this case, the edge conductance, i.e. $\Delta G = G_{2\,\mu\mathrm{m}} - G_{100\,\mu\mathrm{m}}$, goes from $\Delta G \sim 0$ for a large bulk conductivity of $g_{bulk} \sim 19e^2/h$ to about $\Delta G \sim 3e^2/h$ as

the bulk conductivity is reduced to $g_{bulk} \lesssim 5e^2/h$, as shown in Fig. 4.7. In fact, the cut-off bulk conductivity at which edge conduction "activates" can be estimated to be $g_{bulk} \sim 10e^2/h$. In consequence, bulk conductivity clearly suppresses edge transport but only when it is sufficiently large. In the case of low bulk conductivity, edge and bulk transport are seemingly decoupled.

The apparent resilience of edge conduction to bulk transport, at least for smaller values of bulk conductivity, which is seen in Figs. 4.6 and 4.7, is quite surprising, considering that a conductive bulk would allow edge electrons to tunnel from one side of a sample to another, resulting in inter-edge scattering and a reduced edge conductance [42, 43, 44]. In a recent theoretical study of QSH edges in a quantum point contact geometry where tunneling between edge modes on opposite sides is enabled by reducing the device width, it has been found that the decrease in two-terminal helical edge conductance is roughly proportional to $\propto T sin^2\vartheta$, where ϑ is the angle between spin direction and growth axis and T is the tunneling probability between the edges [43]. Thus, even for a large tunneling probability, edge conductance will not diminish if the spins are normal to the quantum well plane, which is the case for weak Rashba spin-orbital interaction. Note that due to the low Fermi velocity of edge states $v = \frac{1}{\hbar}\frac{\partial E}{\partial k} \sim \frac{1}{\hbar} \cdot \frac{\Delta}{2k_{cross}} \sim 3 \cdot 10^4\,\mathrm{m/s}$, relativistic effects of Rashba spin-orbital interaction might be small, and electron spins may very well be aligned along the growth axis, reducing inter-edge tunneling due to the Pauli exclusion [44].

Furthermore, the tunneling probability T between the opposite-side edges may

be significantly reduced by a large Fermi wavevector mismatch. Note that bulk gap states are inherited from a non-hybridized band structure and generally have Fermi wavevector equal to $k_{cross} \gg 0$ while edge modes, for E_F situated in the middle of the gap, have $k_{edge} \sim 0$. Thus, for larger k_{cross} edge modes will be totally reflected from bulk states. In fact, the tunneling probability for the edge electrons will be proportional to the edge-bulk transmission probability, which scales as k_{edge}/k_{cross}, as well as the bulk transmission, which scales as bulk conductivity and hence is proportional to the overlap between the subbands E_{go} and thus varies as$\propto k_{cross}^2$. It follows then that the overall inter-edge tunneling probability will decrease as k_{cross} is reduced. This picture qualitatively agrees with the data presented in Fig. 4.7 where edge conduction activates for smaller bulk conductivity, i.e. in the regime of reduced E_{g0} and k_{cross}, and thus closer to the critical point. Nevertheless, the full quantum theoretical treatment of the problem, which would include dissipation in the tunneling between the wells, similar to Ref. [40], is expected to reveal in more detail the stark resilience of edge transport to the conductive bulk. In the next section, we look into a similar resilience of edge transport to weak magnetic fields.

4.5 Weak field behavior

Next we turn to the magnetic field dependence of gap transport in mesoscopic and macroscopic samples. Surprisingly, resistance peaks of mesoscopic samples show only weak dependence on in-plane and perpendicular magnetic fields as shown in Fig. 4.8,

while macroscopic samples show much stronger dependence. At a first glance, this appears to be in contrast to the strong field dependence reported for HgTe/CdTe quantum wells and the notion of time reversal breaking, which spoils the perfect destructive interference of backscattering paths and leads to the fast decay of edge conductance in a perpendicular field.

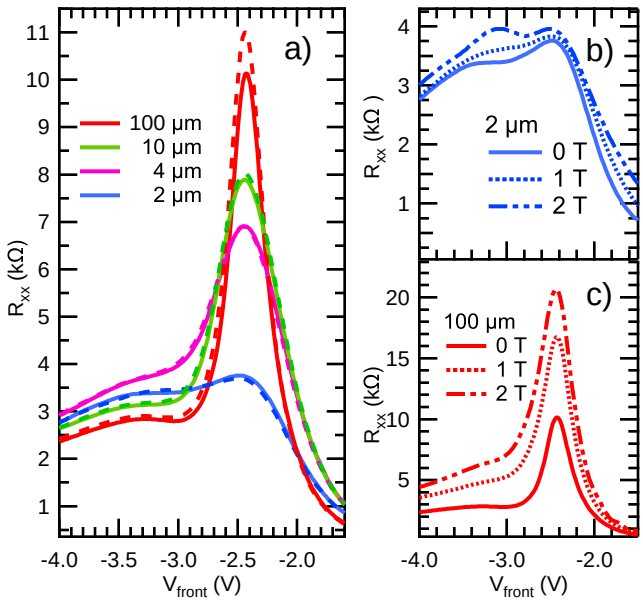

Figure 4.8 : Panel a) shows R_{xx} vs. V_{front} at in-plane field $B_{||} = 0\,\mathrm{T}$ (full line) and $B_{||} = 1\,\mathrm{T}$ (dashed line) for $L = 100\,\mu$m, $10\,\mu$m, $4\,\mu$m, and $2\,\mu$m, indicating weak field dependence of gap resistance; $T = 300\,$mK. Panel b) shows R_{xx} vs. V_{front} at perpendicular fields of $B_{perpen.} = 0\,\mathrm{T}$, $1\,\mathrm{T}$, and $2\,\mathrm{T}$ for $L = 2\,\mu$m, and in panel c) for $L = 100\,\mu$m [45].

However, we note that even in HgTe/CdTe strong magnetic field dependence has never been observed in the smallest micron-size samples, but in the 20 µm long samples [58]. In fact, it has been shown theoretically by Maciejko et al [82], using the full quantum approach of the Keldysh formalism, that the magnetic field decay of edge modes depends sensitively on the disorder strength, with pronounced cusp-like

features of the conductance in a magnetic field occurring only when the disorder strength is larger than the size of the gap. The interpretation of this result was that by providing the states in the bulk by disorder, which is larger then the size of the gap, edge electrons can diffuse into the bulk enclosing larger amounts of flux whose accumulation destroys destructive interference of backscattering paths, resulting in a linear decay of conductance with B. Thus, surprisingly enough, and in contrast to the simple notion of symmetry breaking by applying a magnetic field, bulk states are necessary for edge conduction decay in a magnetic field. In the case of HgTe/CdTe, bulk states were provided by inhomogenous gating, which is more pronounced for longer devices.

Thus, it would naively seem that edge modes in InAs/GaSb should have very strong field dependence due to apparent bulk conduction. However, bulk-edge wave-vector mismatch reduces this possibility in InAs/GaSb, at least in shorter devices. Note that unlike in HgTe/CdTe where the gap opens at $k = 0$, in InAs/GaSb the mini-gap opens at k values generally much larger than zero, and hence, in the middle of the gap, bulk states will necessarily have Fermi wave-vectors significantly larger than the edge. Consequently, due to this decoupling of edge from bulk, the magnetic field dependence of edge modes is expected to be weak. On the other hand, the decay of bulk conductivity with magnetic field may not necessarily be weak due to the localization of the non-hybridized carriers which contribute to nonzero bulk conductivity in the first place. However, this localization is more pronounced for

longer samples, where disorder is naturally stronger. In addition, we note that edge-bulk decoupling is valid only in the limit of smaller disorder, while for larger disorder edge conductance is expected to decay in the magnetic field, similar to the HgTe case. In any case, longer samples are expected to show stronger magnetic field dependence due to both the bulk states' localization and edge supression effects, as experimentally observed in Fig. 4.8 c.

In fact, a clear zero-field conductance enhancement in the hybridization gap is observed in Fig. 4.9 in a $50\,\mu\text{m} \times 100\,\mu\text{m}$ device, where we plot magnetoresistance traces for various front gate biases. As the hybridization gap is approached, small spikes in conductivity at zero magnetic field are observed. Because these features in magnetoconductance are absent for front gate biases away from the mini-gap regime, they presumably stem from the small edge contribution to transport, which is quickly supressed in small magnetic field, similar to the case of long HgTe/CdTe devices. At any rate, magnetic field dependence in both InAs/GaSb and HgTe/CdTe is far more similar than an initial assessment of data presented in Fig. 4.8 might suggest, i.e. in both cases field dependence is weak for mesoscopic devices, while in longer devices clear zero-field conductance enhancement is observed. We note here that weak antilocalization features that are observed in longer devices in both InAs/GaSb and HgTe/CdTe might be a bulk effect after all, enhanced by gating due to Rashba spin-orbital interactions. In fact, recent theoretical work [62] argues that for suitably smooth confinement potential and low disorder, QSH gapless edge states are

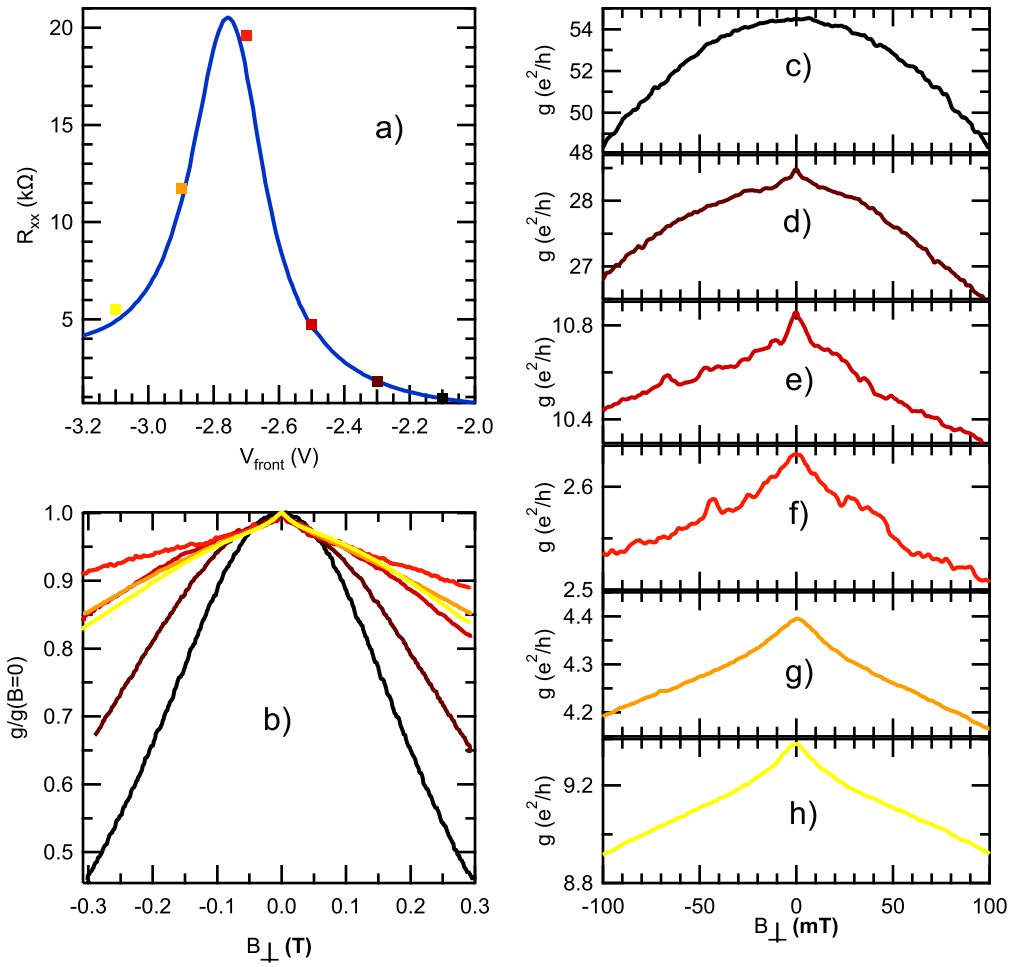

Figure 4.9 : Panel a) shows R_{xx} (in blue) at $B = 0\,\mathrm{T}$ for $50\,\mu\mathrm{m} \times 100\,\mu\mathrm{m}$ device; $T = 20\,\mathrm{mK}$. Colored markers represent V_{front} biases at which we take magnetoresistance traces, and are shown in normalized form in panel b), while panels c) through h) show unscaled conductivity traces versus B. Note clear conductivity enhancement at zero field.

protected by the band topology alone, rather than any symmetries, making QSH inherently more robust to magnetic fields than originally envisioned. Next, we look into transport at high magnetic fields, where we observe dramatic re-entrant quantum Hall behavior - a signature mark of topologically distinct band structure, which validates the topological origin of helical edge modes at zero magnetic field.

4.6 Topological band structure and re-entrant quantum Hall behavior

Re-entrant quantum Hall behavior has been previously observed in HgTe/CdTe QWs, where the system switches from an insulating to an integer quantum Hall regime at $\nu = 1$ and back to insulating at higher fields [32]. This has been taken as direct evidence of a topologically non-trivial gap. Similarly, such metal-insulator oscillations have also been previously observed in InAs/GaSb QWs [83, 84, 85, 86] and also by us in the context of proposed topological phases for the InAs/GaSb system and in a different parameter regime. The origin of re-entrant behavior in InAs/GaSb can be traced back to its non-monotonic band structure. Under a perpendicular magnetic field the continuous density of states separates into series of discrete Landau levels whose dispersion in a magnetic field can be obtained from zero-field simply by transforming $k \rightarrow \sqrt{(2\nu - 1) \cdot e \cdot B/\hbar}$ [35], where ν is the Landau level index. In consequence, the non-monotonic zero-field spectrum will give a similarly non-monotonic Landau level spectrum. At field values which can be related to anti-crossing wave-vector and

band extrema, the Landau level spectrum is gapped and the system switches to an insulating regime. Further away from band extrema, the system exhibits a normal quantum Hall behavior. Fig. 4.10 shows the first twenty Landau levels of electron and heavy hole subbands in 125 Å InAs/50 Å GaSb QWs calculated within an 8-band $k \cdot p$ approach [56, 77]. Note great number of anti-crossing points in the spectrum, which ultimately lead to re-entrant quantum Hall behavior.

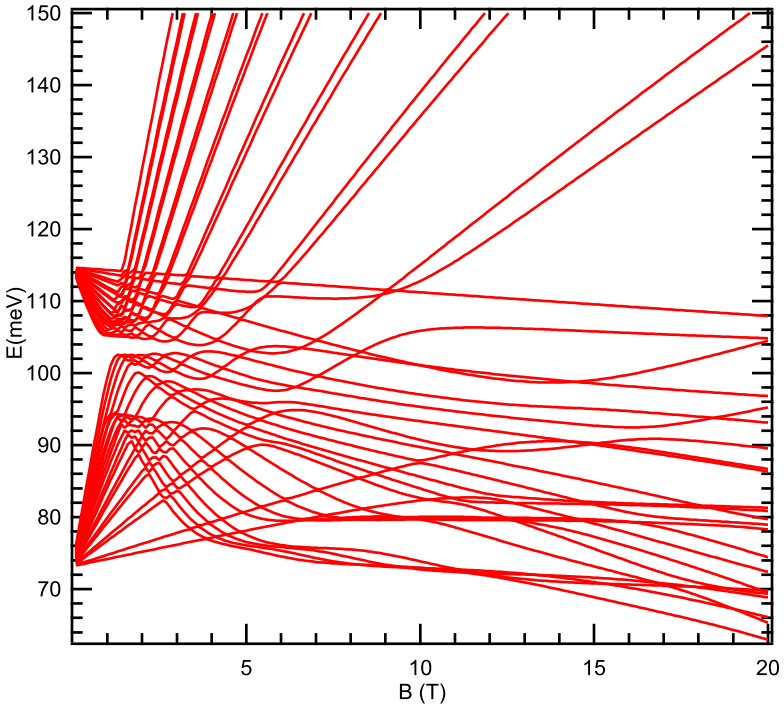

Figure 4.10 : Landau level spectrum in 125 Å InAs/50 Å GaSb QWs calculated within 8-band Kane approach, showing first twenty Landau levels of electron and heavy-hole subbands [56].

As the magnetic field is increased, the separation between the Landau levels is increased, causing their depopulation. In turn, the Fermi level will oscillate with an amplitude which is inversely proportional to the Landau level index. Assuming

a single carrier regime, the magnetic field at which the Fermi energy drops from $(\nu+1)$ to ν Landau level is $B_{\nu+1\to\nu} = \frac{n\cdot h}{\nu\cdot e}$, where n is the carrier density at zero field. The associated change in Fermi energy is $\Delta E_F = E_{LL}\left(\begin{array}{cc} \nu+1, & B_{\nu+1\to\nu} \end{array}\right) - E_{LL}\left(\begin{array}{cc} \nu, & B_{\nu+1\to\nu} \end{array}\right) \sim \hbar\frac{e\cdot B_{\nu+1\to\nu}}{m_e} = 2\frac{n}{\nu}\cdot\frac{\pi\hbar^2}{m_e}$, which for our system parameters can be in the tens of meVs. Thus, even for a purely electronic system, with the Fermi energy above the hybridization gap, the oscillations of the Fermi level due to Landau level depopulation can put the Fermi energy below and into the mini-gap resulting in a re-entrant quantum Hall behavior.

Fig. 4.11 a) shows R_{xx} (in red) and R_{xy} (in blue) in a macroscopic $50\,\mu$m $\times$ $100\,\mu$m Hall bar sample with $n = 9.5\cdot 10^{11}\mathrm{cm}^{-2}$, $T = 20\,$mK, and $B = 0\,$T to $10\,$T. Pronounced Shubnikov-de Haas oscillations are observed in R_{xx} starting at about $1.5\,$T, as well as clear integer quantum Hall (IQH) plateaus in R_{xy} starting at about $2\,$T. At $B \sim 4.2\,$T both R_{xx} and R_{xy} increase drastically as the system exits the $\nu = 10$ IQH state and turns towards the insulating regime. The system returns from the insulating regime at $B \sim 4.7\,$T, entering the $\nu = 8$ state with $R_{xx} \sim 0$. Similarly, such a re-entrant quantum Hall behavior is also observed at $B \sim 5.6\,$T, albeit with a slightly weaker insulating regime, and again at $B > 7\,$T for which the system turns strongly insulating. The fields at which the system turns insulating form a regular ratio of $2:3:4$ and can be related empirically to the anti-crossing density (i.e. k_{cross} in zero-field spectrum) as $B_{cross} \sim \frac{2n_{cross}\cdot h}{i\cdot e}$ where i is an integer, and the anti-crossing density has been estimated to be $n_{cross} \sim 2\cdot 10^{11}\mathrm{cm}^{-2}$ via density measurements.

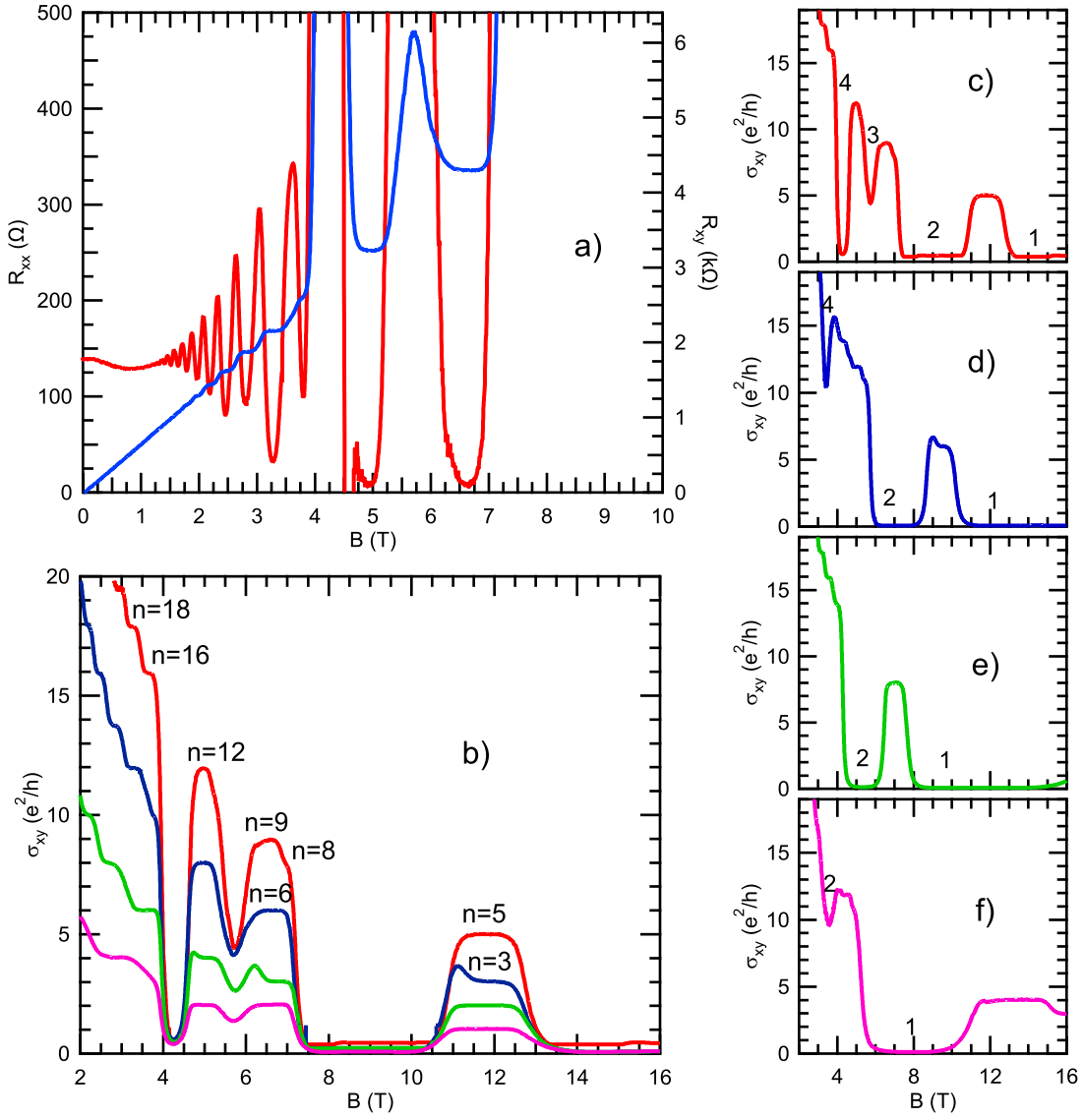

Figure 4.11 : Panel a) shows R_{xx} (in red) and R_{xy} (in blue) versus magnetic field B in a macroscopic $50\,\mu\text{m} \times 100\,\mu\text{m}$ Hall bar, $T = 20\,\text{mK}$. System exhibits re-entrant quantum Hall behavior at $B = 4.2\,\text{T}$, $5.6\,\text{T}$, and $7.5\,\text{T}$. Panel b) shows Hall conductivity σ_{xy} versus B, for $V_{back} = 0\,\text{V}$, and $V_{front} = 0\,\text{V}$, $-1\,\text{V}$, $-2\,\text{V}$, $-2.5\,\text{V}$. Clear oscillations between IQH and insulating regimes are observed at similar fields for all values of V_{front}. Panels c-f show σ_{xy} versus B, for $V_{front} = 0\,\text{V}$, and $V_{back} = 0\,\text{V}$, $-2\,\text{V}$, $-4\,\text{V}$, $-6\,\text{V}$. Insulating regions shift to lower B as the system is tuned towards normal regime with more negative V_{back}.

It is more illustrative to look at the Hall conductivity σ_{xy} shown in Fig. 4.11 b), which shows clear oscillations from quantum Hall plateaus to insulating behavior as B is varied from 0 T to 16 T. We also vary V_{front} changing the electron density from $n = 13 \cdot 10^{11}\text{cm}^{-2}$ down to $n = 2.8 \cdot 10^{11}\text{cm}^{-2}$, with the hole well empty. Nevertheless, in all cases, insulating regions happen at the same B, which suggests that with the front gate bias only the Fermi level is changed, i.e. there is no change in k_{cross} and E_{g0}. On the other hand, by varying V_{back} towards more negative values, insulating regions shift to lower fields as shown in Fig. 4.11 c)-f), indicating a reduced k_{cross} and a smaller overlap between the $E1$ and $H1$ subbands. Thus, by applying a back-gate bias, the band structure can be continuously tuned. We note here that the independence of insulating regions on the front gate bias could also be due to the fact that contact arms actually become insulating versus the active region of the Hall bar. In this case, the back gate bias can still tune the carrier density and the band structure, in agreement with what we observe. In conclusion, at field values which correspond to band extrema, the Landau level spectrum of inverted InAs/GaSb is gapped and the system switches to the insulating regime. Further away from band extrema, the system exhibits normal quantum Hall behavior with clear plateaus in R_{xy}. Such re-entrant quantum Hall behavior is a clear signature of topologically distinct band structure and validates the existence of helical edge modes at zero fields.

4.7 Tuning InAs/GaSb quantum wells into "bilayer graphene"

In the previous portions of this thesis we have demonstrated significant tunability of the InAs/GaSb system via electrical fields, changing the overlap between the electron and hole subbands from several meVs to tens of meVs, and similarly changing the bulk resistance over two orders in magnitude; however, a transition from inverted to normal band structure, i.e. from red to blue regions in the phase diagram in Fig. 2.9 has not been demonstrated. This transition, however, is important for several reasons. First, it would make InAs/GaSb the only known system in nature whose band structure can be tuned from topologically non-trivial to topologically trivial via modest electrical fields, giving unique insight into the nature of such a topological quantum phase transition. Furthermore, such a transition may be important from a technological perspective because it would demonstrate a novel type of switch, which is dissipationless in its on state and highly resistive in its off state [8]. The practical utility of such a device would be limited by its low temperature operation requirement, which in principle could be extended to room temperatures. Finally, exactly at the critical point where $E1 = H1$, the Hamiltonian given in Eq. (2.6) suggests that this system behaves as a massive Dirac or chiral fermion system, in analogy to bilayer graphene but without degeneracies [8]. Such a system has been shown to exhibit non-trivial quantum Hall effect, in zeroth filling factor due to the 2π Berry phase, which is accumulated along cyclotron trajectories [87, 88]. Thus, besides massless Dirac fermions at the sample edge in the inverted regime, this system

also hosts massive Dirac fermions at the critical point where the band structure changes from inverted to normal. We note here in passing that when contacted with superconducting electrodes, InAs/GaSb QWs in the critical regime may also exhibit the recently proposed topological superconductivity, which hosts Majorana fermion bound states. Unlike bilayer graphene where Majorana bound states are not possible due to spin and valley degeneracies, InAs/GaSb does not have valley degeneracy, while spin degeneracy is lifted due to inversion asymmetries [8], allowing for the possibility of non-degenerate zero-energy modes. Note that in this case the zero-field spin splitting in our structures should be further increased to leave one Dirac point at the Fermi level and hence to obtain unpaired Majoranas, which can be easily done by bringing the back-gate closer to the InAs/GaSb quantum wells.

Here we tune the band structure from inverted towards normal regime via the front and back gate bias, as already shown in this thesis, and use transport under an in-plane magnetic field to gauge the actual regime of the system. Fig. 4.12 shows a sketch of band dispersions in inverted and normal regimes. Applying an in-plane magnetic field shifts electron and hole bands in opposite directions in k-space, resulting in a relative shift of the band dispersions: $\Delta k_{||} \approx \frac{eB_{||} \triangle z}{\hbar}$, where $\triangle z$ is the relative separation between electron and hole two-dimensional layers [36, 41]. In the inverted regime, the DOS will be markedly modified in the hybridization gap, resulting in a gap opening at different energies for positive and negative momentum values, and hence nonzero DOS across the hybridization regime. As a result, under

an in-plane magnetic field, resistance in the mini-gap will be significantly reduced. On the other hand, in the normal regime, the in-plane magnetic field does not affect the DOS in the gap, and the gap resistance will be unchanged.

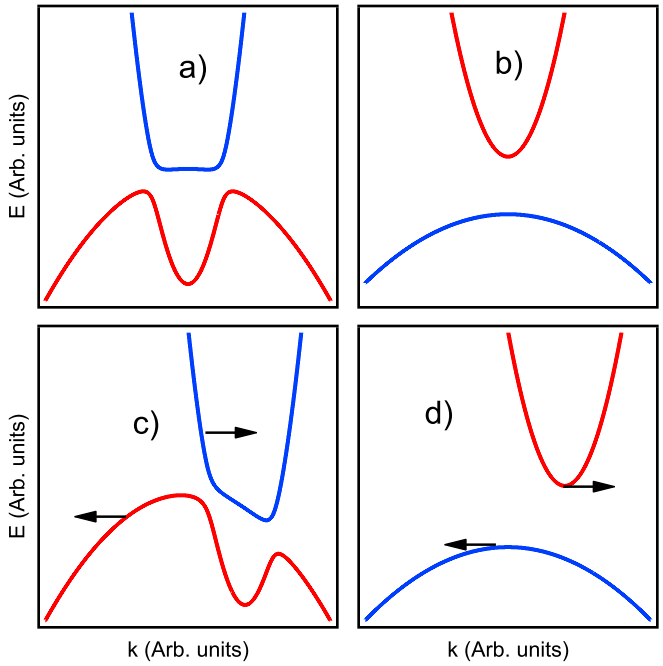

Figure 4.12 : Shows a sketch of band dispersions for inverted regime in a) and normal regime in b) at zero field. Applying in-plane magnetic field shifts E1 and H1 bands in opposite direction, as shown in figured c) and d) for the two regimes. In the case of inverted regime, transport will be markedly modified in the hybridization regime under in-plane magnetic field, and unaffected in the normal regime.

In Fig. 4.13 we show R_{xx} versus V_{front} at in-plane magnetic fields of 0 T (red), 5 T (green), 10 T (pink), and 15 T (blue), while the back gate bias V_{back} is varied from 8 V to -8 V. At $V_{back} = 8$ V, the system is clearly in the inverted regime with significant reduction of resistance peaks with the in-plane magnetic field. On the other hand, for $V_{back} = -8$ V resistance peaks are practically unaffected by the in-plane magnetic

fields of up to 15 T, which is sufficient to shift the band dispersions by as much as $\sim 2 \cdot 10^6\,\mathrm{cm}^{-1}$, indicating normal or close to the normal regime.

Further insight into transport properties at highly negative back gate biases and the regime where the band structure approaches the crtical point, can be inferred from regular magnetotransport in perpendicular magnetic fields. Here it is useful to schematically compare two distinct quantum Hall effects that are relevant to our system: a conventional one describing massive fermions in regular semiconductors, and an unconventional one describing massive Dirac or chiral fermions, such as found in bilayer graphene [89], and shown in Fig. 4.14 a) and b), respectively [87]. In the case of conventional QHE, the Landau level spectrum is given by $E_\nu = \left(\nu + \frac{1}{2}\right)\hbar\omega_c$, where ω_c is cyclotron frequency, while for chiral fermions the Berry phase accumulation of 2π leads to $E_\nu = \pm\hbar\omega_c\sqrt{\nu\,(\nu-1)}$ [88]. As a result, for chiral fermions, $\nu = 0$ and $\nu = 1$ are degenerate zero-energy states, unlike in conventional quantum Hall systems, where no zero-energy states are possible. Now, the carrier density per single Landau level is given as eB/h, and thus the number of occupied Landau levels can be tuned by either changing the carrier density or the magnetic field. Only the Landau levels that are completely filled will give a conductance contribution of e^2/h to the Hall conductance. In consequence, reducing the carrier density in a constant magnetic field will lower the number of filled Landau levels, and hence the Hall conductance will change in a step-wise fashion as sketched in Fig. 4.14. This is valid for all quantum Hall systems, with the notable difference between chiral fermions and ordinary fermions being the

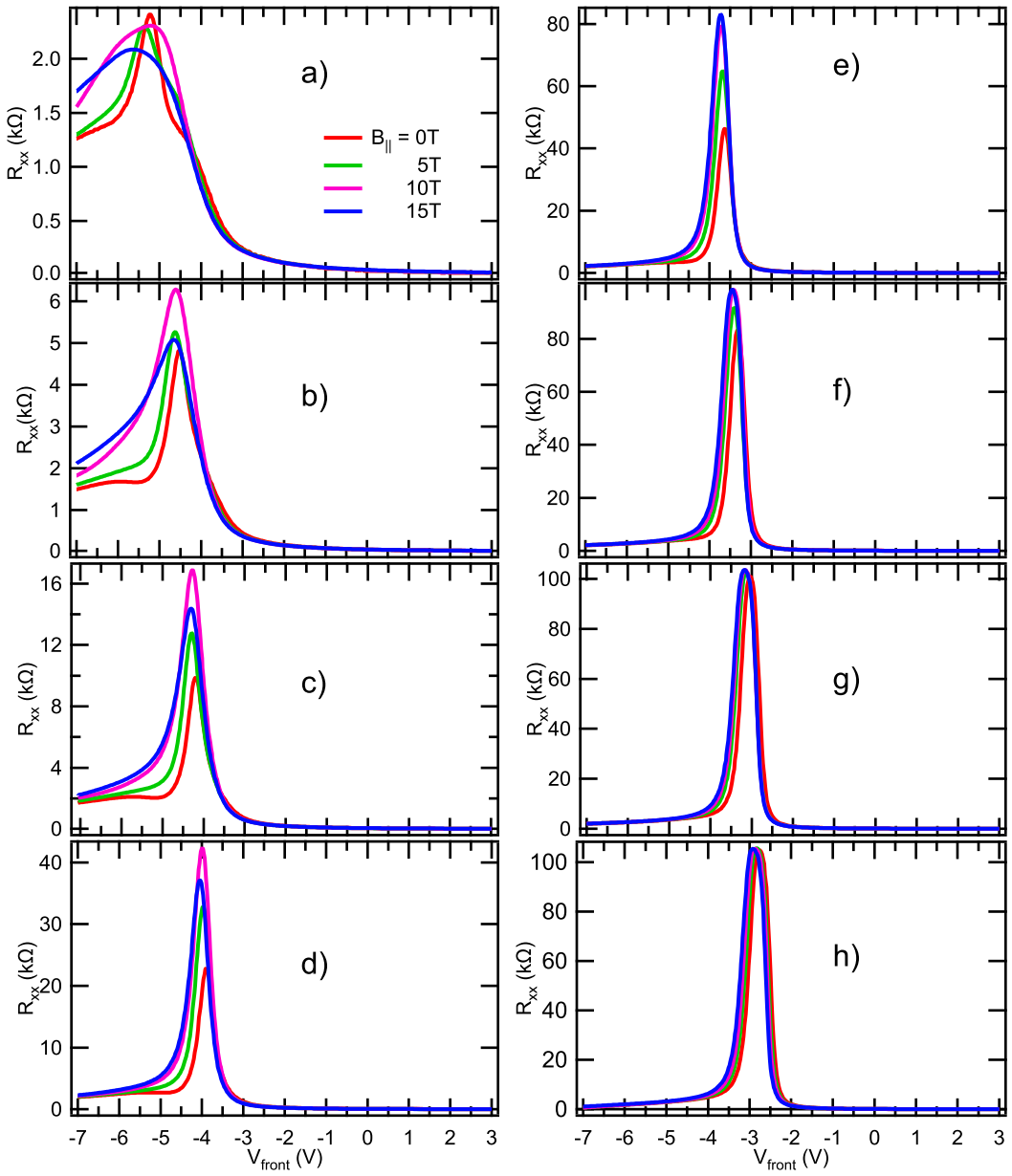

Figure 4.13 : Panels a-h show R_{xx} versus V_{front} at in-plane magnetic fields of 0 T (red), 5 T (green), 10 T (pink), and 15 T (blue) for back gate biases V_{back} = 8 V, 4 V, 2 V, 0 V, −2 V, −4 V, −6 V, and −8 V respectively. As the back gate bias is tuned more negative the overlap between H1 and E1 bands is reduced and system switches from inverted structure in a) (significant in-plane field effect) to non-inverted structure in h) (insignificant in-plane field effect).

absence of $\nu = 0$ Hall conductance plateau. For chiral fermions, due to the zero-energy Landau levels, the Hall conductance jumps directly from positive to negative conductance values, i.e. from ge^2/h to $-ge^2/h$, where g is the number of degeneracies, as the system is tuned through the charge neutral point.

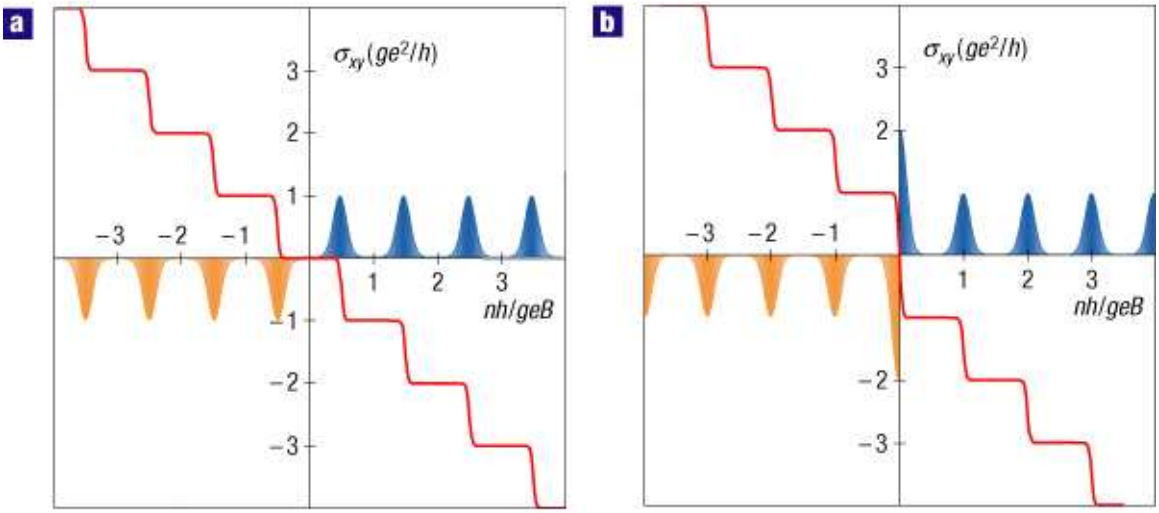

Figure 4.14 : Schematic representation of quantum Hall effects for regular fermions in semiconducting structures in a) and for chiral fermions in b). Dependence of Hall conductivity σ_{xy} on carrier density is the same at all filling factors ν, except at $\nu = 0$. Unlike regular fermions in a), chiral fermions in b) show no plateau at $\nu = 0$, but a double step from $+e^2/h$ to $-e^2/h$ [87].

In Fig. 4.15 we plot Hall and longitudinal conductivities σ_{xx} and σ_{xy} versus front gate bias, at different values of back gate bias, while the perpendicular field is fixed at $B = 4.13\,\mathrm{T}$. As V_{front} is tuned across the hybridization gap, σ_{xy} changes sign indicating a transition from the electron to hole dominated regime. On the electron side, clear plateaus in σ_{xy} are observed, while concomittantly σ_{xx} goes to zero. For $V_{back} = 8\,\mathrm{V}$ (red trace) the sample is in an inverted regime, and the last well resolved plateau on the electron side is at $\nu = 4$, while lower filling factors are irregular

and away from the quantized value due to the electron-hole coupling and consequent hybridization. Because $\nu < 4$ plateaus are not developed, one can estimate electron-hole resonance or anti-crossing density to be $n_{cross} \sim 3 \cdot 10^{11}\text{cm}^{-2}$. Similarly, on the hole side, $\nu = 2$ starts to develop, although away from the quantized value due to electron-hole hybridization. Note the apparent zero plateau in σ_{xy}, as expected for typical semiconducting systems. Furthermore, as V_{back} is tuned to more negative values, the overlap between $E1$ and $H1$ bands is reduced, i.e. band inversion is reduced, the anticrossing wave-vector and density are pushed to lower values, and as a result, the plateaus at lower filling factors develop fully. For example at V_{back}=$-4\,\text{V}$ (middle blue trace), all lower index quantum Hall plateaus are developed on the electron side, including $\nu = 1$, indicating anticrossing density $n_{cross} < 1 \cdot 10^{11}\text{cm}^{-2}$ and hence only a small overlap between $E1$ and $H1$ bands, i.e. E_{g0} of few meVs. Similarly, on the hole side well resolved $\nu = 2$ plateau and features at $\nu = 4$, $\nu = 6$, and $\nu = 8$ are visible. In addition, a clear $\nu = 0$ plateau is visible. On the other hand, as V_{back} is tuned to even more negative values, the zero conductance plateu starts to lift off, suggesting a transition from an ordinary fermion type quantum Hall effect to a chiral fermion quantum Hall effect, as expected when the critical point where $E1 = H1$ is approached.

This is even more apparent in corresponding R_{xy} plots which we show in Fig. 4.16 (top panel). Note that in these experiments we have actually measured R_{xy} and R_{xx}, but we have chosen to show $\sigma_{xy} = \frac{R_{xy}}{r_{xx}^2+R_{xy}^2}$ and $\sigma_{xx} = \frac{r_{xx}}{r_{xx}^2+R_{xy}^2}$, where $r_{xx} = R_{xx} \cdot W/L$,

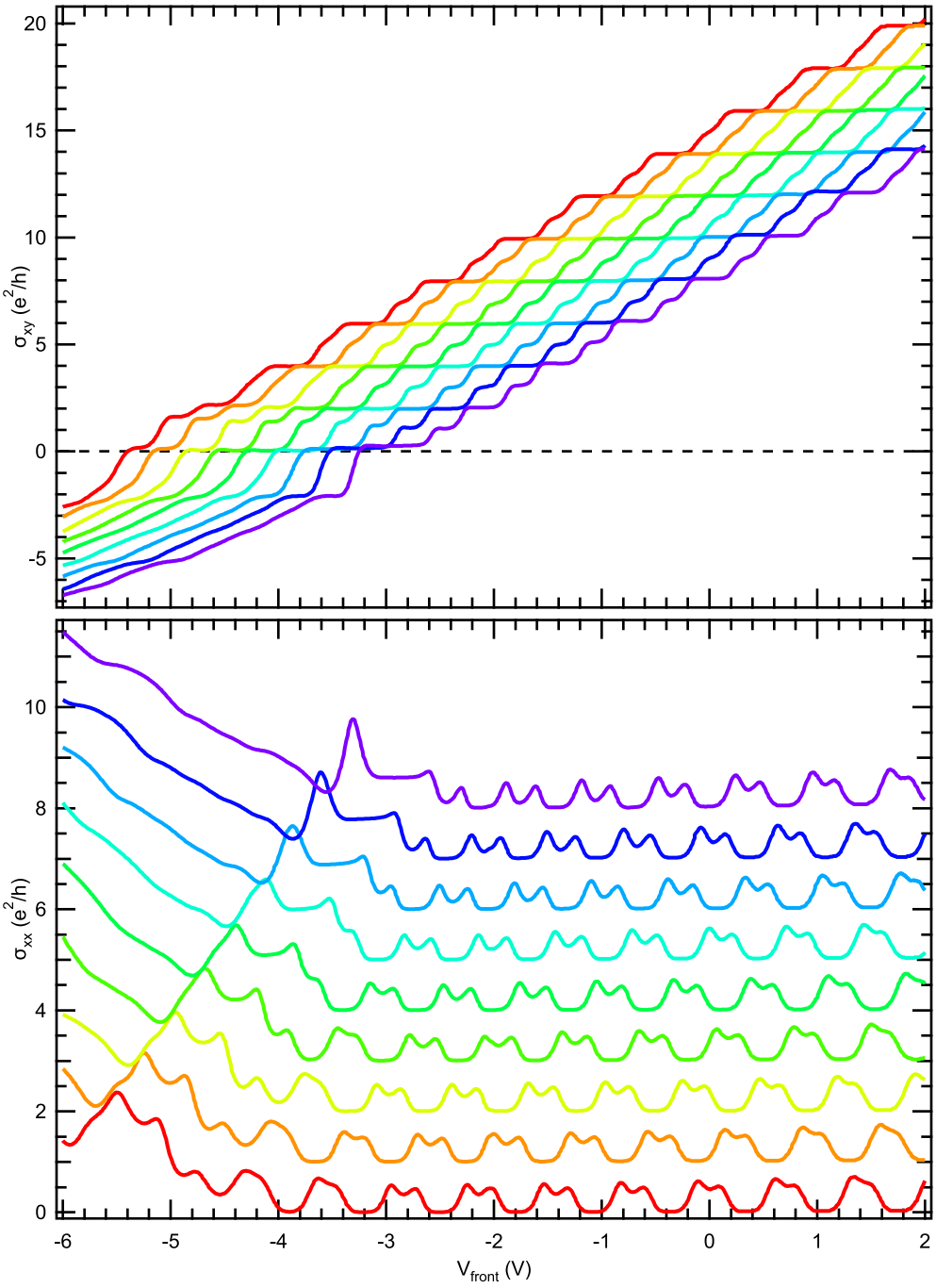

Figure 4.15 : Shows Hall and longitudinal conductivities, σ_{xy} and σ_{xx}, in top and bottom panels, versus V_{front}, and for $V_{back} = 8\,\mathrm{V}$, $4\,\mathrm{V}$, $2\,\mathrm{V}$, $0\,\mathrm{V}$, $-2\,\mathrm{V}$, $-6\,\mathrm{V}$, and $-8\,\mathrm{V}$ (red to violet); $B = 4.13\,\mathrm{T}$, $T = 20\,\mathrm{mK}$. The system is tuned from the deeply inverted regime to the critical regime where the E1 and H1 bands are degenerate, and quasiparticles are chiral fermions.

mainly for the sake of clarity in data presentation. Nevertheless, for the purpose of discussing featues at $\nu = 0$, looking at R_{xy} is more informative, as it magnifies small changes in the zero-plateau as the band structure is tuned towards the critical point. For V_{back} values of 8 V down to -2 V, clear zero-step features are visible. However, as V_{back} is made more negative to -4 V, -6 V, -8 V, and the system is pushed towards the critical point, where band ordering changes, the zero-step feature in Hall resistance is lifted and the quantum Hall system becomes of a chiral fermion type analogous to bilayer graphene. Hence, we have shown that the band structure in the InAs/GaSb system can be tuned from the deeply inverted regime, where the system exhibits massless Dirac fermions at sample edges, towards the critical regime, where $E1$ and $H1$ subband edges are near degenerate and the quasiparticles are massive Dirac or chiral fermions. As a side note, the critical regime has also been explored in HgTe/CdTe QWs in Ref. [90], but their data shows a clear zero σ_{xy} plateau, which is contrary to the chiral fermion characteristic (see Fig. 4.14), and in their case the zero-energy Landau levels have been inferred only by extrapolation. This is mainly due to the fact that their system can be tuned in discrete steps and may not have been exactly at the critical point, while here we tune the system in-situ and in a continuous fashion.

Finally, for completeness we also show B/eR_{xy} versus V_{front} for the same experiments in the bottom panel of Fig. 4.16. For larger V_{back}, B/eR_{xy} shows non-linear behavior in the hole regime, indicating two-carrier transport (Eq. (3.4)) and hence

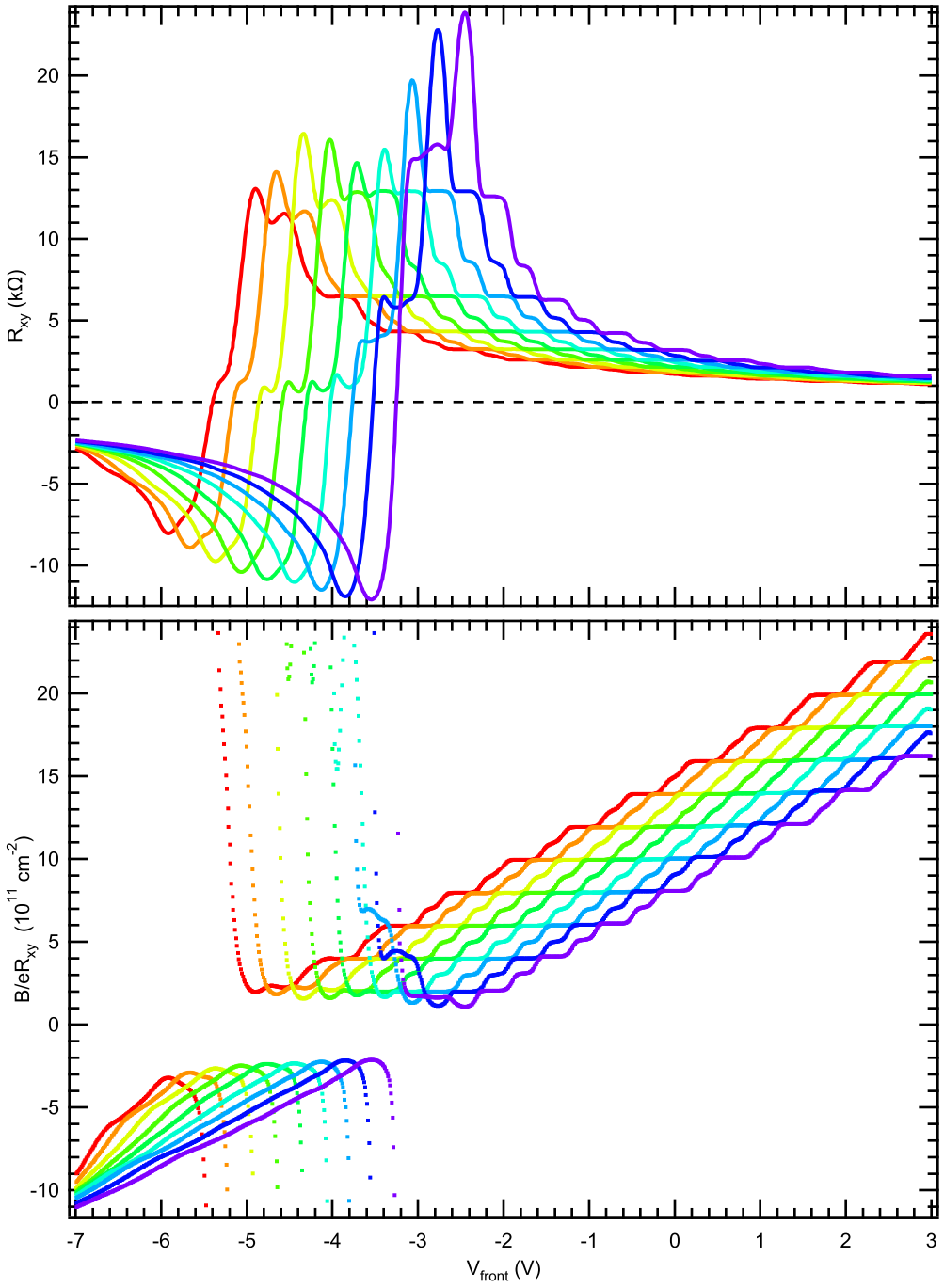

Figure 4.16 : Top panel shows Hall resistance R_{xy} versus V_{front} for the same experiment presented in 4.15. For $V_{back} = -8\,\mathrm{V}$(in violet) the system switches from $-h/2e^2$ towards $+h/e^2$ without a zero step in R_{xy} as expected for chiral fermions and in analogy to bilayer graphene. Bottom panel shows B/eR_{xy} versus V_{front} for the same experiment, where for $V_{back} = -8\,\mathrm{V}$, B/eR_{xy} (violet) trace is near-linear in both electron and hole regime, indicating single carrier transport and near-normal band ordering.

band inversion, while for $V_{back} = -8\,\mathrm{V}$, the B/eR_{xy} trace is near-linear in both the electron and hole regimes, indicating single carrier transport and near-normal band ordering. We have thus clearly demonstrated that the band structure in our system can be tuned from the deeply inverted to the critical regime. However, due to the limiting operating range of our back gates, the deeply normal regime in these 125 Å InAs/50 Å GaSb wells has remained outside of our experimental reach. Nevertheless, transport in this regime is also important, because it provides an important comparison and validation of data presented in support of helical edge modes in the inverted regime. For this purpose we have studied even narrower quantum wells, which are in the normal regime as grown. We present this data in the following section.

4.8 Transport in structures without band inversion

In this section we look into the transport behavior of 80 Å InAs/80 Å GaSb wells. These devices are also top gated, and the fabrication and characterization procedure is similar to the ones presented previously for wider wells. As the width of the quantum wells is reduced, the $E1$ subband is shifted upwards and $H1$ is shifted downwards resulting in normal band structure, with hole states being lower in energy then electron states. Note that for the same reduction in well width, the $E1$ subband experiences a shift which is an order of magnitude larger than the corresponding shift in the $H1$ subband due to the much smaller effective mass of electrons. As a result, the character of the band structure, i.e. whether it is inverted or normal is mostly

determined by the width of InAs layer, while the width of GaSb layer plays only a minor role. According to the theoretical 8-band $k \cdot p$ calculation [8], the critical InAs thickness at which the band structure changes from inverted to normal is $\sim 9\,\mathrm{nm}$, and hence our $8\,\mathrm{nm}$ structure is in the normal regime.

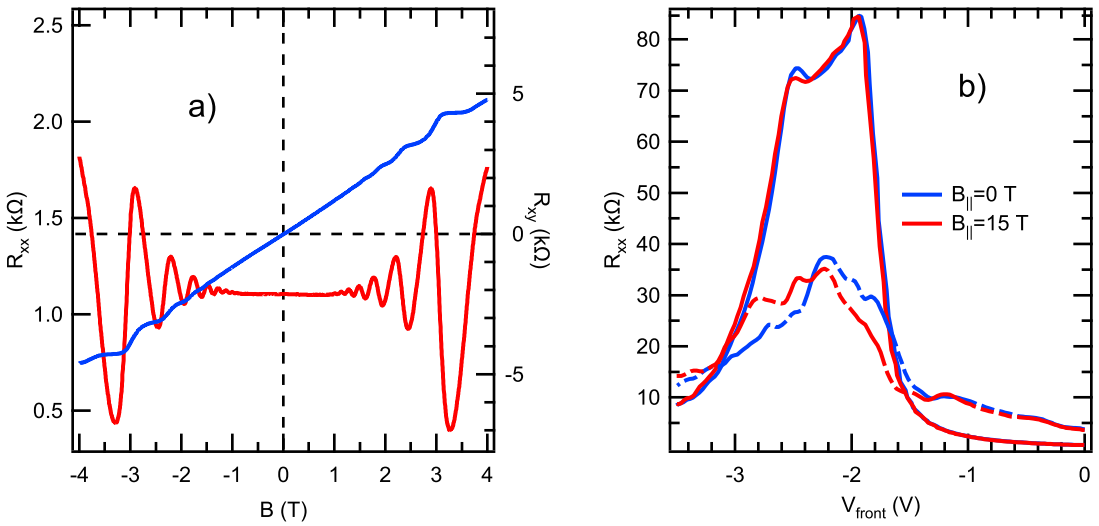

Figure 4.17 : Panels a) shows magnetotransport in 80 Å InAs/80 Å GaSb wells, which are in the normal regime. In this case gate bias is grounded. Panel b) shows R_{xx} versus V_{front} at in-plane magnetic fields of 0 T (blue), and 15 T (red) for macroscopic (full line) and mesoscopic structures (dashed line). Transport is indifferent on in-plane fields confirming that $E1 > H1$. Also shape of the resistance peak is significantly different, being much wider as compared to resistance peaks in inverted structures. Note that difference in conductance between mesoscopic and macroscopic structures is $\sim 0.3e^2/h$ and can be fully accounted by localization type logarithmic correction to conductivity, unlike in inverted structures where such difference is $\sim 4e^2/h$.

This is also evident from the transport data under in-plane magnetic fields shown in Fig. 4.17 b), where we show the longitudinal resistance R_{xx} versus V_{front} for a macroscopic $50\,\mu\mathrm{m} \times 100\,\mu\mathrm{m}$ device (full line) and a mesopic $1\,\mu\mathrm{m} \times 2\,\mu\mathrm{m}$ device

(dashed line). Measurements are performed at in-plane magnetic fields of 0 T (blue) and 15 T (red). Transport is notably insensitive to in-plane fields, and hence, according to the discussion presented earlier in Fig. 4.12 the system has normal band structure alignment with $E1 > H1$. Note that the difference in conductance between mesoscopic and macroscopic structures is $\sim 0.3e^2/h$ and can be fully accounted by logarithmic correction to conductivity due to localization, unlike in inverted structures where such difference is $\sim 4e^2/h$ even for structures whose bulk is comparably resistive to normal structures presented here. This confirms that edge conduction which is observed for wider structures in mesoscopic devices, is due to the topological reasons, i.e. band inversion, and is guaranteed by band considerations alone.

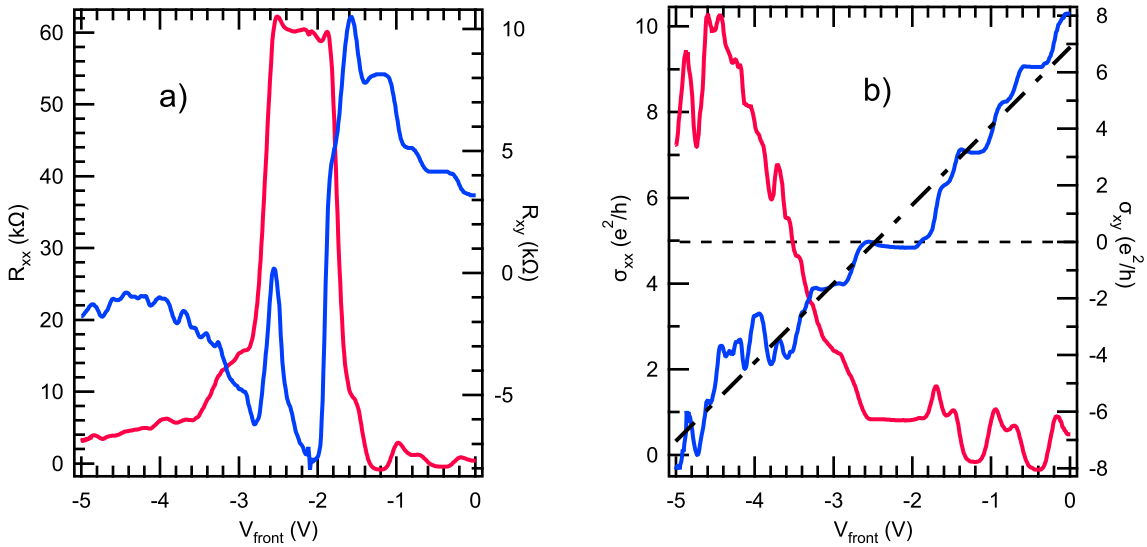

Figure 4.18 : Shows R_{xx} and R_{xy} versus V_{front} in a) and similarly σ_{xx} and σ_{xy} in b) for a macroscopic device, under prependicular field $B = 5$ T. σ_{xy} shows linear dependence on V_{front} (dashed), as the sysytem is switched from electron to hole conduction, indicating single carrier regime and hence normal band ordering ($E1 > H1$).

As mentioned earlier, in these narrower wells carrier mobility is significantly suppressed to about $\sim 2 \cdot 10^4\,\mathrm{cm}^2/\mathrm{V} \cdot \mathrm{s}$ due to interface scattering. Nevertheless, clear SdH and quantum Hall plateaus are still observed as presented in Fig. 4.17 a). Note that these structures show significantly higher contact resistance due to the reduced mobility of the 2DEG in the Hall bar arms, which results in an overall lower quality of SdH and QHE features. This is particularly evident in Fig. 4.18, which shows R_{xx} and R_{xy} versus V_{front} in a) and similarly σ_{xx} and σ_{xy} in b) under a perpendicular field of $B = 5\,\mathrm{T}$. Note that σ_{xy} shows a linear dependence on V_{front} (dashed-line), as the system is switched from electron to hole conduction, indicating a single-carrier regime and hence normal band ordering ($E1 > H1$). This is because in InAs/GaSb QWs two-carrier transport is possible only in the inverted regime, where both electron and hole Fermi surfaces may exist. Furthermore, a clear plateau at $\nu = 0$ is observed in σ_{xy}, and similarly, a zero resistance feature in R_{xy}, as expected for a trivial semiconducting system. A strong oscillation in R_{xy} near $\nu = 0$ may be an artifact due to capacitive coupling and high contact resistance. Nevertheless, oddly enough, on the electron side $\nu = 5$ and $\nu = 3$ are much better developed than $\nu = 2$ and $\nu = 4$.

Finally, transport in 80 Å InAs/80 Å GaSb quantum wells indicates that these structures clearly have normal band ordering with the lowest electron states higher in energy than the highest hole states. As expected, magnetotransport shows typical features found in ordinary semiconducting systems, while the scaling of the gap resistance with length can be fully accounted for within logarithmic correction due to

localization. This validates the picture of helical edge conduction in wider structures with inverted band alignement, and confirms the topological argument that the edge modes in this system are solely guaranteed by topological ordering of the bands.

4.9 Discussion and implications

Work presented in this chapter [45, 46] clearly establishes the InAs/GaSb system as a quantum Spin Hall or 2D topological insulator, making it a great alternative to another model QSH system of HgTe/CdTe. In fact, this system shows far better tunability, especially via back gates, allowing us to continuously tune the system from the inverted regime to the critical point, and allowing us to probe the topological phase transition in a continuous fashion. Nevertheless, there is much room for improvement. The back gate action in this system can be significantly improved via back-side processing, allowing a transition from the inverted to the normal regime in a single bias swing. Due to its chemical properties, antimonides are ideally suited for flip-chip techniques, which are already well developed for GaAs [91] and directly applicable here. This will enable the probing of the helical edge channels via scanning probe techniques [92, 93], which at this point in HgTe/CdTe are very much limited due to the lack of effective back gates. An improvement may also come by growing structures on lattice-matched GaSb substrates, which is in progress as of writing this thesis. Furthermore, a particular appeal for this system comes from its low Schottky interface and transparent interfaces to superconductors, opening a possibility for re-

alization of Majorana bound states and topological qubits [10]. While at this point it is not clear whether such topological qubits would be substantially better than any other qubit realizations [94, 95], this is nevertheless an important research direction, which has been also pursued in this thesis, and will be discussed in its remainding part.

Nevertheless, here we pause for a momement to dispel a common misunderstooding that arises in the research community, which often regards inverted InAs/GaSb to be bulk conductive. This is only partially true and disregards the fact that bulk conductivity in inverted InAs/GaSb is in its magnitude a band structure effect [41, 45, 46, 40], and hence can be easily tuned in a very large range as demonstrated in this chapter. Fig. 4.19 shows bulk resistance versus anticrossing density, i.e. density when $n_{cross} = n \sim p$ for two inverted structures presented in this thesis. As the anticrossing point is pushed to lower resonance densities, i.e. lower n_{cross}, the bulk resistance is increased by two orders of magnitude. In fact, in the limit of low n_{cross}, the bulk resistance is comparable to values reported for HgTe/CdTe. The edge resistance in this case is about an order of magnitude smaller, and hence majority of transport occurs along sample edges. As a result, InAs/GaSb is a robust QSH system, which can be sufficiently insulating in the bulk to observe clear edge effects in transport. In the next chapter, we interface our structures with superconducting electrodes, probing the topological protection of helical edges against backscattering.

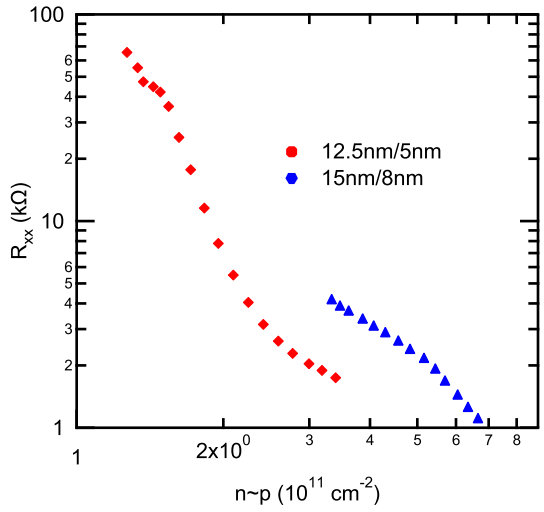

Figure 4.19 : Shows bulk resistance versus anticrossing density, i.e. density when $n_{cross} = n \sim p$ for two inverted structures presented in this thesis. As the anticrossing point is pushed to lower resonance densities, i.e. lower n_{cross}, bulk resistance is increased by two orders of magnitude, and in this limit is comparable to values reported for model QSH system of HgTe/CdTe. Note that edge resistance in this case is about an order of magnitude smaller, and hence the majority of transport occurs along the sample edges.

Chapter 5

Probing Helical Edge Channels via Andreev Reflection Measurements

5.1 Andreev reflection in QSH systems

A remarkable property of quantum spin Hall edge modes is their inherent protection against elastic backscattering. As we have seen in the previous chapter, this has a notable impact on transport properties leading to nearly quantized conductance values in mesoscopic structures. Additional insight regarding the dissipationless character of quantum spin Hall edges can be obtained by combining QSHI with superconductors [96, 97, 98], and probing the helical edge modes via Andreev reflection measurements. Marrying 2D TIs with superconductors is also the next experimental challenge, posing fundamental questions regarding the nature of topological superconductors and the possible realizations of Majorana fermion excitations. As suggested earlier, the InAs/GaSb material system is well suited for the task, due to its low Schottky barrier and its good interface to superconductors.

Andreev reflection is a process unique to a superconductor-normal metal (S-N) interface, where an impinging normal quasiparticle retroreflects, having thus not only opposite velocity but also opposite charge, and resulting in the enhancement of the total current across the interface. The electrical current through a single S-N interface

can be calculated using the Blonder-Tinkham-Klapwijk (BTK) model [99]:

$$I = \frac{N \cdot e}{h} \int \left[f\left(E + eV\right) - f\left(E\right) \right] \left[1 + A\left(E\right) - B\left(E\right) \right] dE \tag{5.1}$$

where N is the number of modes in the normal conductor, $f\left(E\right)$ is the equilibrium Fermi distibution function, V is the voltage drop at the interface, and $A\left(E\right)$ and $B\left(E\right)$ are the probabilities for Andreev and normal reflection of the electron at the interface. In the case of an ideal interface, and for biases within the superconducting gap, quasi-particles are only Andreev reflected, i.e for $V < \frac{\Delta_S}{e}$, where Δ_S is the size of the superconducting gap. This is because there are no states within the superconducting gap, excluding the possibility of electron transmission, and there is no potential barrier which would absorb the momentum difference necessary for normal reflection. In practice, due to native oxides or Schottky barriers, a potential step always exists at the S-N interface, allowing for normal reflection, and hence reducing the probability for Andreev reflection. The interface barrier is characterized by the scattering parameter Z, which is related to the normal transmission of the barrier as $T = \frac{1}{1+Z^2}$. For $Z < 1$, Andreev reflection dominates over normal reflection, resulting in zero bias dips in differential resistance dV/dI. In this case, current enhancement due to Andreev reflection also manifests itself as an excess current I_{excess}, which is obtained by extrapolating the linear $I - V$ curve at high biases, i.e. for $V \gg \frac{\Delta_S}{e}$, to zero bias.

In the case of a S-QSH single edge interface, the absence of backscattering channels

in the helical edge requires normal reflection probability $B(E) = 0$ [97]. Within the superconducting gap ($E < \Delta_S$), electron transmission is excluded, requiring a perfect Andreev reflection with probability $A(E) = 1$. Evaluating equation (5.1) in the zero temperature limit for this case gives a contact resistance for a single helical edge channel of $\frac{h}{4e^2}$ for biases within the superconducting gap, i.e. $V < \frac{\Delta_S}{e}$. In the two-terminal geometry used in our experiments, this gives a resistance of each helical edge mode to be $\frac{h}{4e^2}+\frac{h}{4e^2}=\frac{h}{2e^2}$, assuming independence of two S-QSH interfaces, which gives a total two-terminal resistance of $\frac{h}{2e^2}||\frac{h}{2e^2} = \frac{h}{4e^2}$. On the other hand, for $V \gg \frac{\Delta_S}{e}$, electron transmission into the superconducting lead becomes possible and Andreev reflection probability scales to zero as $A(E) \backsim \left(\frac{\Delta_S}{E}\right)^2 \to 0$, reducing equation (5.1) to the familiar case of N-QSH interface with a contact resistance of $\frac{h}{2e^2}$. Simple resistance combination now gives a total two-terminal resistance of $\frac{h}{2e^2}$.

As a result, this analysis suggests that replacing the normal electrodes with superconducting electrodes results in a doubling of the conductance across the device, which would be a clear indication of the dissipationless character of helical edge modes. We note that this analysis breaks down when the two S-QSH interfaces are not independent, which is the case when the two superconducting electrodes are close enough so that electrons can travel coherently from one electrode to another and back. In this case, Andreev bound states form, which are discrete levels within the superconducting gap and can carry the supercurrent [100]. In this case, S-QSH-S junctions show a unique current phase relationship, indicative of the presence of the Majorana bound

states [101]. This was the ultimate goal of the experiments presented here, but due to fabrication/measurement limitations it has remained elusive as of the writing of this thesis.

5.2 Device fabrication and measurement setup

The experiments were performed on 125 Å InAs/50 Å GaSb quantum wells in the inverted regime, whose characterization data has been thoroughly discussed in the previous chapter. In order to probe the helical character of the edge modes, superconducting niobium electrodes with a critical temperature of $T_c = 8.27\,\mathrm{K}$ (BCS gap of $\Delta_S = 1.24\,\mathrm{meV}$) are deposited directly on the InAs layers, while the electrostatic front gate is used to tune the Fermi energy E_F into the hybridization regime. Devices are patterned in a superconductor-normal metal-superconductor (S-N-S) junction geometry. Fig. 5.1 shows a device cross-section and top view obtained via scanning electron microscopy. Contact regions are patterned via e-beam lithogaphy and etched down to the InAs layer, after which niobium electrodes are deposited via magnetron sputtering. Prior to niobium deposition, the devices are plasma-cleaned in argon atmosphere. The front gate is fabricated by depositing Si_3N_4 using a plasma enhanced chemical vapor deposition system, and evaporating a Ti/Au metal gate, similar to what was reported in previous parts of the thesis. Our devices are current biased via a Keithley 6221 current source, while the corresponding source to drain voltage drop is measured via a Keithley 2182 Nanovoltmeter in quasi-four terminal geometry. Gate

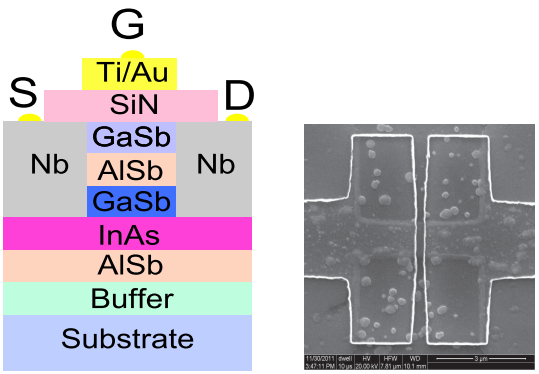

Figure 5.1 : Left panel shows device cross-section while the right panel shows top view of the S-N-S device obtained via scanning electron microscopy.

bias is applied via a Keithley 2400 source/measure unit, and controlled in LabView, via the GPIB interface. Measurements are performed in a ^{3}He refrigerator (300 mK) combined with a 3 T/2 T superconducting vector magnet.

5.3 Andreev reflection in the hybridization regime of InAs/GaSb QWs

In this experiment we tune the Fermi energy into the hybridization regime and vary the source to drain current across the device, while measuring the corresponding voltage drop. Fig. 5.2 shows the experimentally obtained 3D plot of dV/dI vs bias voltage V across the S-InAs/GaSb-S junction (S to D leads in Fig. 5.1, left panel) and front gate bias V_{front} (G lead in Fig. 5.1, left panel). We first note strong zero bias dips in differential resistance for all values of V_{front}. This indicates that conduction is enhanced irrespective of the position of the Fermi level and that Andreev reflection processes clearly dominate over normal reflecton processes. Furthermore,

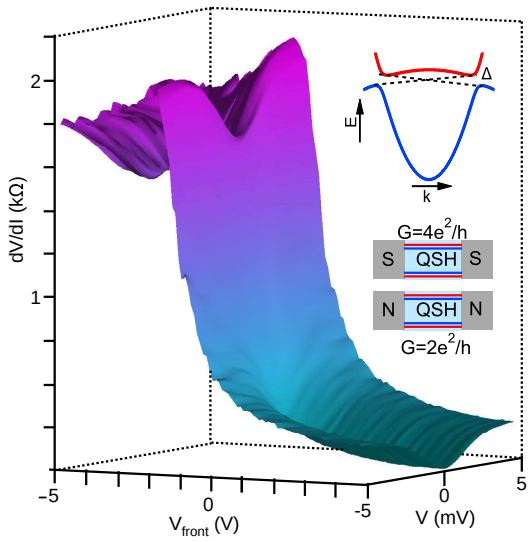

Figure 5.2 : Figure shows differential resistance dV/dI vs bias voltage V across the S-InAs/GaSb-S junction and vs front gate bias V_{front}. Top inset shows energy spectrum of inverted InAs/GaSb QWs with linearly dispersing helical edge modes in the mini-gap. As the Fermi level E_F is tuned across the mini-gap via V_{front}, dV/dI exhibits a strong peak at larger V. On the other hand, for V close to zero, dV/dI exhibits strong dips, suggesting transport dominated by Andreev reflection processes. Bottom inset shows two-terminal structure with superconducting and normal leads. Due to the perfect Andreev reflection at S-QSH interfaces, the voltage drop at each contact is halfed, leading to a doubling of the differential conductance compared to the N-QSH case [47].

the differential resistance at higher biases, i.e. dV/dI for $V \gg \frac{\Delta_S}{e}$, also dubbed normal resistance R_N, shows a clear peak as the Fermi level E_F is tuned into the mini-gap via V_{front}, indicating that the hybridization gap is clearly accessible in our measurements.

Besides the normal resistance, another characteristic parameter which can be extracted from $I-V$ measurements is the excess current, I_{excess}, which is obtained by extrapolating the linear portion of the $I-V$ curve at high biases to zero bias as explained earlier. In this case, the parameter $\frac{e \cdot I_{excess} \cdot R_N}{\Delta_S}$ is a dimensionless quantity,

indicative of the transmissivity of the S-N interface [99, 102, 103]. Fig. 5.3 a) shows normal resistance R_N vs V_{front} (in blue) and I_{excess} vs. V_{front} (in red). As E_F is tuned towards the mini-gap, R_N increases towards the peak value of $\sim 2\,\mathrm{k}\Omega$, signaling mini-gap entry, while concurrently I_{excess} decreases from the maximal value of $\sim 2.6\,\mu\mathrm{A}$ to the mini-gap value of $I_{excess} \sim 150\,\mathrm{nA}$. Furthermore, in Fig. 5.3 b) and c) we plot $I-V$ and $dV/dI-V$ curves for these two cases, i.e. for $V_{front} = 5\,\mathrm{V}$ where $I_{excess} \sim 2.6\,\mu\mathrm{A}$ and E_F above the hybridization gap, and for $V_{front} = -2.1\,\mathrm{V}$ where $I_{excess} \sim 150\,\mathrm{nA}$ and E_F is in the hybridization gap, respectively. Strong zero-bias dips in the $dV/dI-V$ curve are observed, while $I-V$ shows evident non-linear character. For E_F above the hybridization gap, the scattering parameter of the barrier can be estimated from the ratio $\frac{e \cdot I_{excess} \cdot R_N}{\Delta_S} \sim 0.76$, to give $Z = 0.65$ and normal transmissivity of $T = 0.7$ [103, 102]. This transmissivity is only slightly lower than the largest reported value of 0.86 for the InAs material system, indicating a very good quality of our devices.

On the other hand, the mini-gap case requires more thorough discussion. According to BTK theory, the maximal value of $\frac{e \cdot I_{excess} \cdot R_N}{\Delta_S} = \frac{8}{3}$ for perfectly transmissive interfaces, i.e. when $A = 1$ [103]. In the case of S-QSH-S structures normal resistance is $\frac{h}{2e^2}$ so the maximal excess current that can be obtained for perfectly transmissive helical edge modes with zero backscattering is $I_{excess} = \frac{16}{3}\frac{e\Delta_S}{h} \sim 250\,\mathrm{nA}$. However, in our devices we also have a conductive bulk, with bulk normal resistance of approximately $\sim 2.4\,\mathrm{k}\Omega$ and carrier density of $n \sim 5 \cdot 10^{10}\mathrm{cm}^{-2}$. These bulk states can also

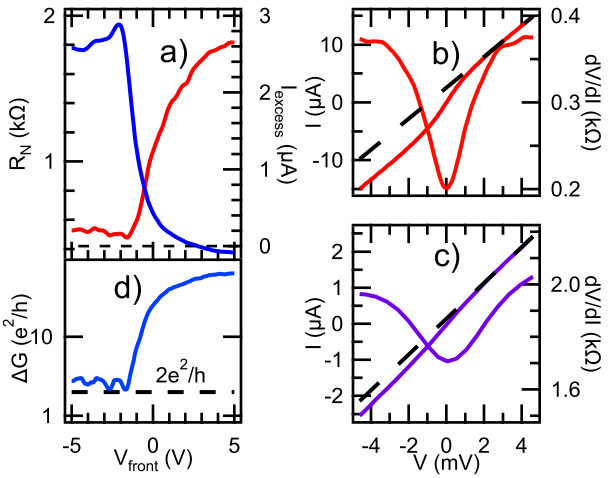

Figure 5.3 : Panel a) shows normal resistance R_N (in blue) and excess curent due to Andreev reflection I_{excess} (in red) vs V_{front}. As V_{front} is decreased, E_F is tuned towards the mini-gap and R_N increases towards the peak value of $\sim 2\,\mathrm{k}\Omega$, while concurrently I_{excess} decreases from the maximal value of $\sim 2.6\,\mu\mathrm{A}$ ($V_{front} = 5\,\mathrm{V}$) to the mini-gap value $I_{excess} \sim 150\,\mathrm{nA}$ ($V_{front} = -2.1\,\mathrm{V}$). Panel b) and c) show dV/dI and I vs V for $V_{front} = 5\,\mathrm{V}$ and $V_{front} = -2.1\,\mathrm{V}$ respectively. Excess current is determined as an intercept of the linear fit to the $I - V$ curve for large V. Panel d) shows the conductance difference $\Delta G \equiv G\,(V = 0) - G\,(V \gg \Delta_S/e)$ vs V_{front} on a log scale. For E_F in the mini-gap ΔG plateaus at $2e^2/h$, indicating perfect Andreev reflection of helical edge channels [47].

contribute to Andreev reflection, thus increasing the excess current; however, at such low carrier densities, disorder generally dominates and a possible bulk contribution to Andreev processes and excess current is expected to be small. On the other hand, a sufficiently conductive bulk can also reduce the total edge conductance as shown in the previous chapter, leading to an increased normal resistance of the edge and hence reduction of the edge excess current. This may explain the slightly smaller measured value of 150 nA in Fig. 5.3 a) and c).

Furthermore, as explained earlier and illustrated in the inset of Fig. 5.2, due to the absence of backscattering channels in helical edges, edge conductance will be doubled from $2e^2/h$, when there is no Andreev reflection such as in normal electrodes or superconducting electrodes at high biases, to $4e^2/h$ for superconducting electrodes at zero bias. As a result, the difference between two-terminal conductances at zero and high biases will be: $\Delta G \equiv G\left(V=0\right) - G\left(V \gg \Delta_S/e\right) = \frac{2e^2}{h}$. Note that in Fig. 5.3 c), where E_F is in the hybridization gap, $\frac{dV}{dI}\left(V=0\right) \sim 1.7\,\mathrm{k\Omega}$, while $\frac{dV}{dI}\left(V \gg \Delta_S/e\right) \sim 2\,\mathrm{k\Omega}$. Inverting these two values gives $\Delta G \sim 2.2\frac{e^2}{h}$, which is suprisingly close to the expected value of $\frac{2e^2}{h}$. This is better illustrated in Fig. 5.2 d), which shows plateauing of ΔG to a conductance value of $\frac{2e^2}{h}$, as E_F is pushed into the hybridization gap, validating the picture of perfect Andreev reflection of helical edge channels.

Nevertheless, we note that this may not be the only explanation of our data. In fact, instead of two ideally transmitted edge channels, the data may also be potentially understood in terms of a larger number of channels with non-ideal Andreev reflection,

i.e. $A < 1$. Because resistance dips are present for all values, then it follows that the Andreev probability is larger than the normal reflection probability, i.e. $A > B$ at zero bias. Also, because at zero bias transmission is excluded, we have that $A+B = 1$, so it follows that $A > 0.5$. Also, from Eq. (5.1) $\Delta G \sim \frac{e^2}{h} N \cdot A \sim 2\frac{e^2}{h}$, so it follows that $N \lesssim 4$. This is in clear contradiction with the number of bulk channels estimated from the bulk carrier density. In this case, the Fermi-wavelength which corresponds to a bulk carrier density of $n \sim 5 \cdot 10^{10}\mathrm{cm}^{-2}$ is $\sim 100\,\mathrm{nm}$, which for a device width of $\sim 1\,\mu\mathrm{m}$ gives the number of bulk channels as $N \gtrsim 20$. As a result, the edge picture certainly explains our data better, although bulk contribution cannot be fully excluded. Next, we look into temperature and magnetic field dependence for potential clues regarding the origin of the excess current in our devices.

5.4 Temperature dependence

The temperature dependence of excess current I_{excess} in Fig. 5.4 a) shows only a weak dependence for temperatures up to 6.5 K and it is quickly suppressed as the temperature is further increased towards the critical temperature of niobium leads. Furthermore, a color map of temperature evolution of dV/dI is shown in Fig. 5.4 b), with dips in dV/dI closely following the BCS temperature dependence [104] of superconducting gap Δ_S. We note here that I_{excess} for E_F, both inside and outside of the mini-gap, shows comparative suppression when Δ_S is reduced with increased temperature. This is most easily seen when I_{excess} is normalized by the corresponding

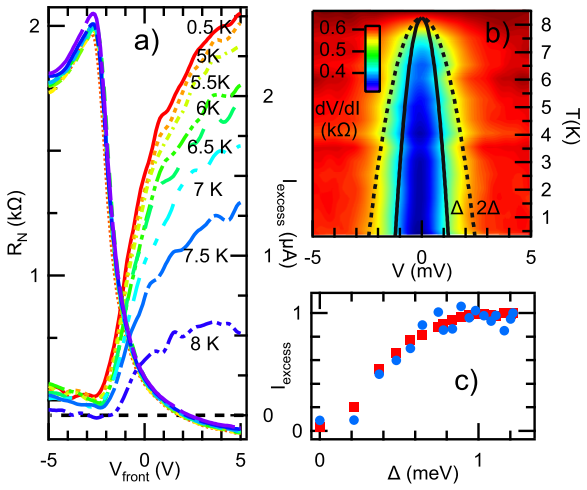

Figure 5.4 : Panel a) shows R_N and I_{excess} vs V_{front} for temperature T=0.5 K, and T from 5 K to 8 K varied in 0.5 K increments. Dependence is exceptionally weak except when T approaches $T_c = 8.27$ K. Panel b) shows a color map of dV/dI vs V and T ($V_{front} = 0$ V). Full and dashed lines show BCS dependence of the superconducting gap Δ_S/e and $2\Delta_S/e$ respectively. Dips in dV/dI follow closely the BCS gap Δ_S. Panel c) shows normalized I_{excess}, i.e. $I_{excess}(T)/I_{excess}(300\,\text{mK})$, vs $\Delta_S(T)$ for E_F above the mini-gap (in red) and E_F in the mini-gap (in blue). In both cases, normalized I_{excess} shows equal decrease as the Δ_S is reduced with T [47].

low temperature values, i.e. $I_{excess}(T)/I_{excess}(300\,\text{mK})$ and plotted in Fig. 5.4 c) for these two cases.

5.5 Magnetic field dependence

On the other hand, the equal suppression of excess current with reduced temperature for the two cases when the Fermi level is inside and above the hybridization gap is in sharp contrast to the magnetic field dependence of excess current shown in Fig. 5.5. In this case, for a Fermi level in the mini-gap, excess current is suppressed much faster than in the case when the Fermi level is outside of the mini-gap. In fact, perpendicular magnetic fields of less than 50 mT are sufficient to fully supress Andreev reflection

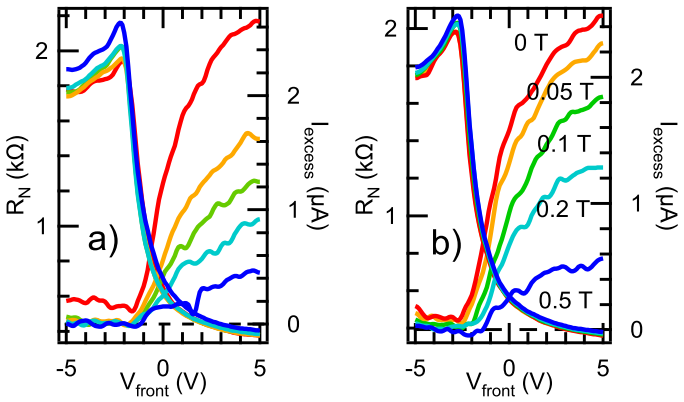

Figure 5.5 : Panels show R_N and I_{excess} vs V_{front} for perpendicular magnetic fields of $B_\perp = 0\,\mathrm{T}$, $0.05\,\mathrm{T}$, $0.1\,\mathrm{T}$, $0.2\,\mathrm{T}$, and $0.5\,\mathrm{T}$ in a) and in b) for in-plane magnetic fields $B_{||}$ with the same increments. Although for E_F above the hybridization gap, I_{excess} survives up to $0.5\,\mathrm{T}$, for E_F in the mini-gap I_{excess} is completely supressed with $B_\perp = 0.05\,\mathrm{T}$ and $B_{||} = 0.1\,\mathrm{T}$. This is in contrast to the equal supression of I_{excess} in temperature dependence (Fig. 3c), suggesting a different nature of excess current in and outside of the hybridization gap [47].

processes in the mini-gap, while above the mini-gap Andreev reflection processes survive in fields up to at least 500 mT.

Similar disproportionality is also observed for the in-plane magnetic fields, albeit in this case the mini-gap excess current survives for fields up to 100 mT while above the mini-gap, curret enhancement due to Andreev reflection is still observable at 500 mT. Such sensitivity to time-reversal breaking indeed suggests that the observed mini-gap excess current may very well be due to the perfect Andreev reflection of helical edge modes. Applying small magnetic fields opens the backscattering channels in our structures, and perfect Andreev reflection is no longer guaranteed. In this case, the probability of Andreev reflection decreases, and excess current vanishes.

5.6 Discussion and implications

In this chapter we have studied InAs/GaSb QWs contacted via superconducting niobium electrodes, observing strong zero-bias dips in the differential resistance as the Fermi level is tuned across the mini-gap. This is indicative of dominant Andreev reflection processes at the superconducting interfaces irrespective of the position of the Fermi level, including within the mini-gap. The relative size of the dips and corresponding gap excess current are in good agreement with the prediction of perfect Andreev reflection of the helical edge modes, necessitated by the absence of backscattering channels. The perfect Andreev reflection occurs in spite of a finite barrier at the interface and shows strong sensitivity to time-reversal breaking - hallmarks of the helical nature of the QSH edges. However, the analysis is complicated by the presence of bulk states, whose contribution in this case, although expectedly small, could not be fully excluded. Back-gate dependence in this case would be immensely helpful because in this case bulk contribution can be significantly reduced; however, due to high back gate leakage currents, back-gates could not have been employed in these experiments. At this point, it is clear that until a more reliable back-gating technique is achieved no clear distinction between edge and bulk contributions in S-QSH-S structures can be made with great certainty. Instead, here we emphasize high interface transmissivity of approximately seventy percent in our devices, which is quite promising for future experiments on hybrid TI/superconducting structures. We also note here that in spite of high barrier transmissivity, the absence of super-

current in our device suggests that coherence is not preserved across the junction, presumably due to the surface degradation caused during plasma processing, as well as potential noise problems in our experimental setup. As of writing this thesis, much work has been done to re-wire our measurement probe for low noise measurements, and with further optimization in fabrication InAs/GaSb readily arises as a viable platform where theoretical predictions of Majorana fermion modes can be experimentally explored.

Chapter 6

Conclusion

In this thesis we have conducted comprehensive low temperature transport measurements on dual-gated broken gap InAs/GaSb quantum wells in both topologically trivial and non-trivial regimes. We have found that InAs/GaSb quantum wells exhibit transport properties characteristic of quantum spin Hall systems, with band structure whose inverted character is signaled by re-entrant quantum Hall behavior, and with apparent edge conduction channels which, to a degree, may persist despite conductive bulk. We have established that the origin of this residual bulk conductivity is level broadening due to disorder; however, in the clean limit, i.e. for vanishing disorder, bulk conductivity depends exclusively on band parameters, decreasing as the overlap between electron and hole bands is reduced and the critical point is approached, where band topology changes. More importantly, we have demonstrated that bulk mini-gap conductivity in this system can be tuned over two orders of magnitude, and for low values, the bulk conducitvity is comparable to the one reported for the model QSH system of HgTe/CdTe. The edge resistance in this case is about an order of magnitude smaller than that of the bulk, and the majority of transport is thus carried along the sample edges.

Edge transport is apparent even at higher values of bulk conductivity, due to Fermi velocity mismatch and edge-bulk decoupling, where four-terminal mesoscopic

samples show additional conductance of approximately $4e^2/h$ as compared to macroscopic samples, while gap conductance shows a length dependence trend which is in close agreement with the expectation for helical edge modes. In addition, the width dependence of gap conductance in the mesoscopic regime indicates clear edge conduction, in support of helical edge transport. On the other hand, topologically trivial structures do not show such additional conduction contributions at mesoscopic length scales, validating the helical edge picture in inverted or topologically non-trivial structures. Separate evidence for topological band structure is found at high magnetic fields, where band hybridization results in non-monotonic Landau levels and non-trivial magnetic properties with characteristic re-entrant quantum Hall behavior.

Furthermore, we have shown that this quantum spin Hall system shows an unprecedented degree of tunability via electrical fields, allowing us to continuously tune the system from inverted towards normal, and allowing us to probe this topological phase transition in a continuous fashion, which has not been possible in any TI system prior to this work. In fact, exactly at the critical point where the band structure changes from inverted to normal, quasiparticles are massive Dirac fermions or chiral fermions, in analogy to bilayer graphene, albeit less degenerate, with characteristic zero energy Landau levels due to a 2π Berry phase, as evidenced from our magnetotransport measurements. In consequence, besides one-dimensional massless Dirac fermions at sample edges in the inverted regime, this system also holds massive

Dirac fermions in the topologically critical regime. However, unlike bilayer graphene, InAs/GaSb in the critical regime does not have valley degeneracy, and spin degeneracy is lifted due to inversion asymmetries, allowing for the possibility of non-degenerate zero-energy modes, which when contacted with superconducting electrodes may lead to coveted topological superconductivity and exotic Majorana bound states.

In fact, a particular appeal for this system comes from its low Schottky interface and transparent interfaces to superconductors, opening a possibility for realization of Majorana bound states and topological qubits in both inverted and critical regimes. This research direction has also been the subject of this thesis in studies involving gated superconductor-InAs/GaSb-superconductor junctions. Although at this point the data is not conclusive, and supercurrent has evaded our devices, the low transparency of our junctions is very promising for future experiments, of course, with necessary improvements in fabrication. Furthermore, back-gate action in our devices can be significantly improved via backside processing, allowing even better tunability of our system. This will enable probing of 2D topological insulators via scanning probe techniques, which at this point have been very much limited. An improvement may also come by growing our structures on lattice matched GaSb substrates, resulting in a reduced number of dislocations and improved sample mobilities. Finally, InAs/GaSb is a robust and exceptionally tunable quantum spin Hall system, where interplay between Dirac physics and superconductivity can be studied and possibly utilized for realization of topological qubits. Ultimately, this may very well enable a

quantum leap towards scalable quantum computing systems.

Bibliography

[1] Klitzing, K. v., Dorda, G., and Pepper, M. *Phys. Rev. Lett.* **45**, 494–497 Aug (1980).

[2] Tsui, D., Stormer, H., and Gossard, A. *Physical Review Letters* **48**, 1559–1562 (1982).

[3] Thouless, D., Kohmoto, M., Nightingale, M., and den Nijs, M. *Physical Review Letters* **49**, 405–408 (1982).

[4] Hasan, M. Z. and Kane, C. L. *Rev. Mod. Phys.* **82**, 3045–3067 Nov (2010).

[5] Qi, X.-L. and Zhang, S.-C. *Rev. Mod. Phys.* **83**, 1057–1110 Oct (2011).

[6] Volkov, B. A. and Pankratov, O. A. *Soviet Physics Uspekhi* **29**(6), 579 (1986).

[7] Pankratov, O., Pakhomov, S., and Volkov, B. *Solid State Communications* **61**(2), 93 – 96 (1987).

[8] Liu, C., Hughes, T. L., Qi, X.-L., Wang, K., and Zhang, S.-C. *Physical Review Letters* **100**, 236601 (2008).

[9] Fu, L. and Kane, C. *Physical Review Letters* **100**, 096407 (2008).

[10] Nilsson, J., Akhmerov, A. R., and Beenakker, C. W. J. *Phys. Rev. Lett.* **101**, 120403 Sep (2008).

[11] Wilczek, F. *Nature Physics* **5**, 614–618 (2009).

[12] Ivanov, D. A. *Phys. Rev. Lett.* **86**, 268–271 Jan (2001).

[13] Read, N. and Green, D. *Phys. Rev. B* **61**, 10267–10297 Apr (2000).

[14] Nayak, C., Simon, S. H., Stern, A., Freedman, M., and Das Sarma, S. *Rev. Mod. Phys.* **80**, 1083–1159 Sep (2008).

[15] Nguyen, C., Werking, J., Kroemer, H., and Hu, E. L. *Applied Physics Letters* **57**(1), 87–89 (1990).

[16] Kane, C. and Mele, E. *Physical Review Letters* **95**, 226801 (2005).

[17] Bernevig, B. and Zhang, S.-C. *Physical Review Letters* **96**, 106802 (2006).

[18] Bernevig, B. A., Hughes, T. L., and Zhang, S.-C. *Science* **314**, 1757–61 (2006).

[19] Fu, L., Kane, C., and Mele, E. *Physical Review Letters* **98**, 106803 (2007).

[20] Hsieh, D., Qian, D., Wray, L., Xia, Y., Hor, Y. S., Cava, R. J., and Hasan, M. Z. *Nature* **452**, 970–4 (2008).

[21] Xia, Y., Qian, D., Hsieh, D., Wray, L., Pal, a., Lin, H., Bansil, a., Grauer, D., Hor, Y. S., Cava, R. J., and Hasan, M. Z. *Nature Physics* **5**, 398–402 (2009).

[22] Roushan, P., Seo, J., Parker, C. V., Hor, Y. S., Hsieh, D., Qian, D., Richardella, A., Hasan, M. Z., Cava, R. J., and Yazdani, A. *Nature* **460**(7259), 1106–1109 (2009).

[23] Zhang, T., Cheng, P., Chen, X., Jia, J.-F., Ma, X., He, K., Wang, L., Zhang, H., Dai, X., Fang, Z., Xie, X., and Xue, Q.-K. *Phys. Rev. Lett.* **103**, 266803 Dec (2009).

[24] Alpichshev, Z., Analytis, J. G., Chu, J.-H., Fisher, I. R., Chen, Y. L., Shen, Z. X., Fang, A., and Kapitulnik, A. *Phys. Rev. Lett.* **104**, 016401 Jan (2010).

[25] Cheng, P., Song, C., Zhang, T., Zhang, Y., Wang, Y., Jia, J.-F., Wang, J., Wang, Y., Zhu, B.-F., Chen, X., Ma, X., He, K., Wang, L., Dai, X., Fang, Z., Xie, X., Qi, X.-L., Liu, C.-X., Zhang, S.-C., and Xue, Q.-K. *Phys. Rev. Lett.* **105**, 076801 Aug (2010).

[26] Hanaguri, T., Igarashi, K., Kawamura, M., Takagi, H., and Sasagawa, T. *Phys. Rev. B* **82**, 081305 Aug (2010).

[27] Analytis, G. J., McDonald, R. D., Riggs, S. C., Chu, J.-H., B. G. S., and Fisher, I. R. *Nature Physics* **6**, 960–964 (2010).

[28] Analytis, J. G., Chu, J.-H., Chen, Y., Corredor, F., McDonald, R. D., Shen, Z. X., and Fisher, I. R. *Phys. Rev. B* **81**, 205407 May (2010).

[29] Butch, N. P., Kirshenbaum, K., Syers, P., Sushkov, A. B., Jenkins, G. S., Drew, H. D., and Paglione, J. *Phys. Rev. B* **81**, 241301 Jun (2010).

[30] Eto, K., Ren, Z., Taskin, A. A., Segawa, K., and Ando, Y. *Phys. Rev. B* **81**, 195309 May (2010).

[31] Checkelsky, J. G., Hor, Y. S., Cava, R. J., and Ong, N. P. *Phys. Rev. Lett.* **106**, 196801 May (2011).

[32] König, M., Wiedmann, S., Brüne, C., Roth, A., Buhmann, H., Molenkamp, L. W., Qi, X.-L., and Zhang, S.-C. *Science* **318**, 766–70 (2007).

[33] Roth, A., Brüne, C., Buhmann, H., Molenkamp, L. W., Maciejko, J., Qi, X.-L., and Zhang, S.-C. *Science* **325**(5938), 294–297 (2009).

[34] Kroemer, H. *Physica E: Low-dimensional Systems and Nanostructures* **20**, 196–203 (2004).

[35] Naveh, Y. and Laikhtman, B. *Applied Physics Letters* **66**, 1980 (1995).

[36] Yang, M., Yang, C., Bennett, B., and Shanabrook, B. *Physical Review Letters* **78**, 4613–4616 (1997).

[37] Cooper, L., Patel, N., Drouot, V., Linfield, E., Ritchie, D., and Pepper, M. *Physical Review B* **57**, 11915–11918 (1998).

[38] Kono, J., McCombe, B. D., Cheng, J.-P., Lo, I., Mitchel, W. C., and Stutz, C. E. *Physical Review B* **55**, 1617–1636 (1997).

[39] Yang, M. J., Yang, C. H., and Bennett, B. R. *Phys. Rev. B* **60**, R13958–R13961 Nov (1999).

[40] Naveh, Y. and Laikhtman, B. *Europhysics Letters* **55**, 545–551 (2001).

[41] Knez, I., Du, R. R., and Sullivan, G. *Phys. Rev. B* **81**, 201301 May (2010).

[42] Zhou, B., Lu, H.-Z., Chu, R.-L., Shen, S.-Q., and Niu, Q. *Phys. Rev. Lett.* **101**, 246807 Dec (2008).

[43] Ström, A., Johannesson, H., and Japaridze, G. I. *Phys. Rev. Lett.* **104**, 256804 Jun (2010).

[44] Väyrynen, J. I. and Ojanen, T. *Phys. Rev. Lett.* **106**, 076803 Feb (2011).

[45] Knez, I., Du, R.-R., and Sullivan, G. *Phys. Rev. Lett.* **107**, 136603 Sep (2011).

[46] Knez, I. and Du, R.-R. *Frontiers of Physics* (2011).

[47] Knez, I., Du, R. R., and Sullivan, G. *arXiv:1106.5819* (2011).

[48] Sakaki, H., Chang, L. L., Ludeke, R., Chang, C.-a., Sai-Halasz, G. A., and Esaki, L. *Applied Physics Letters* **31**, 211 (1977).

[49] Nguyen, C., Brar, B., Bolognesi, C. R., Pekarik, J. J., Kroemer, H., and English, J. H. *Journal of Electronic Materials* **22**, 255–258 (1993).

[50] Altarelli, M. *Physical Review B* **28**, 842–845 (1983).

[51] Quinn, J. *Surface Science* **361-362**, 930–932 (1996).

[52] Laikhtman, B. *Solid State Communications* **104**, 257–262 (1997).

[53] De-Leon, S., Shvartsman, L. D., and Laikhtman, B. *Physical Review B* **60**, 1861–1870 (1999).

[54] Aizin, G. R. and Gumbs, G. *Physical Review B* **64**, 125317 (2001).

[55] Naveh, Y. and Laikhtman, B. *Phys. Rev. Lett.* **77**, 900–903 Jul (1996).

[56] Chang, K. and Li, J. *Private communications* .

[57] Dohler, G. *Surface Science* **98**, 108–116 (1980).

[58] Konig, M. *Spin-related transport in HgTe-based quantum well structures.* Dissertation, University of Wurzburg, (2007).

[59] Wu, C., Bernevig, B. A., and Zhang, S.-C. *Phys. Rev. Lett.* **96**, 106401 Mar (2006).

[60] Xu, C. and Moore, J. E. *Phys. Rev. B* **73**, 045322 Jan (2006).

[61] Schmidt, T. L., Rachel, S., Von Oppen, F., and Glazman, L. I. *arXiv:1201.0278* (2011).

[62] Huichao Li, L. S. and Xing, D. Y. *arXiv:1201.1690* (2012).

[63] Winkler, R. *Spin-orbit Coupling Effects in Two-Dimensional Electron and Hole Systems.* Springer, (2003).

[64] Landauer, R. *Philosophical Magazine* **21**(172), 863–867 (1970).

[65] Büttiker, M. *Phys. Rev. Lett.* **57**, 1761–1764 Oct (1986).

[66] Buttiker, M. *IBM Journal of Research and Development* **32**, 317–334 (1988).

[67] Datta, S. *Electronic Transport in Mesoscopic Systems.* Cambridge University Press, Cambridge, (1995).

[68] Caldeira, A. O. and Leggett, A. J. *Phys. Rev. Lett.* **46**, 211–214 Jan (1981).

[69] Bolognesi, C. R., Kroemer, H., and English, J. H. *Applied Physics Letters* **61**, 213 (1992).

[70] Davies, J. *The Physics of Low-Dimensional Semiconductors.* Cambridge University Press, Cambridge, (1995).

[71] Smith, R. *Semiconductors.* Cambridge University Press, Cambridge, (1978).

[72] Millard, I. S., Patel, N. K., Simmons, M. Y., Linfield, E. H., Ritchie, D. A., Jones, G. A. C., and Pepper, M. *Applied Physics Letters* **68**, 3323 (1996).

[73] Sullivan, G. *Private communications* .

[74] Coleridge, P., Stoner, R., and Fletcher, R. *Physical Review B* **39**, 1120–1124 (1989).

[75] Coleridge, P. *Physical Review B* **44**, 3793–3801 (1991).

[76] Syed, S., Manfra, M. J., Wang, Y. J., Molnar, R. J., and Stormer, H. L. *Applied Physics Letters* **84**, 1507 (2004).

[77] Li, J., Yang, W., and Chang, K. *Physical Review B* **80**, 035303 (2009).

[78] Palevski, A., Beltram, F., Capasso, F., Pfeiffer, L., and West, K. *Physical Review Letters* **65**, 1929–1932 (1990).

[79] Ando, T., Fowler, A. B., and Stern, F. *Rev. Mod. Phys.* **54**, 437–672 Apr (1982).

[80] Kroemer, H. *Private communications* .

[81] Abrahams, E., Anderson, P. W., Licciardello, D. C., and Ramakrishnan, T. V. *Phys. Rev. Lett.* **42**, 673–676 Mar (1979).

[82] Maciejko, J., Qi, X.-L., and Zhang, S.-C. *Phys. Rev. B* **82**, 155310 Oct (2010).

[83] Nicholas, R. J., Takashina, K., Lakrimi, M., Kardynal, B., Khym, S., Mason, N. J., Symons, D. M., Maude, D. K., and Portal, J. C. *Phys. Rev. Lett.* **85**, 2364–2367 Sep (2000).

[84] Takashina, K., Nicholas, R. J., Kardynal, B., Mason, N. J., Maude, D. K., and Portal, J. C. *Phys. Rev. B* **68**, 235303 Dec (2003).

[85] Suzuki, K., Takashina, K., Miyashita, S., and Hirayama, Y. *Phys. Rev. Lett.* **93**, 016803 Jul (2004).

[86] Takashina, K., Nicholas, R. J., Kardynal, B., Mason, N. J., Maude, D. K., and Portal, J. C. *Semiconductor Science and Technology* **21**(12), 1758 (2006).

[87] Novoselov, K. S., McCann, E., Morozov, S. V., Falko, V. I., Katsnelson, M. I., Zeitler, U., Jiang, D., Schedin, F., and Geim, A. K. *Nature Physics* **2**(3), 177–180 (2006).

[88] McCann, E. and Falko, V. I. *Phys. Rev. Lett.* **96**, 086805 Mar (2006).

[89] Castro Neto, A. H., Guinea, F., Peres, N. M. R., Novoselov, K. S., and Geim, A. K. *Rev. Mod. Phys.* **81**, 109–162 Jan (2009).

[90] Büttner, B., Liu, C. X., Tkachov, G., Novik, E. G., Brüne, C., Buhmann, H., Hankiewicz, E. M., Recher, P., Trauzettel, B., and Zhang, S. C. *Nature Physics* **7**(5), 418–422 (2010).

[91] Seamons, J. A., Tibbetts, D. R., Reno, J. L., and Lilly, M. P. *Applied Physics Letters* **90**(5), 052103 (2007).

[92] Jura, M. P., Grobis, M., Topinka, M. A., Pfeiffer, L. N., West, K. W., and Goldhaber-Gordon, D. *Phys. Rev. B* **82**, 155328 Oct (2010).

[93] Lai, K., Peng, H., Kundhikanjana, W., Schoen, D. T., Xie, C., Meister, S., Cui, Y., Kelly, M. A., and Shen, Z.-X. *Nano Letters* **9**(3), 1265–1269 (2009).

[94] Goldstein, G. and Chamon, C. *Phys. Rev. B* **84**, 205109 Nov (2011).

[95] Budich, J. C., Walter, S., and Trauzettel, B. *arXiv:1111.1734* (2011).

[96] Sato, K., Loss, D., and Tserkovnyak, Y. *Phys. Rev. Lett.* **105**, 226401 Nov (2010).

[97] Adroguer, P., Grenier, C., Carpentier, D., Cayssol, J., Degiovanni, P., and Orignac, E. *Phys. Rev. B* **82**, 081303 Aug (2010).

[98] Sun, Q.-F., Li, Y.-X., Long, W., and Wang, J. *Phys. Rev. B* **83**, 115315 Mar (2011).

[99] Blonder, G. E., Tinkham, M., and Klapwijk, T. M. *Phys. Rev. B* **25**, 4515–4532 Apr (1982).

[100] Kulik, I. O. *Soviet Journal of Experimental and Theoretical Physics* **30**, 944 (1969).

[101] Fu, L. and Kane, C. L. *Phys. Rev. B* **79**, 161408 Apr (2009).

[102] Octavio, M., Tinkham, M., Blonder, G. E., and Klapwijk, T. M. *Phys. Rev. B* **27**, 6739–6746 Jun (1983).

[103] Flensberg, K., Hansen, J. B., and Octavio, M. *Phys. Rev. B* **38**, 8707–8711 Nov (1988).

[104] Bardeen, J., Cooper, L. N., and Schrieffer, J. R. *Phys. Rev.* **108**, 1175–1204 Dec (1957).

Appendix A

Recipes for Device Fabrication

Much of the experimental work presented in this thesis relies on a successful fabrication of micro and nano structures. While general processing steps are described in the main body of the thesis, the purpose of this appendix is to give more specific instructions in the form of "recipes". Nevertheless, we warn the reader that device fabrication, at least in a university setting, is more of an art than an exact science, and even subsequent processing runs under what can be nominally considered "the same" conditions can produce markedly different outcomes. As a result, no recipe can substitue common sense and persistence in sample processing, which are indeed essential for successful device fabrication.

A.1 Mask making

1. Upload mask designs to Linux conversion machine; convert and transfer the Lic files to the OS9 machine.

2. Load the mask into Heidelberg DWL mask maker.

3. Turn on the laser, center, focus, and expose the mask.

4. After mask exposure, develop the mask in a 1:5 soluion of MF-351 and DI water for approximately 60 seconds or as needed. Observe the progress/outcome under

an optical microscope.

5. Etch the chromium film in CEP-200 for approximately 60 seconds or until the metal film has been fully etched away. Monitor the progress/outcome of the etch under an optical microscope.

6. Finally, clean the photo-resist by using either photo-resist stripper PRS-100 or acetone for 2-5 minutes, or until the photo-resist is washed away.

7. Wash the mask in DI water and blow dry with nitrogen gas. Inspect under an optical microscope.

A.2 Device patterning

Device patterning is typically performed by a combination of optical and e-beam lithography. Optical lithography is used for larger structures while smaller micron sized structures are defined via e-beam lithography. In the case of optical lithography the following steps are used:

1. Spin S1813 positive photoresist at 6000 rpm for 50 seconds using a ramp rate of 1000 rpm/s.

2. Soft bake at 90 C for 50 seconds.

3. Expose the devices through the previously made mask and using SUSS mask aligner.

4. Develop structures in MF-321 for approximately 60 seconds or as needed. Inspect under an optical microscope.

In the case of e-beam lithography the following steps are used:

1. Spin A4 PMMA positive e-beam resist at 5000 rpm for 40 seconds using a ramp rate of 1000 rpm/s.

2. Bake at 180 C for 90 seconds.

3. Expose the samples in JEOL6500 scanning electron microscope at 30 kV and 7 mm working distance.

4. Develop chips in a 3:1 solution of isopropyl alcohol and MIBKA for 60 seconds, followed by a 20 second rinse in isopropyl alcohol. Inspect under an optical microscope.

A.3 Mesa etch

Mesa etch is normally performed with wet etching. While various wet etching approaches have been developed in the literature, in this thesis we have predominantly used a "cocktail" III-V etchant, which uniformly etches all antimonide materials, and with approximately the same rate. It goes without saying that for successful etching, the sample surface needs to be clean and without any residues or films, such as photo and ebeam- resists, which would prevent and/or interfere with sample etching. The follwing steps are used:

1. Hard bake samples at 100 C for 45 seconds.

2. Etch samples using the solution of H_3PO_4: H_2O_2 : $C_6H_8O_7$:H_2O (3:5:55:220), with a nominal rate of $150 - 250$ Å/min.

3. Inspect under an optical microscope.

A.4 Metallization

Metallization pads are defined via optical lithography and deposited in an e-beam evaporator system. The following steps are employed:

1. Define metallization pads as described earlier.

2. Deposit germanium, palladium and gold layers in an e-beam evaporator system. Layer thicknesses are 430 Å, 300 Å, and 870 Å, respectively. Nominal deposition rates are 1.5 Å/s, 1.5 Å/s, and 2 Å/s. In order to ensure longevity of crucible liners, the e-beam power should be ramped up and down slowly.

3. If no processing at higher temperatures will follow the metallization process, then devices should be annealed at 300 C in a forming gas atmosphere for few minutes. Typically this step is not necessary if silicon-nitride will be deposited via plasma enhanced chemical vapor deposition, because in this case structures are unintentionally annealed.

4. After deposition, lift-off in aceton for approximately 5 minutes or until the metal has been completely removed.

A.5 Silicon-nitride deposition

Silicon nitride is deposited using a plasma enhanced chemical vapor deposition system, manufactured by Trion. The following parameters have been used for a nominal deposition rate of 300 Å/min:

1. Chamber pressure: 600 mTorr
2. Power: 50 W
3. Temperature: 350 C
4. 12 sccm SiH_4
5. 10 sccm NH_3
6. 200 sccm N_2

A.6 Via etching

Vias in silicon nitride are etched using a reactive ion etching system also manufactured by Trion. The following parameters have been used for a nominal etching rate of 2400 Å/min:

1. Chamber pressure: 100 mTorr
2. Power: 100 W
3. 50 sccm CF_4

4. 6 sccm O_2